Study of Single Event Upset Phenomena Induced by Muons and Protons in 65-nm Planar Bulk SRAMs

鄧，亦凡

https://hdl.handle.net/2324/7182513

出版情報：Kyushu University, 2023, 博士（工学），課程博士
バージョン：

Study of Single Event Upset Phenomena Induced by Muons and Protons in 65-nm Planar Bulk SRAMs

Deng Yifan

Department of Interdisciplinary Engineering Sciences
Interdisciplinary Graduate School of Engineering Sciences
Kyushu University

February 2024

Abbreviations

ADU	Analog to Digital Unit
BL	Bit Line
BS	Board Side
CCD	Charge-Coupled Device
CCE	Charge Collection Efficiency
CERN	European Organization for Nuclear Research
CMOS	Complementary Metal Oxide Semiconductor
CNN	Convolutional Neural Networks
CR	Cosmic Ray
EXPACS	Excel-based Program for calculating Atmospheric Cosmic-ray Spectrum
HEP	High Energy Proton
HI	Heavy Ion
ISMS	International Society for μSR Spectroscopy
JAEA	Japan Atomic Energy Agency
J-PARC	Japan Proton Accelerator Research Complex
KEK	High Energy Accelerator Research Organization
LEP	Low Energy Proton
LINAC	Linear Accelerator
MLF	Materials and Life Science Experimental Facility
MOS	Metal Oxide Semiconductor
MR	Main Ring synchrotron
NMOS	N-type Metal Oxide Semiconductor
PMOS	P-type Metal Oxide Semiconductor
PMT	Photomultiplier Tube
PS	Package Side
PVC	PolyVinyl Chloride
RCS	Rapid Cycling Synchrotron
SER	Soft Error Rate
SEU	Single Event Upset
SOTB	Silicon-on-Thin-BOX
SRAM	Static Random Access Memory
SV	Sensitive Volume
TEG	Test Element Group
UVT	UltraViolet Transmittance
VLSI	Very Large-Scale Integrations
WL	Word Line

1 Introduction

1.1 Soft Error and Single Event Upset

Industrial needs for highly reliable circuits are in a wide area of applications, including medical, aerospace, automotive, networking, nuclear engineering [1], supercomputer [2], and machine learning applying Convolutional Neural Networks (CNN) [3]. As the number of electronic devices increases, consumer electronics may require higher reliability. For circuit reliability, the problem of radiation-induced soft errors occurring inside the Very Large Scale Integrations (VLSIs) in a terrestrial radiation environment has been recognized as a major threat to electronics [4].

Static random access memory (SRAM), one of the most sensitive components in VLSIs with reported irradiation experiments and simulation [5], is subject to a representative radiation-induced soft error due to a hit of a single particle named Single Event Upset (SEU) [1]. It is caused by a transient signal induced by energetic ionizing radiation and destroys the information stored in memory elements. The functional structure of the memory cell in SRAM and the mechanism of SEU can be briefly described as follows.

The circuit structure of a six-transistor SRAM cell is shown in Figure 1.1. The two parts in the red dash frames are each equivalent to two CMOS inverters, and the structure and circuit diagram are shown in Figure 1.2. The outputs and inputs of the two inverters are connected as shown in Figure 1.3, and the latch voltage state is self-sustaining when not writing. The two MOS transistors on the left and right sides in Figure 1.1 become on when the reading and writing are performed.

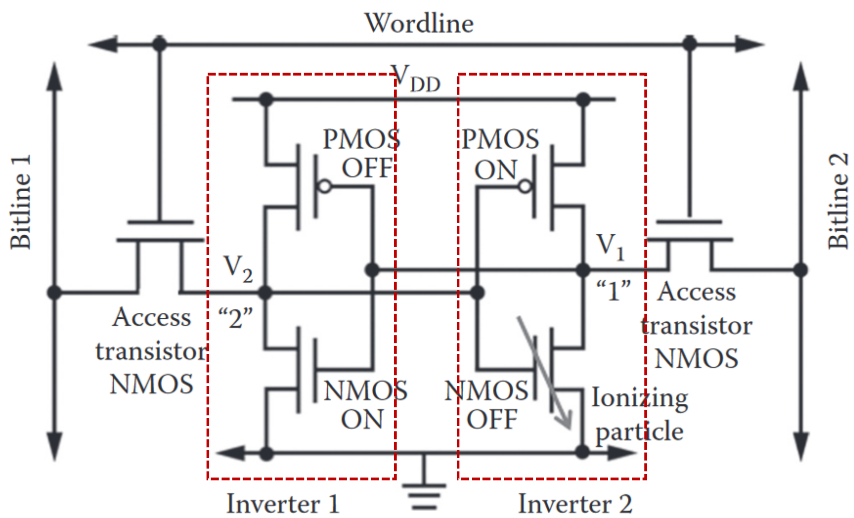

Figure 1.1 Schematic circuit for a six-transistor SRAM cell [1].

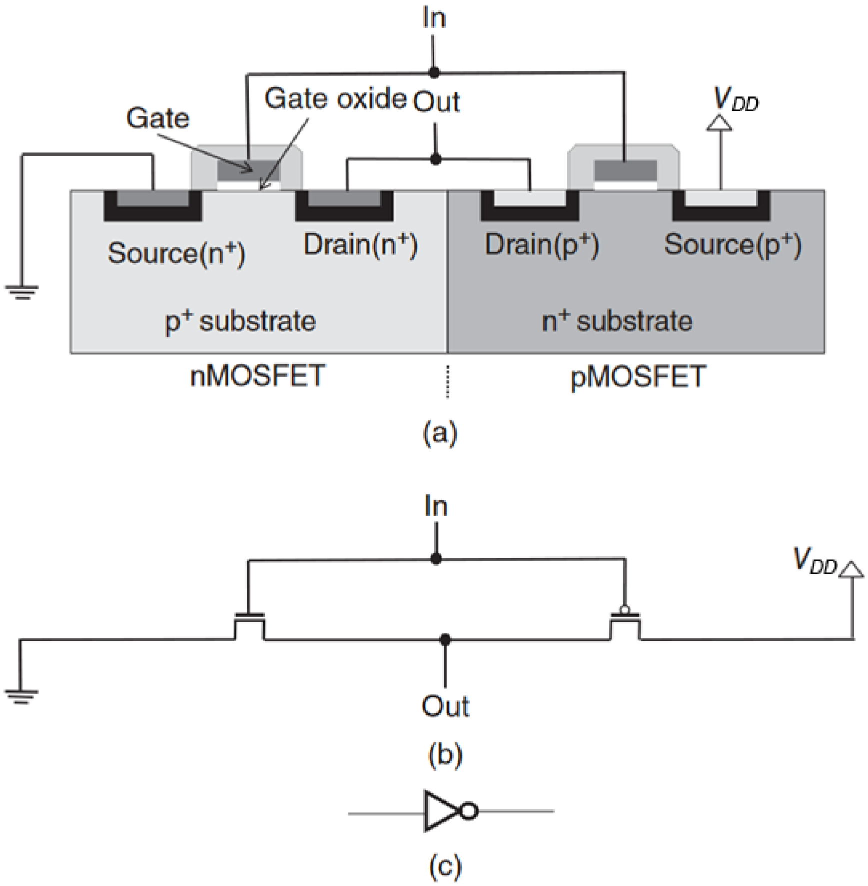

Figure 1.2 (a) Structure of inverter, (b) circuit, and (c) its symbol. [4]

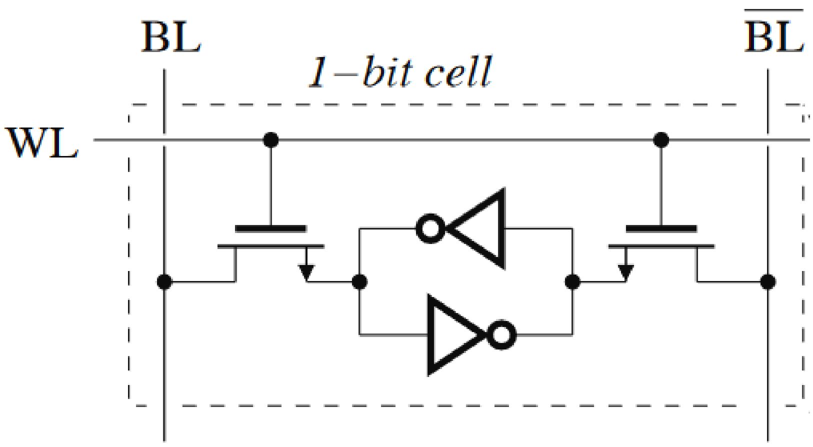

Figure 1.3 Equivalent circuit of an SRAM cell [6].

When the memory cell is storing data, one of the MOS transistors in each inverter should be on, and the other should be off. Once a MOS transistor in the off state is turned on by accident, the value stored in the cell is flipped.

As shown in Figure 1.4, when an energetic particle strikes the device material, electrons along the particle track can be released by direct ionization of the incoming particle or indirect ionization of nuclear reactions. These electrons produce a cascade of secondary electrons, which thermalize and create electron-hole pairs along the particle path. The released carriers are quickly transported in the device by charge drift and diffusion and finally collected by the gates.

The sensitive volume (SV), containing the p-n junction's depletion region, allows very efficient collection of the deposited charge because of the strong electric field [1], [7]. According to [8], the SV of the SRAM memory cell is defined as the depletion region of the off-state NMOS and PMOS. If the collected charge at the SV exceeds the minimum charge needed to open the off-state MOS transistor, i.e., the critical charge (Q_c), the value stored in the cell will be flipped, and an SEU will occur.

The probability of an SEU is more significant when the critical charge of a cell is lower. Given that supply voltage and cell size are reduced with each technological generation, the critical charge of SRAM cells continues to decrease as long as the transistor structure is the same, making the cell more vulnerable to more types of particles. [1]

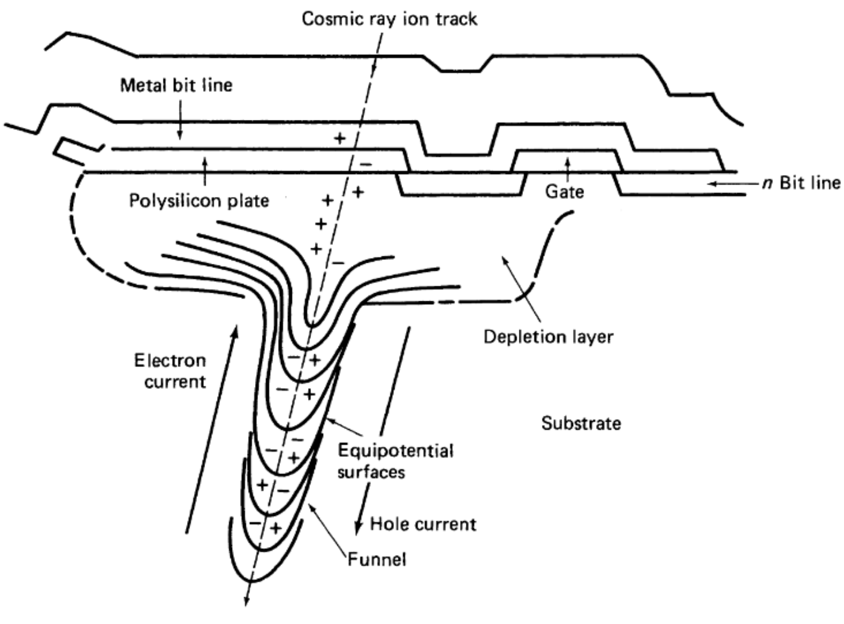

Figure 1.4 Charge deposition, transportation, and collection process along the ion track in the bulk device [7].

1.2 Cosmic Rays in Terrestrial Environment

Primary Cosmic Rays (CRs) come from all directions of deep space and the sun, composed of protons, helium nuclei, and heavy ions with high energy. Their collisions with atmospheric nuclei give rise to secondary or terrestrial cosmic rays. A schematic of this process is shown in Figure 1.5.

The primary CRs are subject to strong colliding with atmospheric nuclei, such as nitrogen and oxygen, resulting in secondary particles, such as pions, kaons, hyperons, charmed particles, and nucleon-antinucleon pairs by various nuclear reactions. The energetic primaries and their spallation fragments continue propagating in the atmosphere and interacting with air atoms, producing more particles along their trajectories. A fraction of them, including neutrons, muons, protons, pions electrons, positrons, and photons, can be propagated to ground level [1], [4]. Figure 1.6 shows a typical energy spectrum of cosmic rays at the sea level near Tokyo, calculated by an Excel-based program for calculating atmospheric cosmic-ray spectrum (EXPACS) [9]–[11].

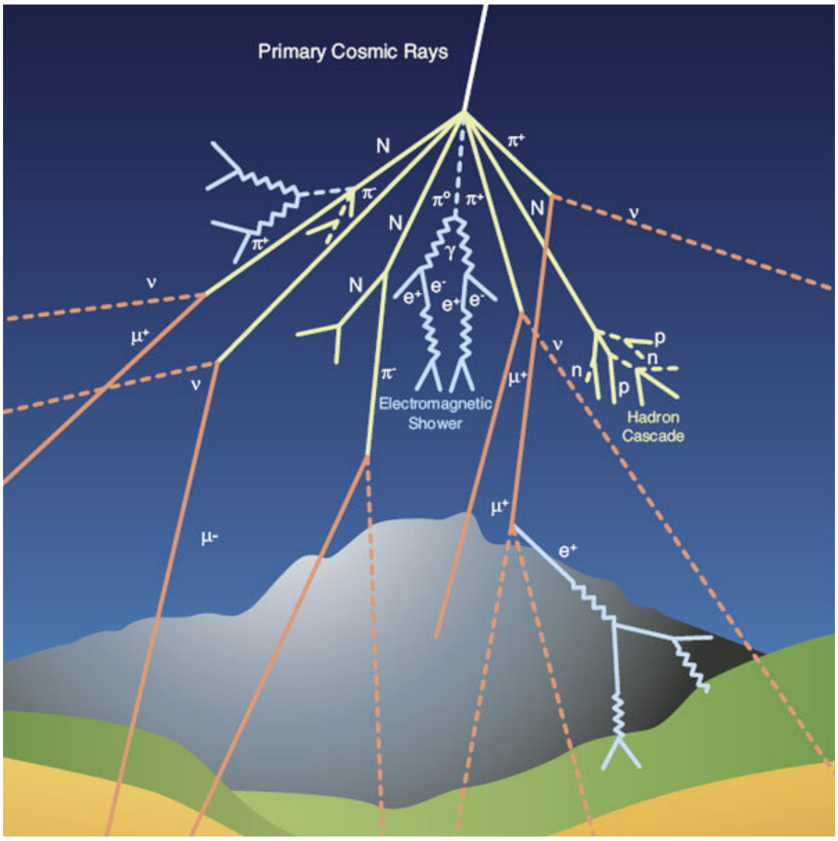

Figure 1.5 Schematic of the cosmic rays reaching the ground [12].

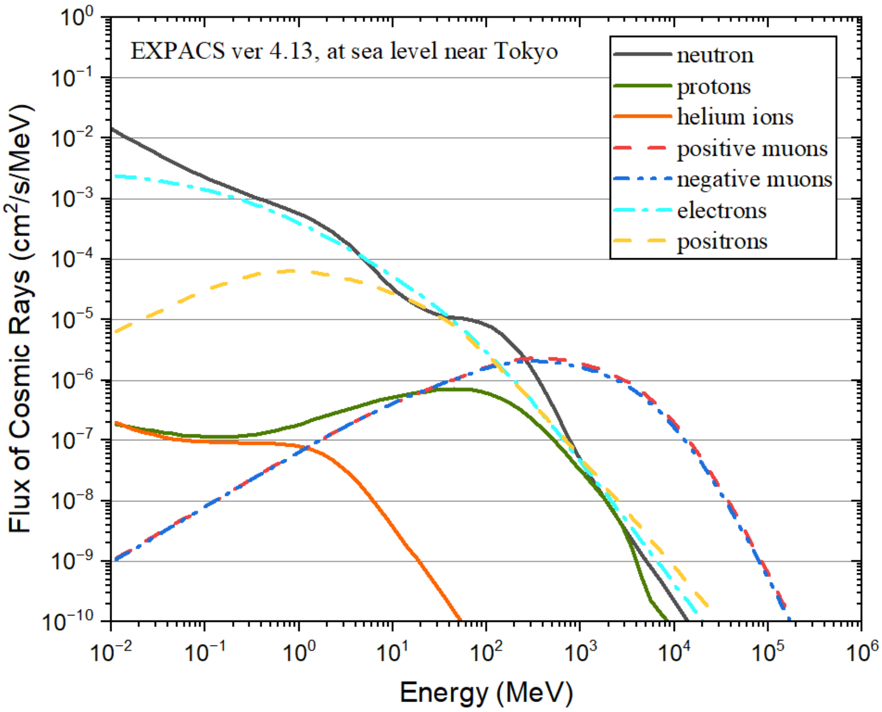

Figure 1.6 Energy spectra of the secondary cosmic rays at ground level, calculated with EXPACS [9]–[11].

Among the cosmic rays at ground level, neutrons have always been considered a main radiation source for SEUs in terrestrial environments. With the miniaturization of semiconductors and the decrease in operating voltage, there is a growing interest and discussion in whether the large number of muons may be another source of SEUs through the direct ionization process and nuclear capture reaction for negative muons [13]–[17]. As for protons, besides the high-energy protons (HEPs), which can produce SEUs by secondary ions released from the nuclear reaction with material atoms, the low-energy protons (LEPs) producing SEU through direct ionization have been a subject of study for one and a half decades [18].

Figure 1.7 predicts that the contribution of protons and muons to the Soft Error Rate (SER) in bulk devices will become more pronounced as the technological node decreases [19]. In Figure 1.7, the unit of SER is FIT/Mbit, where FIT means Fault in Time, i.e., the number of SEU occurrences per 10^9 hours. It is worth pointing out that alpha-emitting impurities in some packaging materials are considered in predicting alpha particle contribution to SER [19].

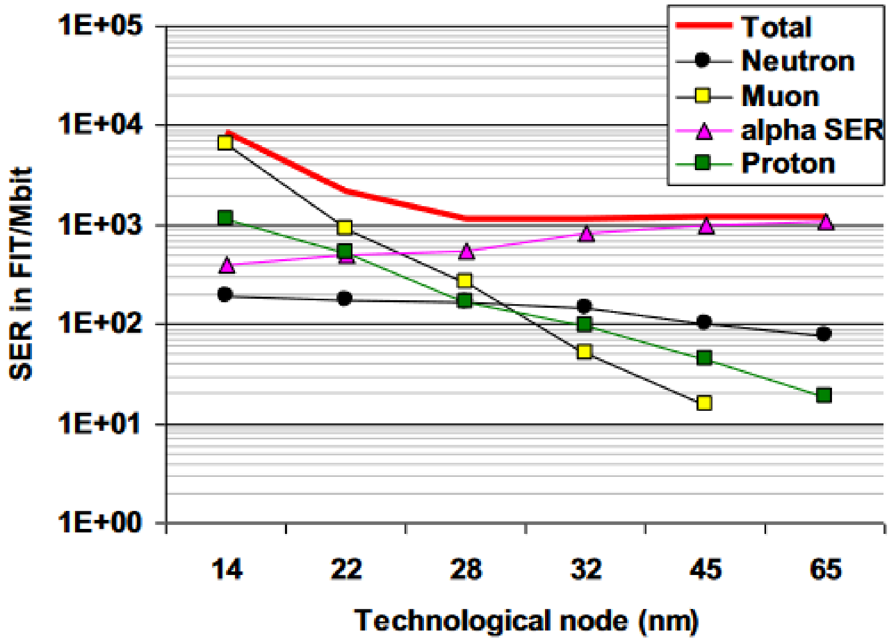

Figure 1.7 Contributions of various particles to the Soft Error Rate (SER) in bulk devices at each technological node [19].

1.3 Characteristics of Muons and Protons

1.3.1 Basic Properties of Muons

Muons are unstable elementary particles of two charge types (positive muons μ^+ and negative ones μ^-) having a spin of 1/2 and a lifetime of 2.2 μs. The muon mass m_μ is 105.66 MeV/c^2, which is intermediate between the proton mass m_p and the electron mass m_e, i.e., 1/9 times m_p and 207 times m_e [20].

A muon is produced in the decay of pion ($\pi^\pm$) or kaon ($K^\pm$) according to:

$$\pi^+ \to \mu^+ + \nu_\mu, \tag{1-1}$$

$$\pi^- \to \mu^- + \bar{\nu}_\mu, \tag{1-2}$$

$$K^+ \to \mu^+ + \nu_\mu, \tag{1-3}$$

$$K^- \to \mu^- + \bar{\nu}_\mu, \tag{1-4}$$

where ν_μ and $\bar{\nu}_\mu$ denote the muon and anti-muon neutrinos, respectively. The μ^+ and μ^- in vacuum have the following major (100%) decay modes:

$$\mu^+ \rightarrow e^+ + \bar{\nu}_\mu + \nu_e, \tag{1-5}$$

$$\mu^- \rightarrow e^- + \nu_\mu + \bar{\nu}_e, \tag{1-6}$$

where ν_e and $\bar{\nu}_e$ denote the electron and anti-electron neutrinos, respectively.

When muons enter the device, they interact with the electrons and nuclei of the device material and begin to lose energy as they penetrate. The kinetic energy that a charged particle loses in the matter per unit length is called the stopping power. The stopping power of positive and negative muons as a function of muon kinetic energy is shown in Figure 1.8. The stopping power is calculated by Geant4 [21]. A detailed description of the Geant4 calculation model will be given in Chapter 3.

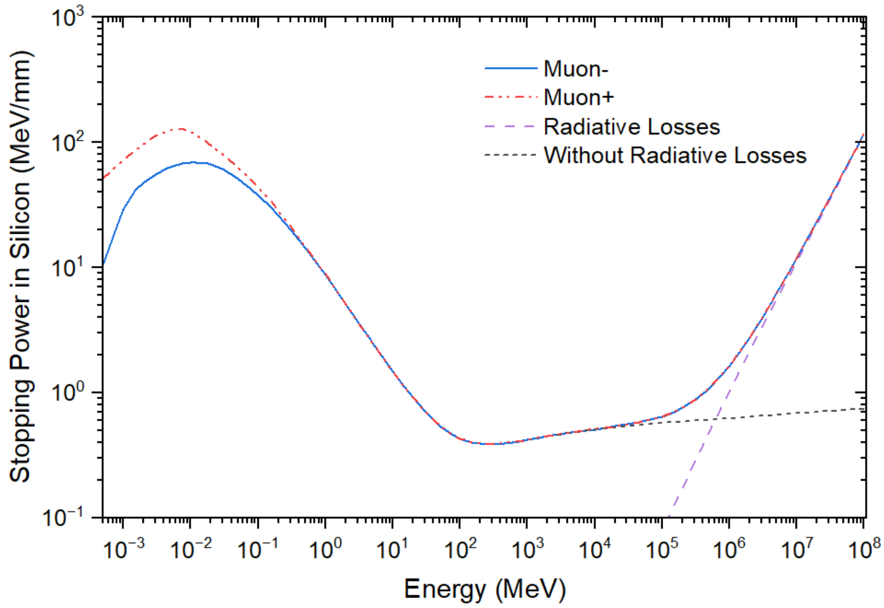

Figure 1.8 Stopping powers of positive and negative muons in silicon calculated with Geant4 [21].

In the low-energy region (below 100 MeV), the energy loss of the muon is mainly produced by ionization and excitation. At energies above 2×10^4 MeV, bremsstrahlung and positron-electron pair production of muon dominate the energy loss. They are summed up as the radiation loss and shown with the purple dash line in Figure 1.8. It is worth pointing out that in the energy region below 1 MeV, positive and negative muons show significantly different stopping power due to the Barkas effect [22]–[24].

1.3.2 Negative Muon Capture Reaction

After a positive muon comes to a stop through interaction with matter, it will decay into a positron and two neutrinos, as described in equation (1-5). However, as illustrated in Figure 1.9, negative muons have a possibility to react with the device material atoms after they are stopped in the material.

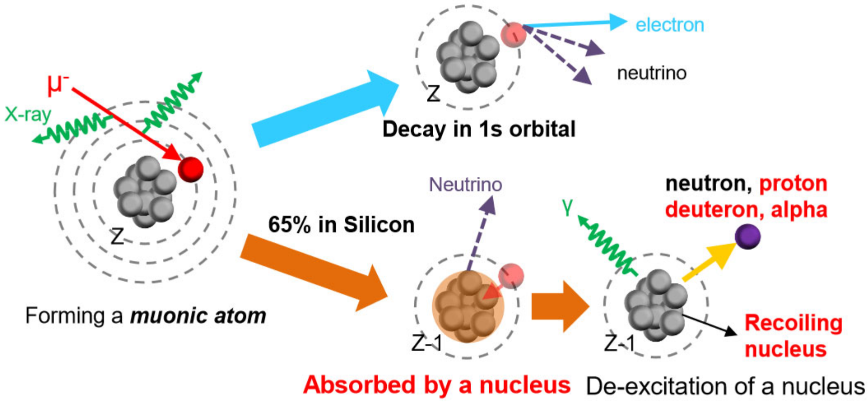

Figure 1.9 Schematic illustration of the negative muon capture.

When the negative muon is stopped in the target material, it takes a replacement with the innermost electron of a near atom, forming the muonic atom in an excited state. Since all low-lying muonic states are unoccupied, the muon electromagnetically cascades rapidly to the lowest quantum state (1s) by various cascade transitions, mainly the radiative processes emitting X-ray photons. After the muon has reached the 1s orbit, it either decays in the 1s orbit, as shown in the equation (1-6) or is captured by the nucleus via the weak interaction. The latter is known as the muon capture reaction. In silicon, approximately 35% of negative muons decay in orbital, and the remaining 65% is captured by the nucleus.

During the muon capture reaction, the nucleus first releases a muon neutrino, leaving a residual heavy nucleus in a highly excited state, which is described by:

$$\mu^- + X_Z^A \rightarrow v_\mu + X^{*}{}_{Z-1}^{A}, \tag{1-7}$$

where Z is the atomic number, and A is the nucleon number of the target atom. The residual heavy nucleus de-excites by releasing charged particles, neutrons, or gamma rays until it cascades to stable nuclei.

For example, the residual nucleus $^{28}Al^{*}$, formed by a silicon nucleus capturing a negative muon, is suggested to have a global pattern of de-excitation modes described in Table 1.1 according to [25].

Table 1.1 Global pattern for the negative muon capture reactions in ^{28}Si [25]

Reaction	%	Reaction	%	Reaction	%	Reaction	%
$(\mu)^{28}$Al	26						
$(\mu,n)^{27}$Al	45	$(\mu,p)^{27}$Mg	2.0				
$(\mu,2n)^{26}$Al	12	$(\mu,pn)^{26}$Mg	4.9	$(\mu,d)^{26}$Mg	3.1		
$(\mu,3n)^{25}$Al	1.0	$(\mu,p2n)^{25}$Mg	1.4	$(\mu,dn)^{25}$Mg	1.0	$(\mu,2pn)^{25}$Na	0.1
		$(\mu,p3n)^{24}$Mg	0.6	$(\mu,d2n)^{24}$Mg	0.3	$(\mu,\alpha)^{24}$Na	1.0
		$(\mu,p4n)^{23}$Mg	0.1			$(\mu,\alpha n)^{23}$Na	0.8
						$(\mu,\alpha 2n)^{22}$Na	0.5
						$(\mu,\alpha 3n)^{21}$Na	0.2

The emission spectra of protons, deuterons, tritons, and alpha particles from nuclear muon capture reaction on Silicon are shown in Figure 1.10. The open triangles and solid circles represent the experimental data from Edmonds [26] and Budyashov [27]. The dotted lines represent the calculated results by Geant4, which will be explained in detail in Chapter 3.

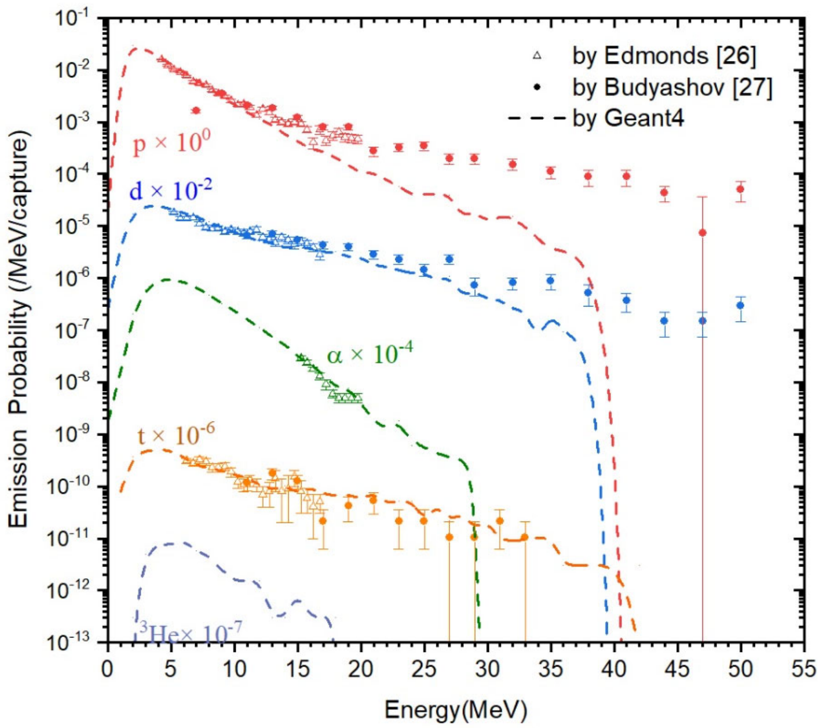

Figure 1.10 Measured and simulated energy spectra of protons, deuterons, tritons, and alpha particles from the muon capture reaction on silicon.

These released charged particles can deposit large amounts of energy, and their significant effects on SEU will be shown in Chapter 2.

1.3.3 Basic Properties of Protons

A proton is a charged particle with a positive electric charge of +1. The mass of a proton is 938.27 MeV/c^2, approximately nine times as heavy as that of the positive muon.

The interaction of protons with material depends on proton energy. Low-energy protons behave as charged particles and deposit the energy primarily through ionization and excitation. At very high energies, radiative energy loss dominates. The stopping power of the proton is shown as a function of the kinetic energy of the proton and compared to that of the positive muon in Figure 1.11.

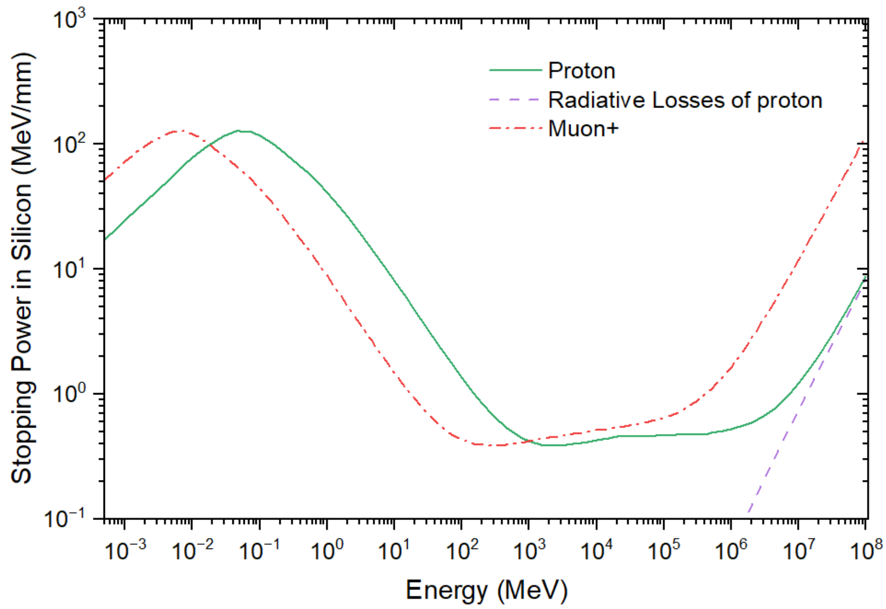

Figure 1.11 Proton stopping power for silicon calculated with Geant4 and compared with the positive muon one.

As shown in Figure 1.11, the stopping power curve of the proton is very similar to that of the positive muon. The relationship between them can be approximated by:

$$S_p(E) = S_\mu\left(E\frac{m_\mu}{m_p}\right), \tag{1-8}$$

where E represents the kinetic energy, S_p is the stopping power of the proton, and S_μ is that of the positive muon.

In addition, high-energy protons (typically above 20 MeV) can also lose their energy by nuclear interactions, like neutrons. Recoil atoms from nuclear reactions can also deposit energy in the material, resulting in indirect ionization. Both direct and indirect ionization contribute to SEUs.

1.4 Energy Loss Straggling

The total continuous energy loss of charged particles is a stochastic quantity with a distribution described as a straggling function. According to [28], the ionization energy loss fluctuation of non-relativistic proton and muon can be simplified using a Gaussian function:

$$E_k(s) \sim G\left(\bar{E}_k(s), \sigma\right), \tag{1-9}$$

$$\sigma^2 = 4\pi r_e^2 m_e^2 c^4 N_{el} s, \tag{1-10}$$

where $E_k(s)$ represents the variation in the kinetic energy of a specific particle at the penetration depth s, which follows the Gaussian distribution with an average energy deposition $\bar{E}_k(s)$ and the standard deviation σ that is only related to the depth s. Here, r_e is the classical electron radius, m_e is the electron mass, c is the light velocity, and N_{el} is the electron density of the medium.

The energy straggling will significantly affect the distribution of energy deposition with a depth of incidence, i.e., the Bragg curve. Figure 1.12 shows the Bragg curves of protons and positive muons in silicon, which have the same ranges (0.2, 1.0, and 1.8 mm) in silicon.

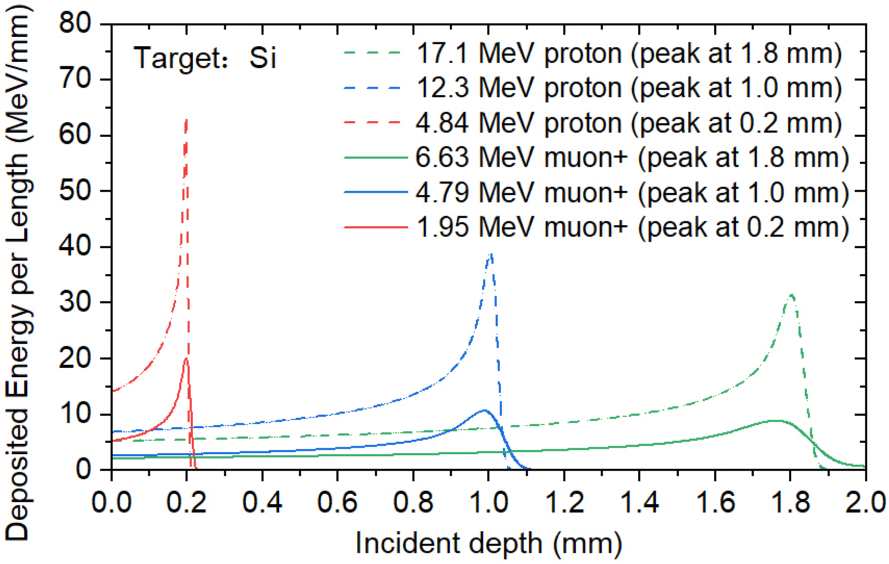

Figure 1.12 The Bragg curves of protons and positive muons having the same ranges (0.2 mm, 1.0 mm, and 1.8 mm) in Silicon.

Figure 1.12 shows three important conclusions that are important theoretical underpinnings of this study that were applied to qualitatively explain the experimental and simulation conclusions in Chapters 2, 3, and 4.

First, the incident depth of both protons and positive muons at the Bragg peaks increases with their incident energy. However, the incident energy of a proton is always greater than that of a muon when their Bragg peaks overlap at the same depth. Therefore, a one-to-one mapping can be established between the incident energies of the two, which is the basis for the energy mapping method of predicting the muon SEU cross-sections by using proton tests and Monte Carlo simulations in Chapter 4.

Second, for positive muons, the height of the Bragg peak also becomes smaller and broadens with the depth of the Bragg peak. Since energy straggling is related to the depth of incidence according to the equations (1-9) and (1-10), the width of the energy spectrum will increase with the depth of SV, which will broaden the Bragg peak and decrease its magnitude deposition characteristics. This phenomenon can qualitatively explain the difference in SEU cross sections in different irradiation sides in Chapters 2 and 3.

Finally, protons with the Bragg peak position at the same depth have a much more significant peak magnitude than the positive muons. This can also be explained by the influence of energy loss straggling. After penetrating the same thickness s, the average energy $\bar{E}_k(s)$ of the muons in the depth s is always less than that of protons when their Bragg peaks overlap. Meanwhile, the standard deviation $\sigma(s)$ of the kinetic energy distribution in depth s is the same for both. Therefore, the relative energy width defined by $\sigma(s)/\bar{E}_k(s)$ of the muon is greater than that of the proton. As a result, the positive muon's Bragg peak is much lower and broader than the proton's, as shown in Figure 1.12, and the broadening of the Bragg peak becomes more significant as the range lengthens with increasing incident energy. This phenomenon is then used to qualitatively explain the difference in the magnitude of SEU cross-section between proton and positive muons in Chapter 4.

It should be noted that the above three conclusions from Figure 1.12 can only qualitatively explain the experimental and simulation conclusions in Chapters 2, 3, and 4. Their detailed quantitative explanations are based on a concept of effective SEU fluence, which will be introduced in detail in Chapters 3 and 4.

1.5 Previous Works

As mentioned in Section 1.2, neutrons have always been considered a main radiation source for SEUs in terrestrial environments. Interactions of neutrons with atomic nuclei, including elastic scattering, inelastic scattering, and capture, are summarized clearly in [29], [30]. Many works on neutron-induced soft errors have been performed, for instance [31]–[35]. The standard for neutron-induced soft error rate testing of ICs was established and revised by the JEDEC Solid State Technology Association [36]. The neutron-induced soft error has been investigated well, and the test method has been practically implemented. It is worth mentioning that Abe et al. investigated the impact of the irradiation side on the neutron-induced SEU in 65-nm SRAMs [37]. It was reported that the number of SEUs observed by the board side (BS) irradiation was approximately 20% to 30% smaller than that observed by package side (PS) irradiation. The SER observed from the PS irradiation was approximately twice as large as that from the BS irradiation. These facts inspired the objective of the irradiation side impact on muon SEU in this study.

After intense muon beams became available using particle accelerators in the 1960s, the field of scientific research using muons has been growing yearly [20]. In 1979, Ziegler and Lanford first described that muons could interact with matter at relatively low incident energies through direct ionization, electromagnetic scattering, and negative muon capture [38]. Moreover, they predicted that devices would be susceptible to the natural ionization of cosmic-ray muons because of the dramatic decrease of critical charge Q_c. In the 1980s, Dicello et al. studied the muon-induced soft error and evaluated the contribution of cosmic-ray muons to the SER on sea level [39]–[42]. However, the positive muon with a fluence of 4×10^{11} cm^{-2} produced only three events of soft errors, and the negative muon beam with a fluence of 8×10^{10} cm^{-2} made no errors [39]. The soft error rate induced by stopping muon was estimated at only 2% of the total rate from all species [42]. In summary, the SEU introduced by the muon was almost negligible in these studies in 1980s because the critical charge of the devices used in the irradiation tests was relatively high compared to modern devices.

Until recent years, the muon-induced soft error has drawn attention due to the critical charge being decreased by the miniaturization and low voltage operation of circuits. From 2010, a series of muon-induced SEU experiments were performed by Sierawski et al. [13]–[15]. Using low-energy positive muon beams, they demonstrated the effects of muon direct ionization for bulk SRAMs of different technology nodes (i.e., 65, 55, 45, and 40 nm). The SEU probability increased with the reduction of the supply voltage due to the decrease of the critical charge, as shown in Figure 1.13. Serre et al. studied the effect of low-energy (<1 MeV) negative muons on SRAMs and demonstrated the importance of the negative muon capture mechanism as an additional mechanism of charge deposition in silicon [43]. More recently, experiments and simulations have been performed for negative and positive muon-induced SEUs in 65-nm bulk SRAMs and 65-nm Silicon-on-Thin-BOX (SOTB) SRAMs by Liao and Manabe et al. [8], [44]. In the studies, the peak SEU cross-section of the negative muon is about nine times as large as that of the positive muon due to the contribution of the negative muon capture. In [45], Liao et al. reported that the incident angle of the muon beam also influences the SEU cross-sections. Moreover, indoor and outdoor muon SERs were predicted depending on the experimental SEU cross-section data in [17]. The muon SER outdoors is at most 1% of the neutron, while on the first floor of a five-story concrete building, the muon SER is at most 10% of the neutron. Although the muon SER is still insignificant compared to neutrons, muon SEU is predicted to be more pronounced in devices with smaller technology node sizes [19].

In addition, Trippe et al. proposed a method based on the proton test and simulation to predict the muon SEU because the limited muon test facilities make it difficult and financially expensive to conduct a muon irradiation test [46].

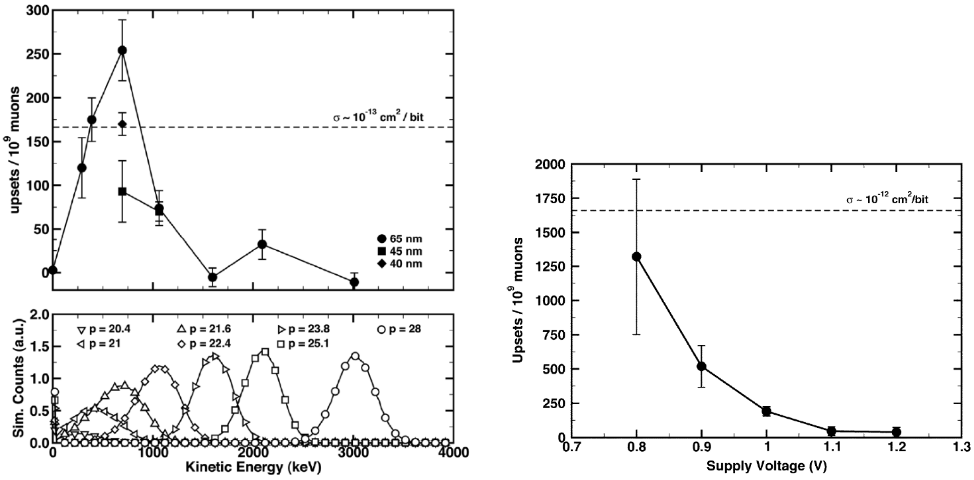

(a) Energy dependence (b) Supply operation voltage dependence

Figure 1.13: Measured positive muon-induced SEU probabilities as the functions of (a) the kinetic energy and (b) the supply voltage. The figures are taken from Figures 4 and 5 in [13]. (a) was measured under an operation voltage of 1.0 V for 65, 45, and 40 nm SRAMs, and (b) was measured under a 21 MeV/c muon for 65-nm SRAM.

The impact of low-energy proton (LEP) on modern electronics is an important issue for both space and terrestrial applications. Rodbell et al. noted that LEP-induced SERs should be accounted for in terrestrial radiation environments. While shielding materials can easily absorb LEP, scattering of high energy protons (HEP) can yield significant fluxes of LEP, impacting electronics [47]. For the recent one and a half decades, direct ionization from LEP and related upsets in highly integrated memory devices have been a subject of study [48]–[54]. In 2023, Coronetti et al. published the experimental and simulation results of proton direct ionization upsets at tens of MeV on 65-nm SRAMs [18]. For the chip under study, direct ionization is a dominant contributor at 10 MeV, a significant contributor at 20 MeV, and as important as the nuclear elastic scattering at higher energies. Over 50 MeV, the behavior of the proton begins to resemble that of the neutron for inducing SEUs. In addition, the study showed that high-energy (>0.860 keV) δ-rays generated inside and outside the SV are determinants in triggering upsets at primary proton energies above 3 MeV. A small amount of these high-energy δ-rays produced by a single proton can deposit enough energy to exceed the critical energy of the SRAM because Coulomb scattering events significantly increase the actual path of the δ-ray inside the SV.

1.6 Objective

As mentioned, there is a growing interest and discussion about whether the large number of muons in cosmic rays may be another source of SEUs through direct ionization and negative muon capture in previous works. However, the SEU cross-sections and the SER predictions from acceleration tests highly depend on the experimental conditions. Since muons pass through different thicknesses and materials before reaching the Sensitive Volume (SV) in cases of varying irradiation sides, i.e., package side (PS) and board side (BS), the changes of peak incident energy and energy straggling degree will influence the muon-induced SEUs. Therefore, the primary objective of this study is to investigate the impact of irradiation side and irradiation angle on muon-induced SEU in 65-nm bulk SRAMs.

On the other hand, the minimal muon test facilities worldwide make it challenging to conduct muon irradiation tests, and such muon-accelerating tests are often financially expensive. As the Low Energy Proton (LEP) induced SEU and its contribution to the SER have been investigated widely and reported to need to be considered at ground level, this study also seeks to establish a method for predicting muon SEUs using a combination of proton testing and Monte Carlo simulation, after comparing positive muon and proton-induced SEU in 65-nm bulk SRAM. Because LEP and positive muons have the same charge and a scale relationship of stopping power with kinetic energy, they deposit energy and produce SEUs in devices primarily through direct ionization.

The last objective of this study is to investigate how the dependence of irradiation sides observed in the experimental SEU cross-sections affects the SER prediction. The SERs of positive and negative muons in PS and BS irradiation tests are estimated. The results in BS irradiation are compared with protons. Moreover, since the incident angle dependence of muon-induced SEUs is reported in [45], it is of interest to evaluate the muon-induced SER under a realistic environment considering the zenith angle distribution of muon flux.

Thus, this study has the following three main objectives:

1) To analyze the experimental data of 65-nm bulk SRAMs, investigate the effects of irradiation side and irradiation angle on muon-induced SEU, and investigate the associated physical mechanism using Monte Carlo simulations.
2) To compare positive muon-induced SEU in 65-nm bulk SRAM with proton-induced one and establish a method for predicting muon SEUs using a combination of proton test and simulation.
3) To estimate the muon's contribution to SER in 65-nm bulk SRAMs at ground level using test results with different irradiation sides and compare with the proton's contribution in BS irradiation. To estimate muon SERs under a realistic environment considering the zenith angle distribution of muon flux.

Chapter 1 of this thesis introduces the background and motivation of this work. The subsequent Chapters are arranged as follows.

Chapter 2 presents the re-analysis of measurements on muon SEU cross-sections in different irradiation sides. The negative and positive muon acceleration tests were performed for 65-nm bulk SRAM. In the experiment period, both package side (PS) irradiation and board side (BS) irradiation tests were done, while the results of PS irradiation have not been wholly analyzed nor published. This chapter describes the previous tests' experimental facilities, devices, and setups. Then, the muon beam intensity in PS irradiation is newly analyzed using the image luminance of the beam profile monitor. After that, the measured SEU cross sections in the PS irradiation tests are derived and compared with the previously published results from BS irradiation.

Chapter 3 gives a simulation analysis of measurement results. The simulation method is introduced first, including the simulation tools (Geant4), physical process, geometry model, beam source, and SEU determination in simulation. Then, the critical charge dependence of SEU cross sections for positive and negative muons in BS irradiation is analyzed to determine the critical charge so that the simulation reproduces the measurement well. The momentum-dependent SEU cross sections for positive and negative muons in PS and BS irradiation are derived using the simulation and compared with the measurement. At the end of the Chapter, a quantitative assessment of the impact of energy straggling on SEU is established based on the concept of effective SEU fluence.

Chapter 4 compares positive muon-induced SEU in BS irradiation with proton-induced ones by simulation. Then, a new method was developed to predict the positive muon-induced SEU using proton tests and Monte Carlo simulation.

Chapter 5 gives the SER estimations for positive and negative muon in 65-nm bulk SRAMs based on the measured data in PS and BS irradiations. Then, the SERs were predicted under a more realistic environment by considering the zenith angle distribution of muon flux.

Finally, Chapter 6 gives a summary and conclusions, and the perspectives of the future work are also described.

2 Analysis of Measurements on Muon SEU Cross-sections in Different Irradiation Side

2.1 Introduction

As mentioned in Chapter 1, the SEU cross-sections and the SER predictions from acceleration tests highly depend on the experimental conditions. Since muons pass through different thicknesses and materials before reaching the Sensitive Volume (SV) depending on the direction of muon incidence, it is also of interest to know the impact of the irradiation side on muon-induced SEUs.

In the previous study [8], negative and positive muon acceleration tests were performed for 65-nm bulk SRAMs at the Muon Science Facility (MUSE) [55], [56] in Materials and Life Science Experimental Facility (MLF), Japan Proton Accelerator Research Complex (J-PARC). In the experiment period, both package side (PS) irradiation and board side (BS) irradiation tests were conducted, while the results of PS irradiation have not been wholly analyzed nor published.

Therefore, this chapter describes the experimental facilities, devices, and setups in the previous tests, then re-analyzes the measured data from the PS irradiation test and compares them with the previously published results from BS irradiation.

2.2 Previous Experiment

2.2.1 Muon Science Facility and Device Under Test

The PS and BS muon irradiation tests for the 65-nm bulk device in the previous experiment were performed in MLF of J-PARC. The accelerator complex of J-PARC was constructed in the south part of the Japan Atomic Energy Agency (JAEA) site in Tokai village, north of Ibaraki prefecture. The J-PARC proton accelerators consist of the following three parts: a 400-MeV Linear Accelerator (LINAC), a 3-GeV Rapid Cycling Synchrotron (RCS), and a 50-GeV Main Ring synchrotron (MR). The Aerial shot from the west side of J-PARC is shown in Figure 2.1.

Approximately 90% of the 3-GeV proton beam in RCS was sent to the MLF to produce intense pulsed muon and neutron beams. The Muon Science Facility (MUSE) inside the MLF provides kinds of decay and surface muon beams, of which the layout is shown in Figure 2.2. The PS and BS irradiation tests of muon-induced SEUs of 65-nm bulk SRAMs were all performed using the muon beam from the D Line. The production mechanism and characteristics of muons in the D line are as follows.

The primary 3-GeV proton beam was bombarded on a graphite target to generate pions through proton-proton or proton-neutron reactions in the carbon nucleus. These pions are captured into the beamline by a quadrupole triplet and transported inside the beamline under the restraint of bending magnets and a superconducting solenoid magnet. Inside the beamline, the decay muons were obtained through the in-flight decay of the negative/positive pions. These decay muons are confined by a solid longitudinal magnetic field of several teslas from a superconducting solenoid magnet. Three quadrupole triplets and two bending magnets were used to select the muons momenta and transport them to the experimental area.

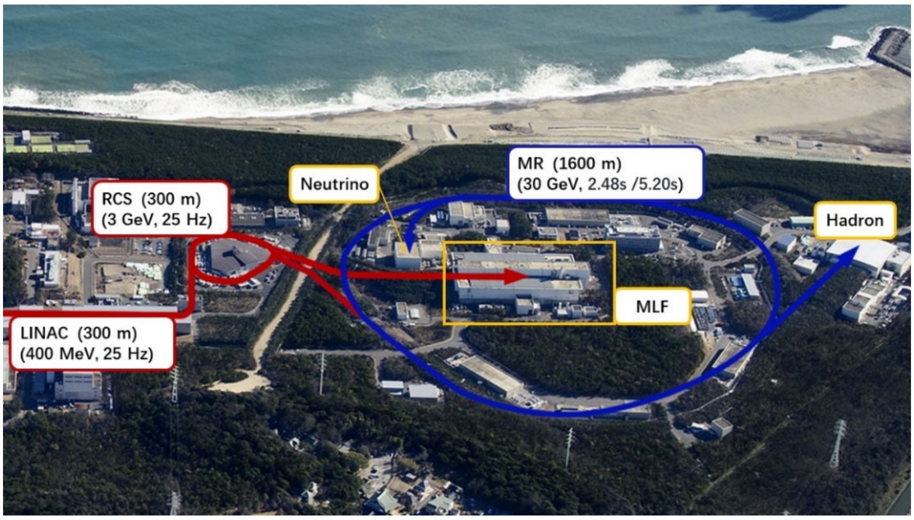

Figure 2.1 Aerial shot and facilities layout in J-PACR. The shot is from [57]. The layout and accelerator information is taken from [58].

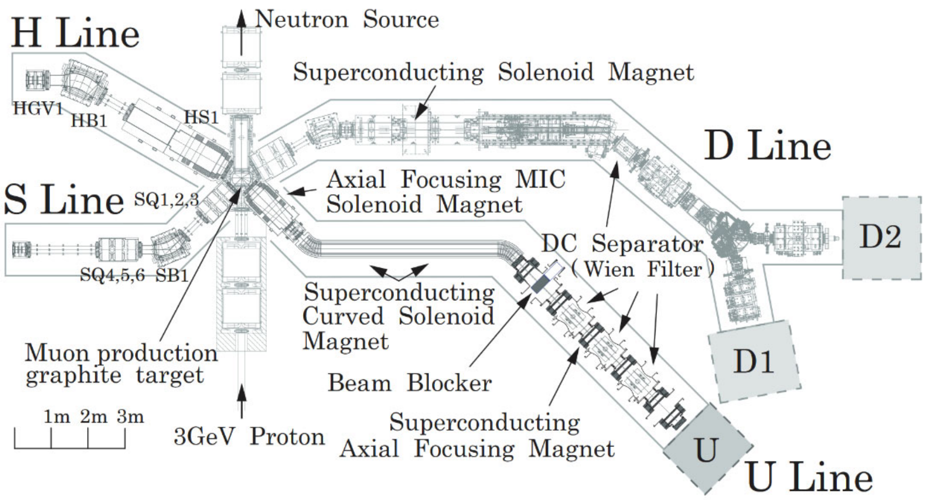

Figure 2.2 Layout of the Muon Science Facility (MUSE) in MLF, J-PARC. The layout is taken from [56].

The main properties of the decay muon beam in the D line are shown in Table 2.1. The D line provides muons ranging from 2 MeV to 54 MeV. The energy distribution of the muon beam can be approximated as a Gaussian distribution. The standard deviation in energy (σ) is reported to average 9.6% (5% in momentum) for 34-MeV/c to 44-MeV/c muons [8] and to average 6.38% for 2-MeV to 54-MeV muons [55]. The temporal width of the pulsed muon beam was reported to be 100 to 130 ns [55]. In summary, intense and high-quality negative and positive muon beams are available in the D line over a wide range of energy. Thus, the experimental data with high counting statistics can be taken in the facility during short irradiation time.

Table 2.1: main properties of the decay muon beam in the D line [55]

	Decay muon (μ±)
Beam Energy Range	2 – 54 MeV
FWHM (σ)	15% (6%)
Pulse Width	100 – 130 ns
Pulse Interval	40 ms
Beam Size	70 mm × 70 mm
Beam Intensity	10^6 – 10^7 /s

The device board used in the irradiation tests is shown in Figure 2.3. Four by four SRAM chips were mounted on the device board and packaged in ellipsoidal resin. The thickness of resins is not spatially uniform and averages 0.935 mm [59]. Each SRAM chip was fabricated in 65-nm bulk CMOS technology, of which structure is shown in Figure 2.4. It contains 42 SRAM test element groups (TEGs), and each TEG has 32 kbit cells. The cells are arranged in 64 BL × 512 WL, and the cells in every 2 BL × 64 WL share the same well, where BL and WL stand for Bit Line and Word Line, respectively. Thus, an SRAM chip contains about 12 Mbit cells.

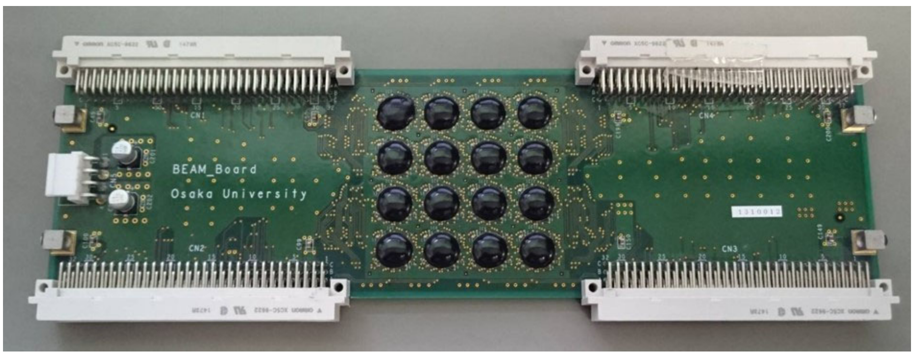

Figure 2.3 Actual picture of the Device board Under Test (DUT).

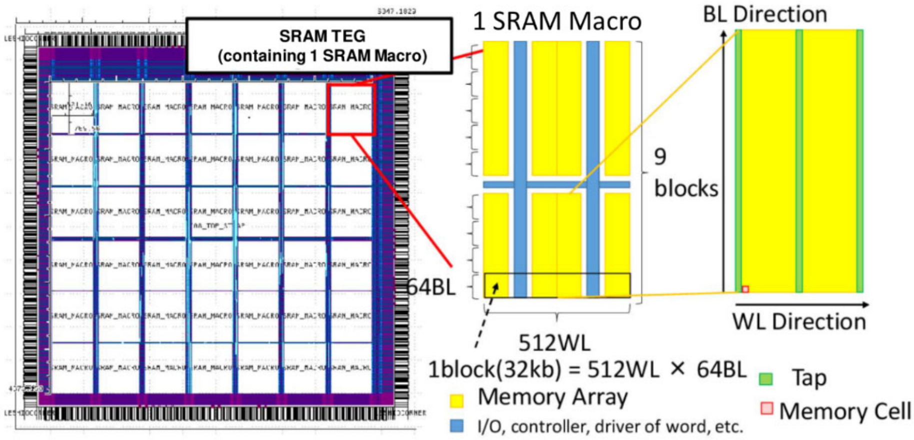

Figure 2.4 Structure of SRAM chip under test. For each chip, there are 42 SRAM TEGs. Each TEG contains a 32-kbit SRAM macro. The figure is taken from [8]

2.2.2 Experiment Layout in Different Irradiation Sides

Irradiation tests with negative and positive muons were all performed using the D2 experimental area at J-PARC Muon Facility, MUSE. The experimental layout is schematically illustrated in Figure 2.5. The device board was placed perpendicular to the beam direction and irradiated on the PS and BS sides. All experimental setups described below are the same for both PS and BS irradiation tests, except for the orientation of the device board.

The device board was located at a 340 mm distance from the beam exit. A 155 mm thick beam collimator was placed 35 mm before the device board. The structure is shown in Figure 2.6, and a detailed description of the collimator can be found in Manabe's doctoral thesis [60]. The collimator consists mainly of lead and aluminum. All inner and the front surfaces of the lead block slit were covered with the 5 mm thick aluminum (Al) plates to suppress the emission of the background particles (e.g., neutrons and light ions) from the negative muon capture in the high-Z material lead. The collimator slit allows the muon beam to irradiate only 3 by 4 SRAM chips, framed in red in Figure 2.5. The other 1 by 4 left SRAM chips served as a reference, confirming that the effect of background radiations on SEU was negligible.

Two kinds of detectors, namely a plastic scintillator and two germanium detectors, were placed downstream of the device board during SEU irradiation tests. The details of the detectors will be described in Subsection 2.2.4. A VLSI tester was placed in the experimental area and connected to the device board to read/write the stored data in the SRAMs. Figure 2.7 shows a photograph of the experimental setup during irradiation tests.

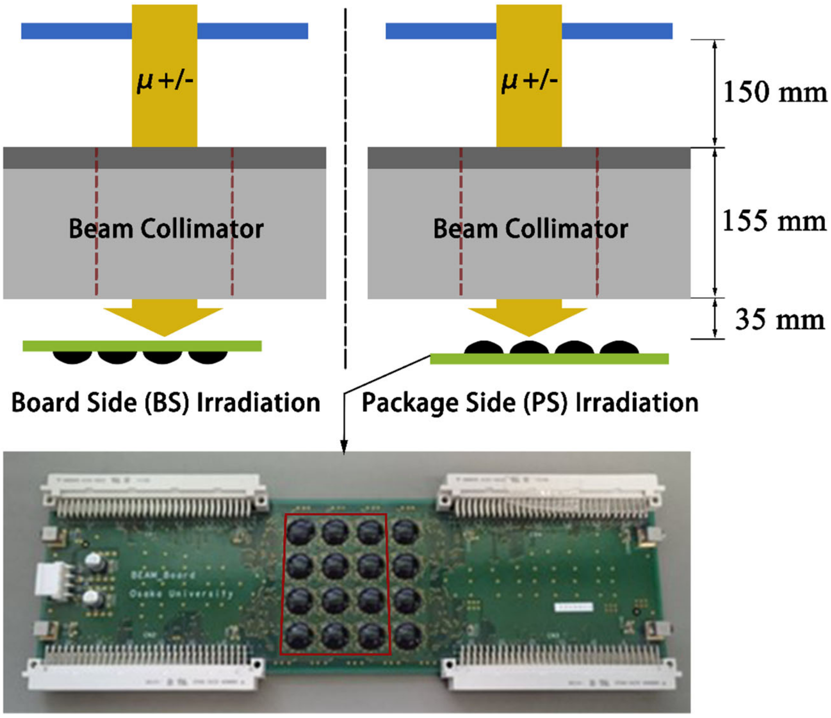

Figure 2.5 Overall layout of the experimental setup in the irradiation tests. The red frame notes the irradiated chips.

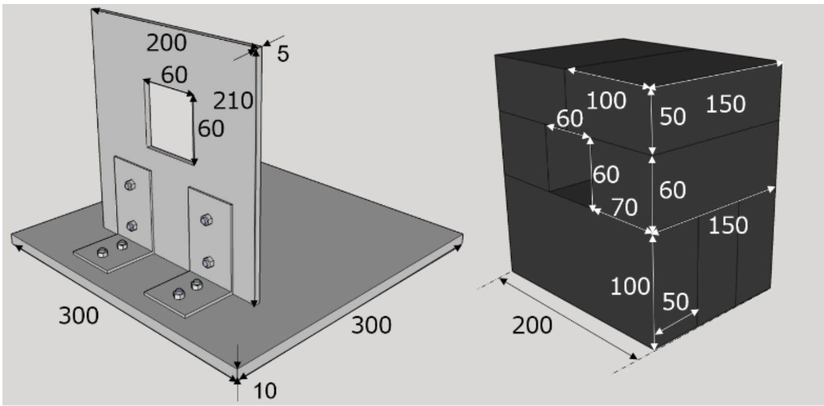

Figure 2.6 Schematic illustration of the beam collimator, which consists of an aluminum (Al) front plate (left) and lead blocks (right). The units of length are [mm]. [60]

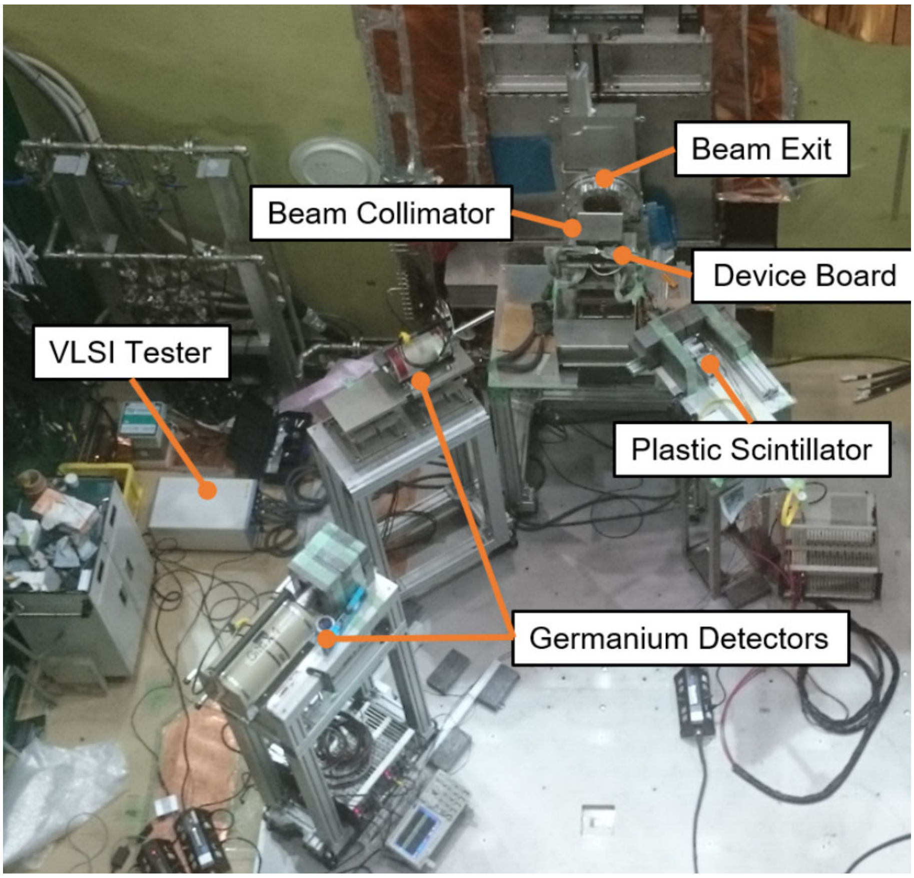

Figure 2.7 Photograph of the experimental setup during irradiation tests [60].

2.2.3 Measurement of SEU Cross Sections

The irradiation test is regarded as a static test, and the measurement procedure is shown in Figure 2.8 and described as follows. First, the SRAM memories were initialized by writing a data ‘0’ before each irradiation began. Then, the SRAMs were turned into a “holding” state at a supply voltage of 0.5 V. The muon beam irradiated at the test device during this “holding” state [45]. Beams of positive and negative muons are from 24 MeV/c to 36 MeV/c for the PS irradiation and 34 MeV/c to 42 MeV/c for the BS irradiation. After irradiation time, the data in memories were read. Once the stored data in a memory cell was changed to “1”, an upset was counted. Finally, the SEU cross section $\sigma_{<SEU>}$ was derived by:

$$\sigma_{<SEU>}[\mathrm{cm}^2/\mathrm{Mbit}] = \frac{N_{SEU}}{\Phi[cm^{-2}]\,N_{bit}[\mathrm{Mbit}]}, \quad (2\text{-}1)$$

where N_{SEU} is the number of recorded SEUs in the irradiation tests, N_{bit} is the number of memory bits in the device with a unit of Mbit, Φ is the total fluence of incident muons during the test which was obtained using the intensity of the pulsed muon beam. Note that the beam intensity was measured by different methods in BS and PS irradiation tests, which will be detailed in Sections 2.2.4 and 2.3, respectively.

Moreover, only 0.02% of the total SEU events were observed in the four unirradiated reference chips during the muon irradiation tests. This confirms that other background particles, e.g., neutrons from other beamlines in MLF and secondary cosmic rays, can be ignored.

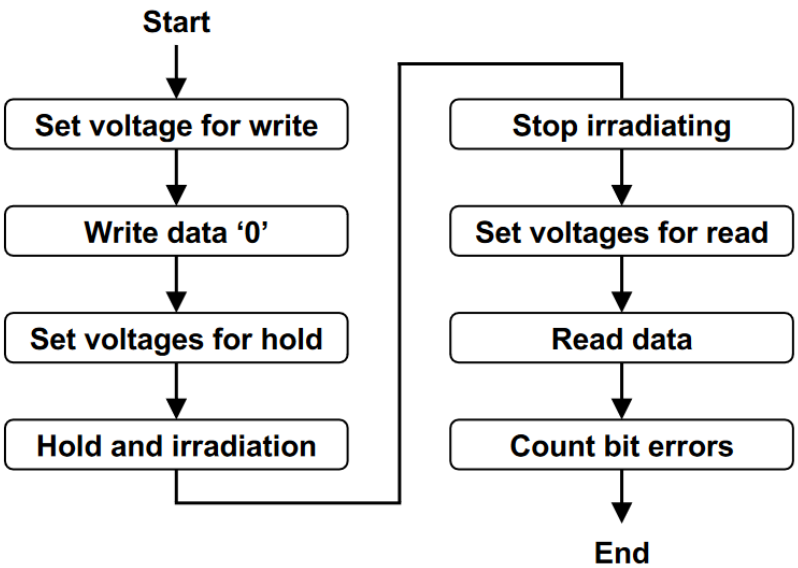

Figure 2.8 Flow chart of the muon irradiation process [45].

2.2.4 Measurement of Beam Intensity in BS Irradiation Tests

In the BS irradiation tests, the absolute value of muon beam intensity is measured by a counter telescope consisting of two plastic scintillators that detect the decay electrons/positrons of negative/positive muons. The experimental setup for muon flux measurement is shown in Figure 2.9. Since the beam intensity measurement in BS irradiation was performed and analyzed by Dr. Manabe, whose Ph.D. thesis [60] contains a detailed description, a brief description follows.

The capture rate of negative muons depends on the elements in the target. Therefore, the device board is replaced by an aluminum plate during the flux measurement because the complex material elements in the device board make the ratio of decay electrons to the muon flux cannot be calculated. The 100-mm thick piled-up lead blocks with a 50 mm × 30 mm slit were placed before the scintillators to shield the background radiation, shown in Figure 2.10.

The plastic scintillators were 2 mm thick and were placed 600 mm from the device board at an angle of approximately 37 degrees. They were made by a BC400 scintillator, of which the photograph is shown in Figure 2.11, and the general properties are listed in Table 2.2. The distance between them was 100 mm. When a decay electron/positron passes through each plastic scintillator, it deposits the energy and produces scintillation light in the scintillator. The light was converted to electrical pulses by photomultiplier transistors (PMTs) connected to each scintillator. Finally, two plastic scintillators measured the decay electrons/positrons by coincidence counting.

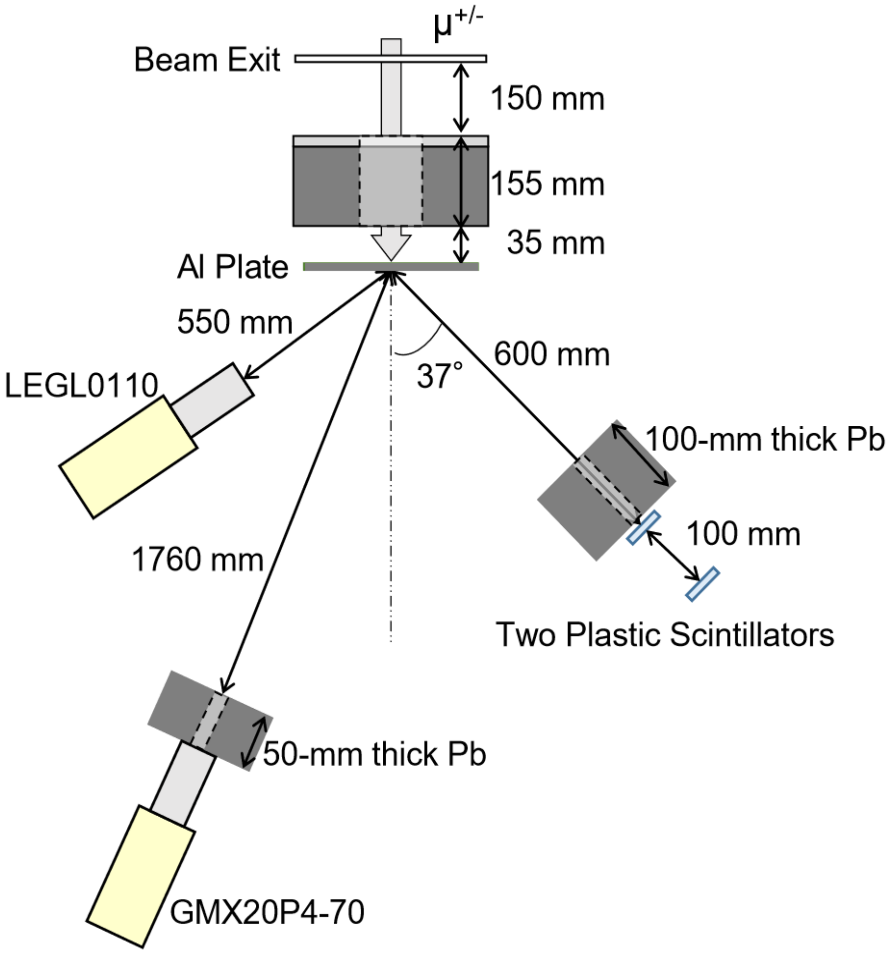

Figure 2.9 Experimental setup during the measurement of beam flux in BS irradiation tests [60].

Table 2.2: Main properties of the scintillator used in counter telescope

Scintillator Type	BC400
Base	Polyvinyl toluene
Composition formula	$-CH_2CH(C_6H_4CH_3)_n-$
Density[g/cm^3]	1.032
Size	25 mm × 25 mm × 2 mm

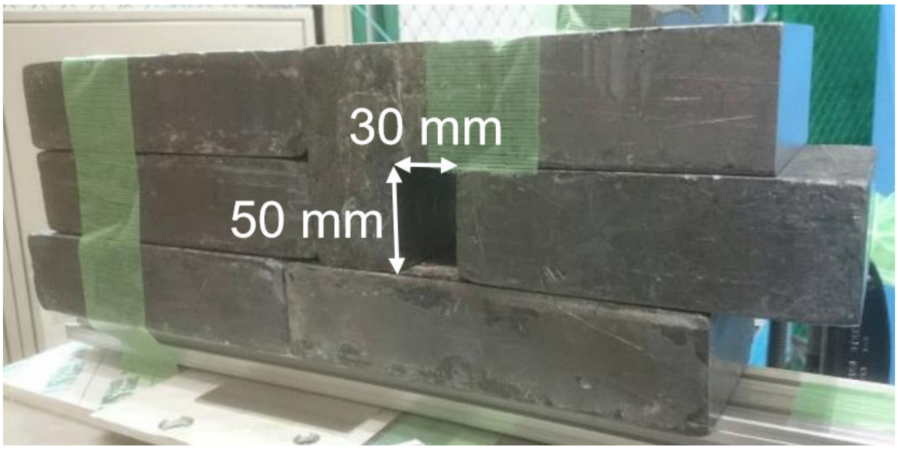

Figure 2.10 The lead blocks as the collimator of the plastic scintillators during the measurement of beam flux in BS irradiation [60].

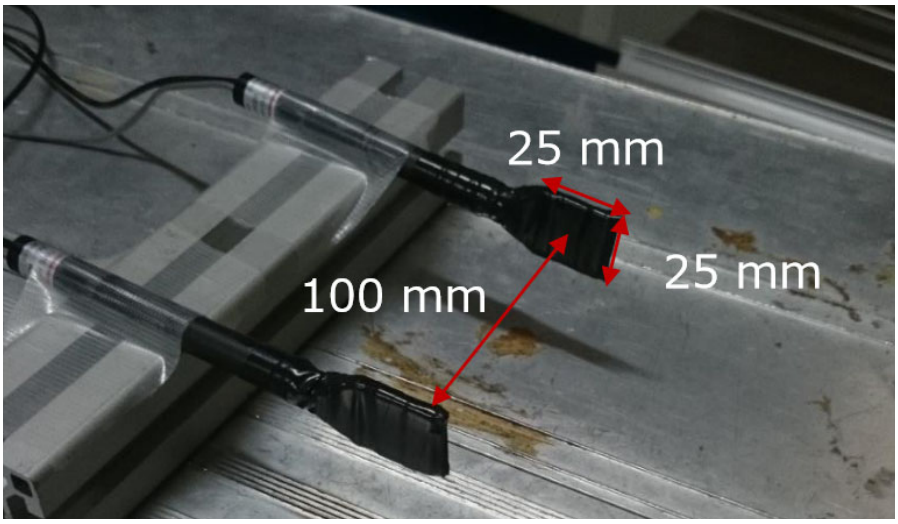

Figure 2.11 Photograph of the two plastic scintillators used in the counter telescope to measure beam flux in BS irradiation [60].

2.3 Beam Intensity Analysis on Package Side Irradiation Tests

The beam intensity measurement in PS irradiation differs from that in BS irradiation. The counter telescope composed of plastic scintillators was not used, and no absolute value was measured in PS irradiation. Alternatively, a beam profile monitor measured the relative muon intensity [61] in momentum steps of 2 MeV/c under both the PS and BS irradiations. Then, the relative intensity measured with the beam profile monitor was normalized to the absolute intensity measured with the counter telescope in BS irradiation at 34 MeV/c. The measured data from the beam profile monitor were fitted by a cubic function over the momentum range of 24 to 44 MeV/c. The result is shown in Figure 2.20. Finally, the muon intensities from 24 MeV/c to 36 MeV/c under PS irradiation were obtained by fitting the curves. The beam flux analysis of the PS irradiation case was newly performed in this study. The measurement method is detailed in the following subsection 2.3.1.

2.3.1 Image Luminance of the Beam Profile Monitor Output

The beam profile monitor consists of a scintillation screen and UVT acrylic blocks in a light-tight polyvinyl chloride (PVC) tube for light shielding, which structure is shown in Figure 2.12. A round-shaped scintillation screen (130 mm in diameter and 2 mm thick) was made of an EJ-212 plastic scintillator [62]. When muons interact with the scintillator, the scintillation light is generated from the deposited energy. A two-dimensional muon beam profile can be measured as a CCD camera image. The device board was removed during the beam profile measurement, and the profile monitor was placed behind the beam collimator. The layout of the relative muon flux measurement is shown in Figure 2.13.

Figure 2.14 shows a measured two-dimensional profile image of the beam intensity for a positive muon beam of 36 MeV/c. The beam intensity increases toward the center, shaped like a square, due to the beam collimator slit. The bright pixels in the ring area marked with **T** come from the leakage lights in the connection position between the light transport tube and the CCD Relay lens. The brightness values in the integration area (region **I** in Figure 2.14) are integrated after background noise subtraction by:

$$L = \sum_{p \in \mathbf{I}} L_p - \frac{n_{\mathbf{I}}}{n_{\mathbf{B}}} \sum_{p \in \mathbf{B}} L_p , \tag{2-2}$$

where L_p represents the brightness at pixel point $p(i,j)$, $n_{\mathbf{I}}$ is the number of pixels in the integration area **I**, and $n_{\mathbf{B}}$ is the pixel number in the background area. The background area is designated as **B = U-I-T** and marked in Figure 2.14. Taking Figure 2.14 as an example, the integral brightness is 2.014×10^9 ADU, where ADU is the grayscale unit. This integrated brightness is related to the muon beam intensity.

Brightness integration was performed on the monitor output images from 24 to 44 MeV/c in steps of 2 MeV/c. The results are shown in Figure 2.15. The errors in integral brightness come from two primary parts. On the one hand, the relative error caused by the statistical error of the number of photons to CCD can be calculated by:

$$\sigma_{ph} = \frac{1}{\sqrt{\sum_{p \in \mathbf{I}} n_{\gamma p}}} = \frac{1}{\sqrt{\sum_{p \in \mathbf{I}} \frac{L_p \cdot gain}{QE}}}, \tag{2-3}$$

where $n_{\gamma p}$ is the number of photons to pixel point $p(i,j)$, and QE is the quantum efficiency of which unit is "photon/electron." And the unit of *gain* is "electron/ADU." Since there are 62,500 pixels in the integration region, even averaging one photon per pixel, this error is only 0.4%. Thus, this error can be ignored in the measurement.

On the other hand, the relative error caused by the estimation of background brightness can be expressed by:

$$\sigma_b = \sqrt{\frac{1}{n_B - 1} \sum_{p \in \mathbf{B}} \left(L_p - \bar{L}_{\mathbf{B}} \right)^2}, \tag{2-4}$$

where the $\bar{L}_{\mathbf{B}}$ is the average brightness of the pixel points in the background area. Taking Figure 2.14 as an example, the relative error caused by the estimation of background brightness is 2.8%.

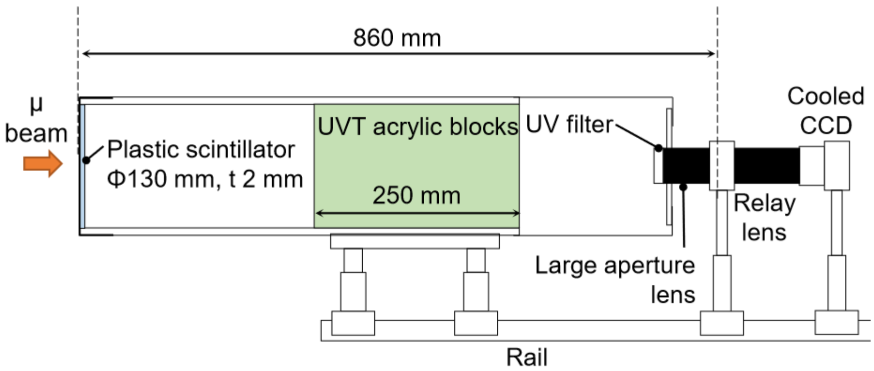

Figure 2.12　Schematic drawing of the beam profile monitor [60].

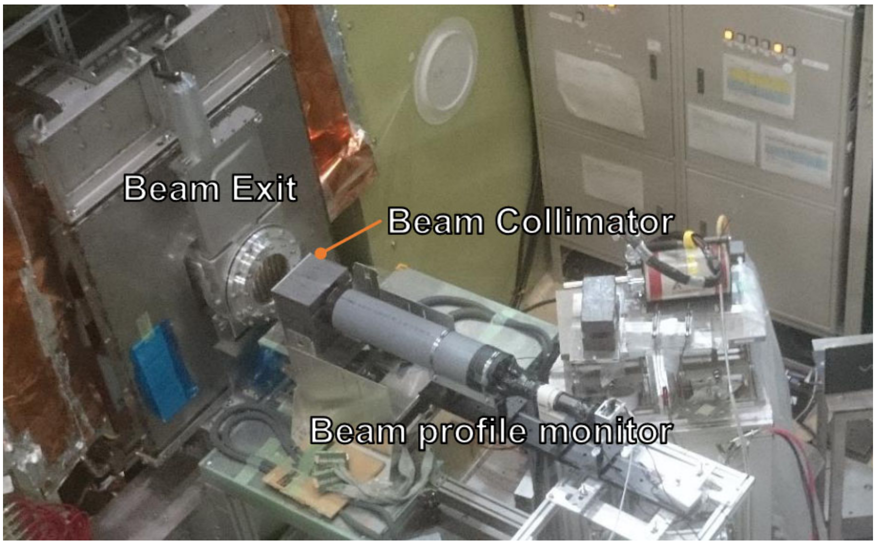

Figure 2.13 Layout of the relative muon flux measurement [60].

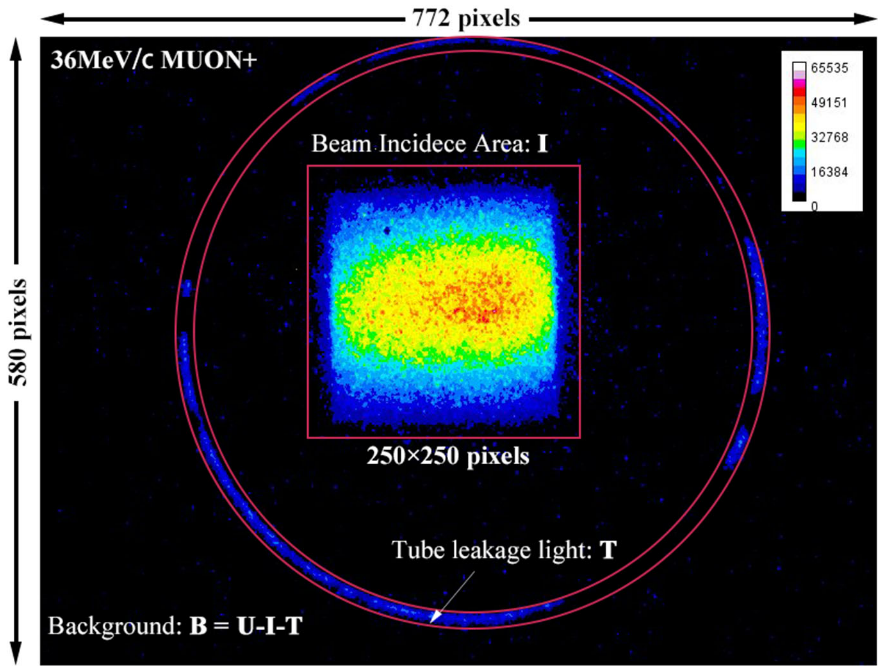

All pixels in figure: **U** = $\{p(x,y) \mid 0 \le x \le 772 \ \&\ 0 \le y \le 580\}$

Beam incidence area: **I** = $\{p(x,y) \mid 247 \le x \le 497 \ \&\ 119 \le y \le 369\}$

Tube leakage light: **T** = $\{p(x,y) \mid 260 \le (x-400)^2+(y-271)^2 \le 275\}$

Figure 2.14. A two-dimensional profile image of the beam intensity for a positive muon beam of 36 MeV/c.

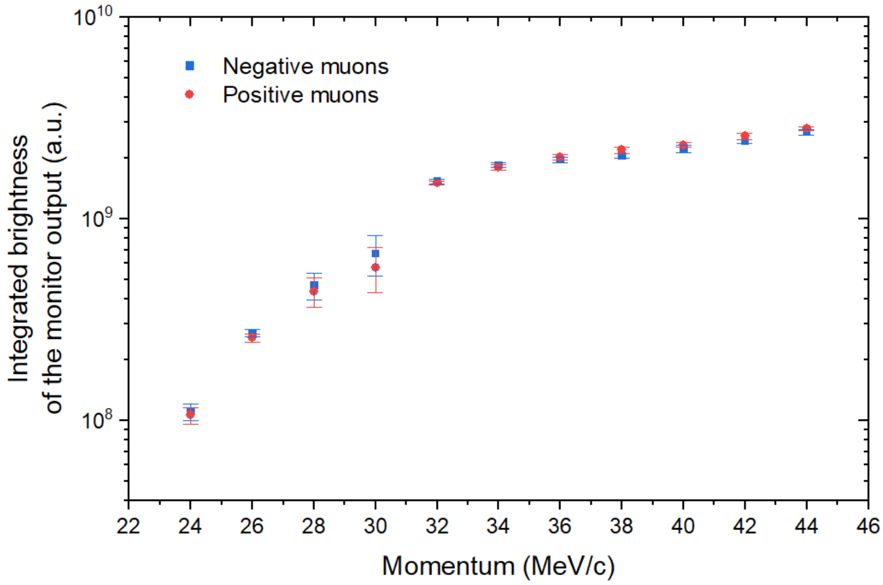

Figure 2.15 Momentum dependence of the integrated brightness L of the beam profile images.

2.3.2 Beam Intensity Derivation Considering Birks Effect

The integrated brightness L in Figure 2.14 is proportional to the number of generated photons in the scintillator. To convert L to the relative beam intensity, the non-linear response of organic scintillators (the Birks effect [63], [64]) should be considered. The number of generated photons in the scintillator per incident muon, i.e., N_{ph}, can be expressed by:

$$N_{ph} = \int_0^d \frac{Y_0 \frac{dE}{dx}}{1 + kB \frac{dE}{dx}} dx, \tag{2-5}$$

where kB is the Birks constant, d is the scintillator thickness, dE/dx is the ionization density, and Y_0 is the absolute light yield, which is 10050 photons/MeV for EJ-212 scintillator according to [65].

The photon productions of the EJ-212 plastic scintillator for muons with different momentums were simulated by Geant4. The scintillator with the same material and size was modeled and set to the same distance to the beam exit as the measurement. A collimator identical to the experiment was also placed between the scintillator and the beam exit in the simulation. The ionization densities dE/dx of muons were evaluated over the momentum range shown in Figure 2.15, and kB was set to 13.2 mg/(cm^2·MeV) from [64]. The results for positive and negative muons are shown in Figure 2.16.

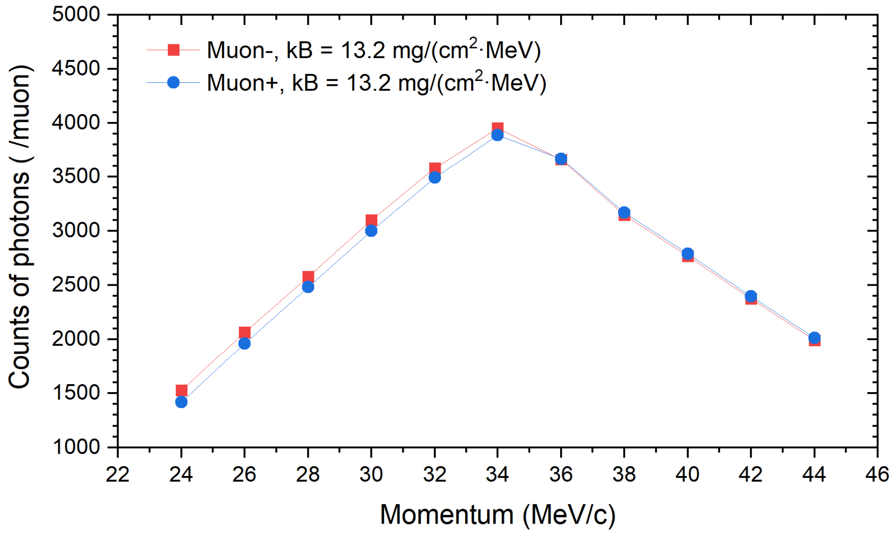

Figure 2.16. Simulated photon productions N_{ph} in the scintillator for incident muons with different momenta.

The slope of the curves in Figure 2.16 is changed at 34 MeV/c because the muons above 34 MeV/c pass through the scintillator, and the deposited energy decreases with increasing momentum. Finally, the relative beam intensity was obtained using

$$I_{rel}(p_\mu) = \frac{L(p_\mu)}{N_{ph}(p_\mu)}, \tag{2-6}$$

where p_μ is the momentum of the muon, L is the integrated brightness in Figure 2.15, and N_{ph} is the number of photon production per muon in Figure 2.16.

In addition, the photon production at the upper and lower limits of the kB value is also simulated to estimate the relative muon intensity error resulting from the kB value selection since there is a relative error of 18.9% in the kB value [64]. This error is marked with σ_{kB}.

2.3.3 Temporal Distribution of Pulsed Beam Intensity

The time origin is equal to the arrival time of the pulsed proton beam, then the delay of the CCD camera shutter in beam profile monitor to the time origin is referred to as the shutter time in this study. Because the beam is pulsed, the relative muon intensity calculated from the profile monitor will be distributed with the shutter time of the CCD camera. Only with the integral brightness measured at the shutter time corresponding to the peak flux, we calculate the accurate relative beam intensities in the tests with different momentums, as shown in Figure 2.16. Thus, the beam intensity distribution concerning shutter time was measured at each momentum point. Some of the results are shown in Figure 2.17.

The flux distribution with the shutter time at a specific muon momentum is assumed to be a Gaussian distribution, which is described as:

$$I_{rel}(t) = I_{rel}(t_c)e^{-\frac{(t-t_c)^2}{2\delta^2}}, \tag{2-7}$$

where $I_{rel}(t_c)$ represents the relative beam intensity at any shutter time t, t_c represents the shutter time at peak intensity, and δ is the standard deviation of the muon beam pulse. The beam width (FWHM) is set to 0.102 μs to make the flux distribution reproduce the measurement best. The corresponding standard deviation was 0.043 μs. Figure 2.17 shows that the Gaussian distribution agrees well with the measured temporal distribution, especially the temporal distribution at 32 MeV/c.

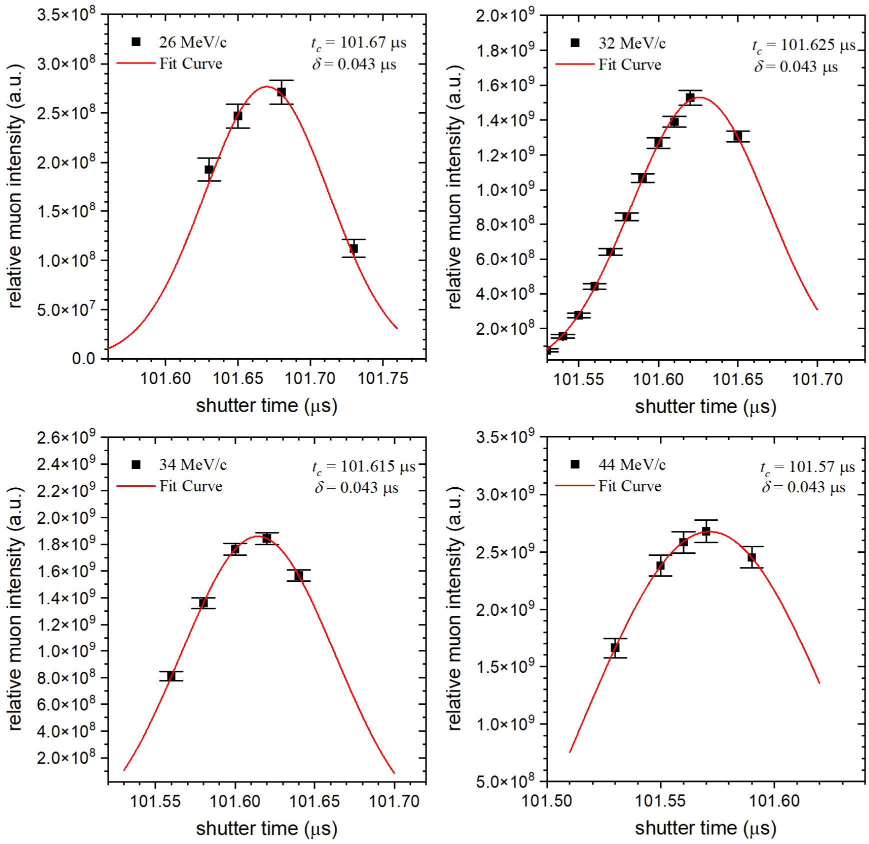

Figure 2.17 The temporal distribution of relative negative muon intensity at 26, 32, 34, and 44 MeV/c.

However, limited data at different shutter times were available for the measurements taken at the 28-MeV/c and 30-MeV/c muons during package tests. Therefore, the available measured data in the non-peak region and the known Gaussian distribution were used to estimate the relative muon intensity at 28 MeV/c and 30 MeV/c, as shown in Figure 2.18. The peak shutter time of the Gaussian distribution at 28 MeV/c and 30 MeV/c in Figure 2.18 were estimated as follows.

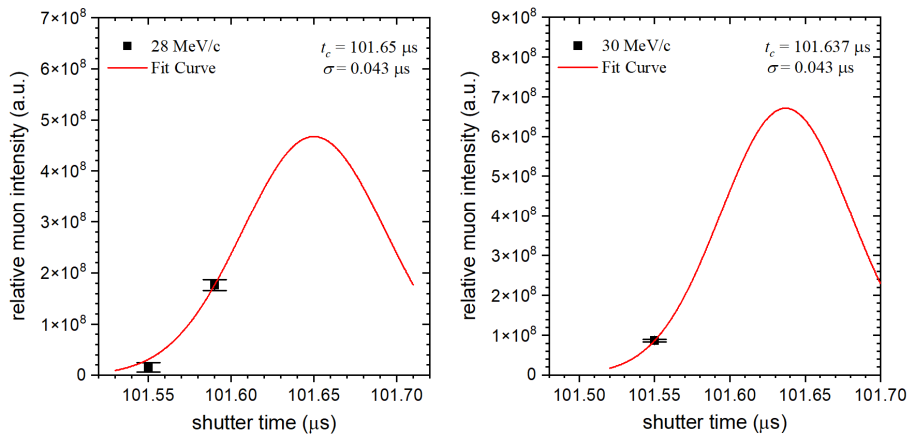

Figure 2.18 The estimation of relative negative muon intensity in peak shutter time at 28 and 30 MeV/c.

The shutter time at the peak muon intensity varies at different muon momentum. Because π mesons decay produces the muons in the D line, both have different transport times at a fixed flight distance when their velocity is different. For a given muon momentum p_μ, their peak shutter time can be described by:

$$t_c(p_\mu) = T_0 + \frac{L_{eff}}{c}\sqrt{\frac{m_\mu^2 c^2}{p_\mu^2} + 1}, \tag{2-8}$$

where T_0 is the time when π mesons are released from the surface of the graphite target, the second term represents the flight time of the muons, where m_μ is the rest mass of muons, c is the speed of light, and L_{eff} means the effective flight length of the muons. Adjusting L_{eff} to 18.5 m and setting T_0 to 101.411 μs, the calculated peak shutter times best match the measured ones. The comparison is shown in Figure 2.19. The red and blue points are the peak times obtained in the measurements, and the green curve shows the peak times obtained from the calculations with equation (2-8). The calculation generally agrees with the measurement.

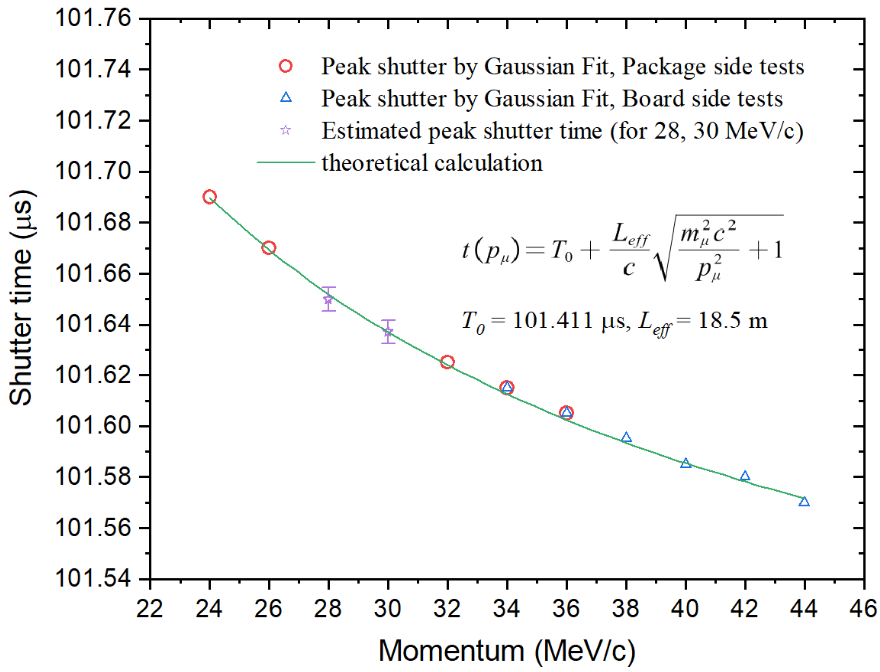

Figure 2.19 Comparison of peak shutter times obtained from theoretical calculations and measurements.

The relative error of the estimated peak shutter time at 28 and 30 MeV/c is obtained from the variance of the measured values from the calculated ones. The error of relative beam intensity resulting from the estimation of the peak shutter time at 28 and 30 MeV/c is calculated by

$$\sigma_t = \frac{I_{rel}(t_{up}) - I_{rel}(t_{down})}{I_{rel}(t_c)}, \tag{2-9}$$

where $I_{rel}(t_c)$ is the estimated relative muon intensity when using the estimated peak shutter time t_c in Figure 2.19 for 28-MeV/c and 30-MeV/c muons, and t_{up} and t_{down} are the upper and lower error limits of the estimated peak shutter time for 28-MeV/c and 30-MeV/c muons in Figure 2.19.

2.3.4 Results of the Derived Muon Beam Flux

After integrating image brightness from the beam profile monitor and converting the integral brightness to relative beam intensity, the relative beam intensities at peak shutter time are calculated from temporal distribution as the measurement result of relative muon beam intensity. They are normalized to the absolute measurement by the counter telescope at 34 MeV/c for both positive and negative muon. The results are shown in Figure 2.20.

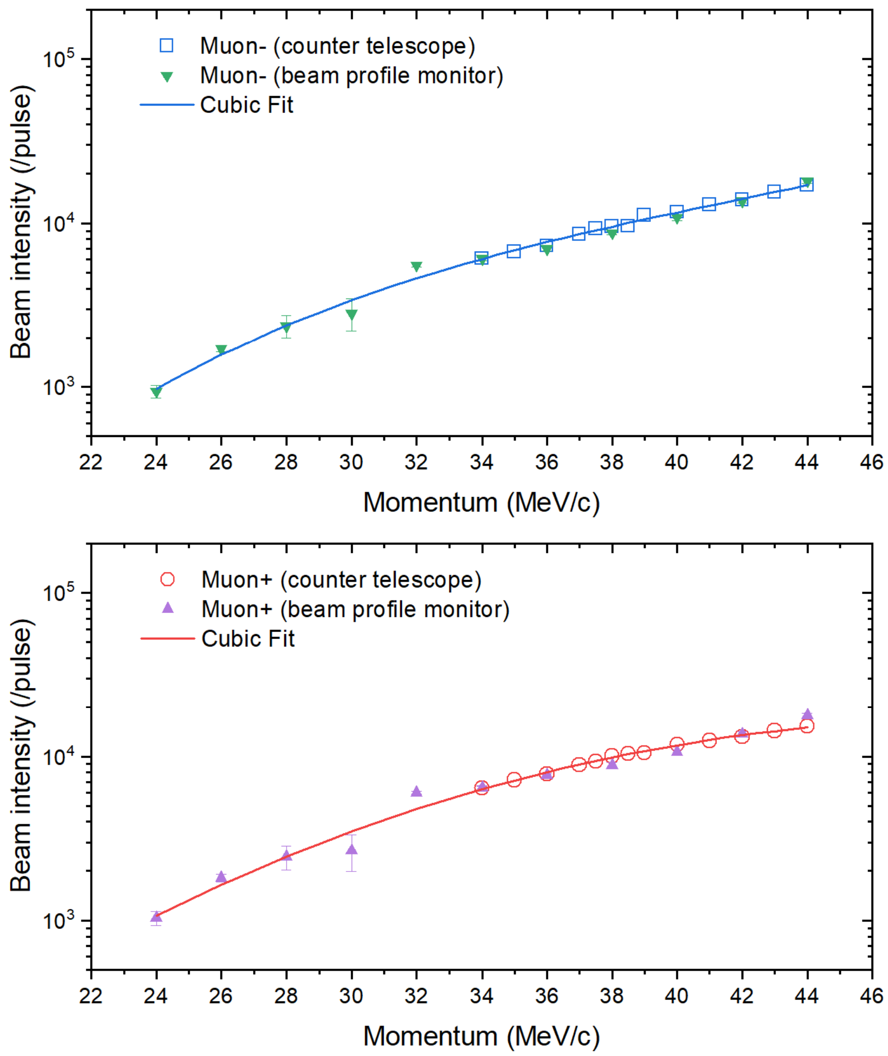

Figure 2.20. Measured intensities of the pulsed muon beams with the two different methods. The cubic fitting curves based on the measured data are also given. The upper and lower panels show the positive and negative muon intensity, respectively.

Furthermore, it should be noted that the relative error of the muon intensity measured by the beam profile monitor in Figure 2.20 is calculated by:

$$\sigma_I = \sqrt{\sigma_b^2 + \sigma_{kB}^2 + \sigma_t^2}\,, \tag{2-10}$$

where σ_t is 0 for all the momentum points except at 28 and 30 MeV/c.

2.4 Results of the Irradiation Tests

Irradiation tests with negative and positive muons were performed in the momentum ranges from 24 to 36 MeV/c in PS irradiation and 34 to 44 MeV/c in BS irradiation. All SRAMs were operated at a supply voltage of 0.5 V during the tests. The experimental results of positive and negative muon-induced SEU cross sections for 65-nm bulk SRAMs with PS and BS irradiations are plotted as a function of momentum with colored symbols in Figure 2.21. Since the muon beam had distribution in momentum, the experimental result at momentum *p* shown in Figure 2.21 is defined as momentum-averaged SEU cross section $<\sigma_{SEU}(p)>$ by

$$<\sigma_{SEU}(p)> = \frac{\int \sigma_{SEU}(p')G(p',p)\,dp'}{\int G(p',p)\,dp'} \tag{2-11}$$

where $G(p', p)$ is the Gaussian distribution of incident muons fluence with the momentum p' in the irradiation test with the mean momentum p, and $\sigma_{SEU}(p')$ is the mono-energetic muon SEU cross-section at the momentum p'.

From Figure 2.21, both the SEU cross-sections show a broad peak structure. The peak cross-section for negative muons is about 9 times that for positive muons in both the PS and BS irradiations. The nuclear capture process by negative muons releases many secondary charged particles, making SEUs more significant than positive muons.

The peak of the SEU cross-section in the BS irradiation tests appears at 38 MeV/c, which is much higher than that in the PS irradiation tests, i.e., 28 MeV/c. The peaks for negative and positive muons appear near the end of the track due to the muon capture and the Bragg peak, respectively. Thus, different penetration depths in PS and BS irradiation can explain the different SEU peak positions. In BS irradiation, the muon needs to pass through much more material thickness to reach the SV than in PS irradiation. The thickness and composition of each layer in the SRAM structure will be introduced in the simulation analysis in Chapter 3.

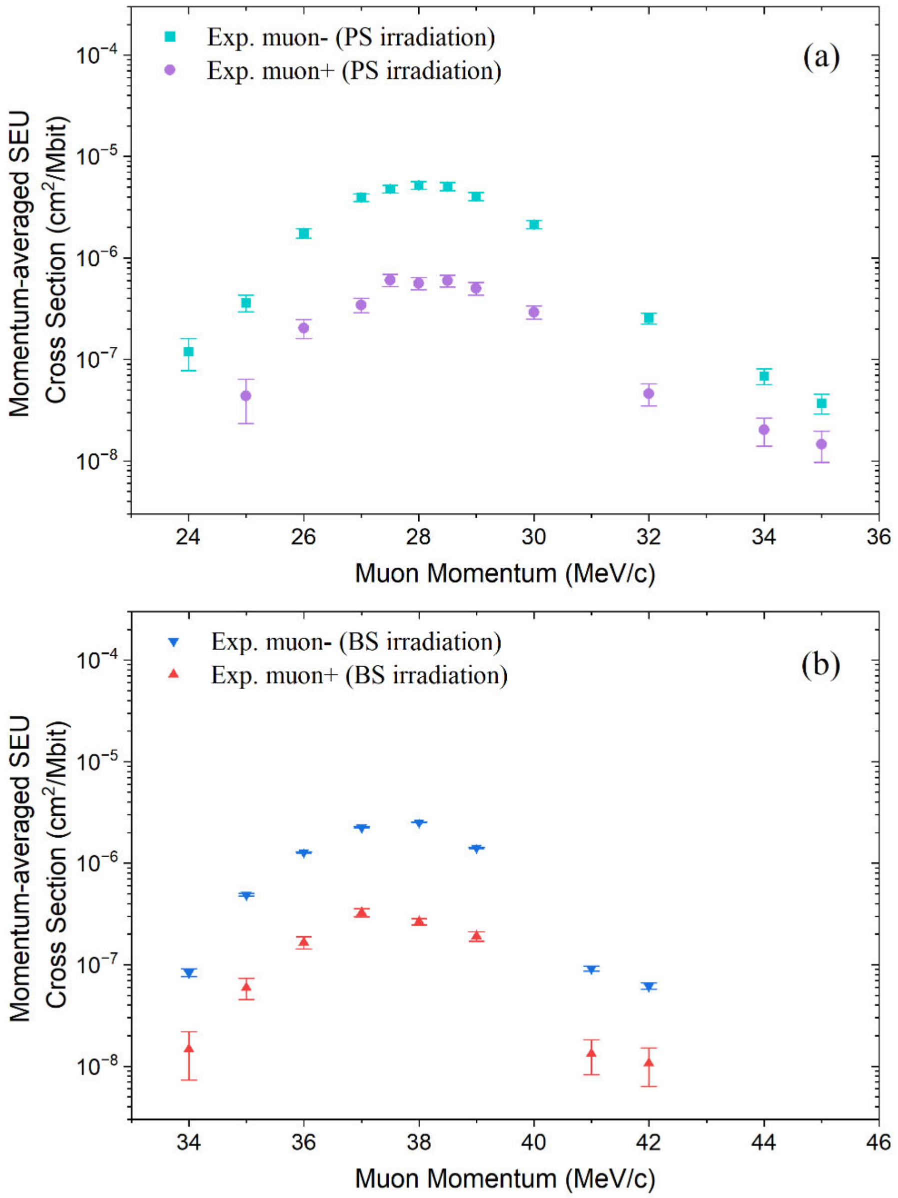

Figure 2.21 Panel (a) shows the measured and simulated positive and negative muon SEU cross sections of 65-nm bulk SRAM for the PS irradiation test, while panel (b) shows those for the BS irradiation test.

Moreover, the peak SEU cross-section of the PS irradiation is about twice that of the BS irradiation. The ratios of the peak SEU cross-sections for the PS and BS irradiations are given by

$$k_{CS-} = \frac{\sigma_{p-}}{\sigma_{b-}} = 2.06 \pm 0.18\,, \tag{2-12}$$

$$k_{CS+} = \frac{\sigma_{p+}}{\sigma_{b+}} = 2.13 \pm 0.33\,, \tag{2-13}$$

for negative and positive muons, respectively. In equations (2-12) and (2-13), σ_{p-} and σ_{b-} denote the peak SEU cross-section for negative muon PS and BS irradiation, respectively. Similarly, σ_{p+} and σ_{b+} represent the peak SEU cross-sections for positive muon PS and BS irradiations, respectively. The errors are derived using the error propagation formula considering the systematic error of measured flux and the statistical error of SEU events number. These ratios of SEU cross-sections that exist between PS irradiation and BS irradiation will be explained by simulation analysis in Chapter 3. This is one of the primary topics in this study.

2.5 Conclusion

The positive and negative muon irradiation tests on 65-nm bulk SRAMs were performed previously. The result of PS irradiation tests is newly analyzed and compared with the previous work with BS irradiation.

After describing the other experimental setups in PS and BS irradiation tests, the different methods of beam intensity measurements for PS irradiation are presented. The luminance of the output photograph of the beam profile monitor is integrated and corrected for the nonlinear response of the scintillator as the relative beam intensity. The absolute values of beam intensity in the PS irradiation were obtained by normalizing the relative beam intensity at 34 MeV/c with that of the BS irradiation. By the analysis, the temporal distribution of muon beam intensity approximately follows a Gaussian distribution with a standard deviation of 0.043 μs. The shutter times at peak intensity calculated by equation (2-8) reproduce well with the measured ones.

The muon-induced SEU cross sections of 65-nm bulk SRAMs in both PS and BS irradiation tests show a broad peak structure. The peak cross section for negative muons is about 9 times that for positive muons in both the PS and BS irradiation. This can be explained by the nuclear capture process of negative muons releasing many secondary charged particles and making SEUs more significant than positive muons.

The peak of the SEU cross-section in the BS irradiation tests appears at 38 MeV/c, which is much higher than that in the PS irradiation tests, i.e., 28 MeV/c. Different penetration depths in PS and BS irradiation can explain the different SEU peak positions.

Moreover, the peak SEU cross-section of the PS irradiation is about twice as significant as that of the BS irradiation. The ratios of the peak SEU cross sections in the PS to that in BS irradiations are 2.06 for negative muons and 2.13 for positive muons, respectively. The ratios can be explained by different energy straggling due to different penetration depths, as described in Chapter 3.

3 Simulation Analysis on Measurement Results

3.1 Introduction

The previous muon irradiation tests of 65-nm bulk SRAMs have shown differences in SEU cross-sections between positive and negative muons and between PS and BS irradiation tests. To understand the physical mechanism of these results, Monte Carlo simulations were performed and compared with the measured results.

First, critical charge Q_c dependent SEU cross sections were analyzed, and the absolute values of the cross sections were compared with the experiments to get the most appropriate parameter values. The contribution of secondary particles released from negative muon capture to SEU numbers in simulation illustrates the difference in SEU cross sections between positive and negative muons. Then, momentum-dependent SEU sections were obtained by simulation and compared with experimental results to verify the validity of the simulations.

As introduced in section 1.4, the difference in magnitude of SEU cross-section between PS and BS irradiation tests can be explained qualitatively by the Bragg peak shape of different depths in Figure 1.12. To quantitatively explain the differences, the concept of an effective SEU fluence is defined and applied in detail in this chapter. Note that the effective SEU fluence was obtained by approximate calculation in previous work [66] to investigate the impact of energy straggling on SEUs, while we use simulation to get more accurate results in this thesis.

3.2 Simulation Method

3.2.1 Simulation Tools — Geant4

The particle transport Monte Carlo simulation toolkit Geant4 [21] was used for all simulations in this study. The origin of Geant4 development can be traced back to two studies independently at the European Organization for Nuclear Research (CERN) and the High Energy Accelerator Research Organization (KEK) in 1993. It is managed and maintained by CERN now.

Geant4 includes a complete range of functionality, including tracking, geometry, physics models, and hits. The physics processes offered cover a comprehensive coverage, including electromagnetic, hadronic, and optical physical processes, a large set of long-lived particles, materials, and elements over a wide energy range from several eV to the hundreds of TeV. Geant4 has been created by exploiting software engineering and object-oriented technology and implemented in C++. It has been widely applied in particle physics, nuclear physics, accelerator design, space engineering, and medical physics.

At the kernel of this toolkit is an abundant set of physics models to handle the interactions of particles with matter across an extensive energy range. Data and expertise have been drawn from many sources worldwide and continue to be refined. The object-oriented methods have allowed the users of Geant4 to effectively manage complexity and limit dependencies by defining a uniform interface and common organizational principles for all physics models.

In addition, because the open-source Geant4 gives three levels of user behavior interfaces, i.e., Run, Event, and Step, users can obtain and deal with many kinds of physical information freely by programming.

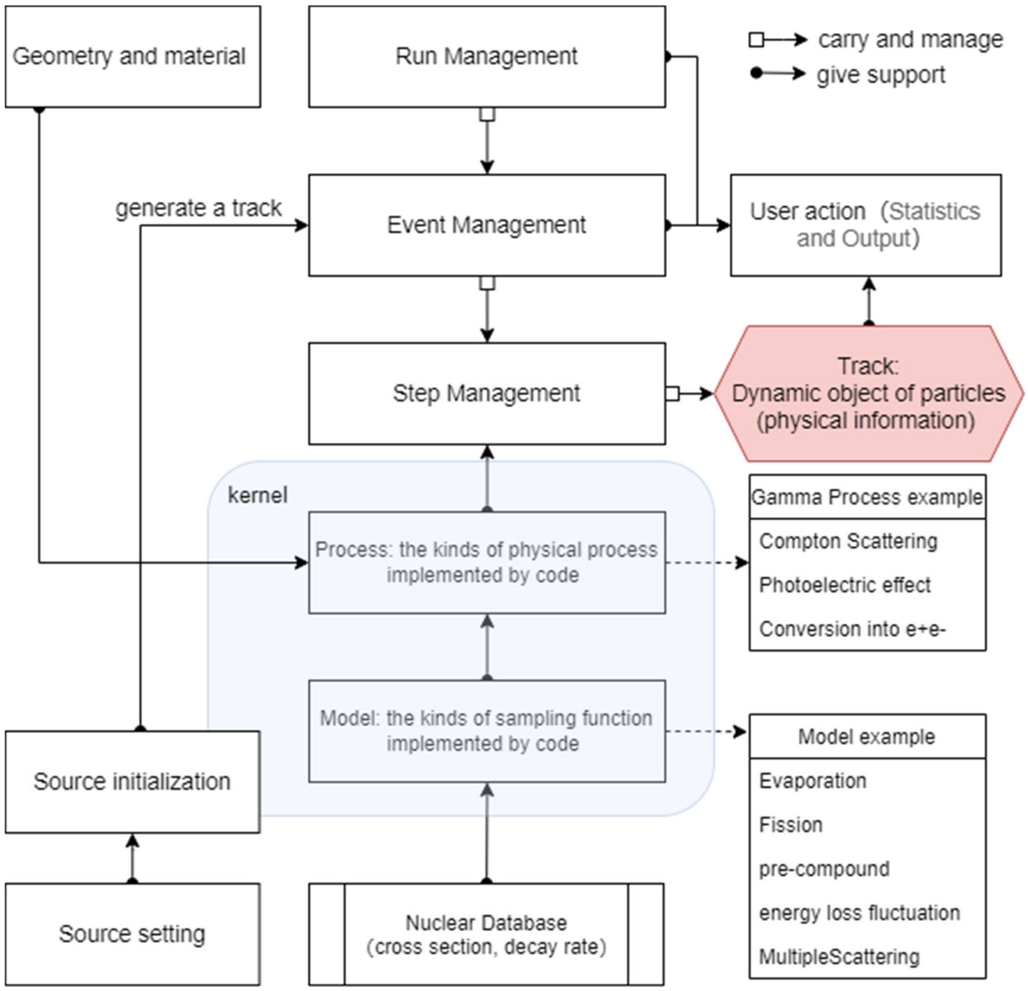

Figure 3.1 A structure diagram of the Geant4 toolkit.

3.2.2 Physical Process in Simulation

In the Geant4 simulation of muon-induced SEUs, direct ionization, multiple scattering, and decay processes were considered as the physical processes during the muon transport and energy deposition in matter for both negative and positive muons. On the other hand, for negative muons, secondary ions produced from nuclear capture have a significant impact on SEU. Therefore, a pre-compound model coupled with exciton and evaporation models was used to simulate the negative muon capture process. All the above physical processes and models are explained as follows.

A built-in physical process list named EM Opt4 (Electromagnetism Option 4) is in charge of simulating the electromagnetism processes, including ionization, multiple scattering, bremsstrahlung, etc. In this setting, ionization is implemented by several models depending on energy and particle type. From 0 to 200 keV, the Bragg model for $\mu+$ and the ICRU73Q0 parameterization for $\mu-$ derive the continuous ionization energy loss in a simulation step based on the stopping power data from [67], [68]. The Bethe-Bloch model calculates the ionization energy loss for $\mu+$ and $\mu-$ between 200 keV and 1 GeV, and the MuBetheBloch model calculates it from 1 GeV to 100 TeV. In all the above ionization models, sampling of emitted δ-electrons is carried out first. If the initial energy of the δ-electron exceeds a user-set cut value (T_{cut}), it is generated and tracked. Otherwise, all the energy loss is regarded as continuous, calculated by the Bethe-Bloch restricted energy loss formula [69] or derived from the experimental database. Then, the energy loss is floated by the sampling function of the energy straggling process. Because the energy deposition of δ-electrons influences the triggering of the SEU [18], the T_{cut} must be set so that the range of electrons with this energy is significantly smaller than the SV size.

The multiple Coulomb scattering is handled by the WentzelVI model [70] and a single scattering model based on the [71]. The G4MuonDecayChannel of the G4Decay class deals with the decay process of positive muon (μ+) according to V-A theory.

Muon capture or decay in orbit is handled by the G4MuonMinusCapture process. In Geant4 version 10.06 used in this study, the Bertini cascade model [72] is the default model handling the pre-equilibrium emission from a highly-excited nucleus formed after muon capture. Because the particle emission spectrum of this model did not agree well with the experimental data, this default setting was changed in this study. Therefore, a pre-compound model [73] coupled with exciton and evaporation models was used to simulate the de-excited emissions of the residual nucleus. This model has been built in the G4MuMinusCapturePrecompound class by V. Ivanchenko. Figure 1.10 in Section 1.3.2 shows the particle emission spectrum by the model and is compared with the measured results. It can be seen that the energy spectra of low-energy protons and various other particles are in good agreement with the experimental values, except for high-energy protons, which are significantly lower than the observed values.

3.2.3 Geometry Used in Simulation

The geometric model of the SRAM device in simulation is shown in Figure 3.2. The SRAM chip is covered by an ellipsoidal package and fixed on the device board. The profile of the SRAM chip is 2.4 × 2.8 mm rectangle. From bottom to top, it contains a 0.3-mm thick Substrate, a 0.4-μm thick Sensitive Layer, a 0.35-μm Insulation Layer, and a 2.43-μm Metal Wire Layer. The center depth of the ellipsoidal package is 0.935-mm. The device board is 10 × 10 mm square. A 2.8-cm square surface muon source is 340 mm from the SRAM cell. The 0.335-mm thick Board Resin covers both sides of the 0.93-mm thick Board Core. There is a 0.2-mm Prepreg Layer in each Board Resin. Therefore, the total thickness of the device board is 1.6 mm. The composition and density of the above structures are listed in Table 3.1 [59].

About 12-Mbit memory cells are evenly arranged in the sensitive layer. The sensitive volume (SV) inside the memory cell was defined as the source and drain regions under the gate of the off-state NMOS and PMOS. The schematic layout of the 2×2 SRAM cells layout in the 65-nm bulk SRAM taken from [74] is shown in Figure 3.3 (a), and the SV structure configuration of a memory cell in the simulation is shown in Figure 3.3 (b).

Table 3.1 The composition and density of the 65-nm Bulk SRAM device given in [59]

Structure	Sub-layer	Composition	Density (g/cm^3)
Chip	Metal Wire Layer	Cu & SiO_2	5.785
	Insulation Layer	SiO_2	1.5
	Sensitive Layer	Si	2.329
	Substrate Layer	Si	2.329
Board	Board Resin	$C_{15}H_{16}O_2$	1.7
	Board Core	SiO_2	1.5
	Prepreg Layer	$C_{15}H_{16}O_2$	1.8
Package	Package Resin	$C_{22.9}H_{26.1}O_{4.3}$ & $C_9H_{10}O_3$ & SiO_2	1.75

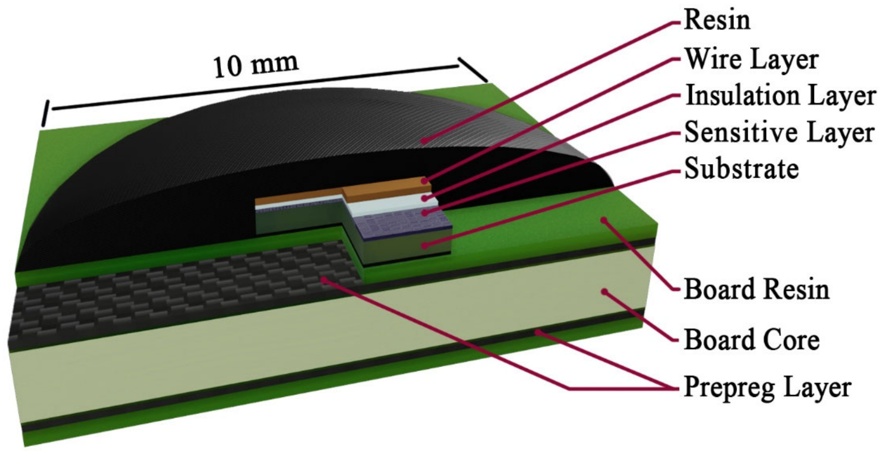

Figure 3.2 Geometric model of the SRAM in simulation.

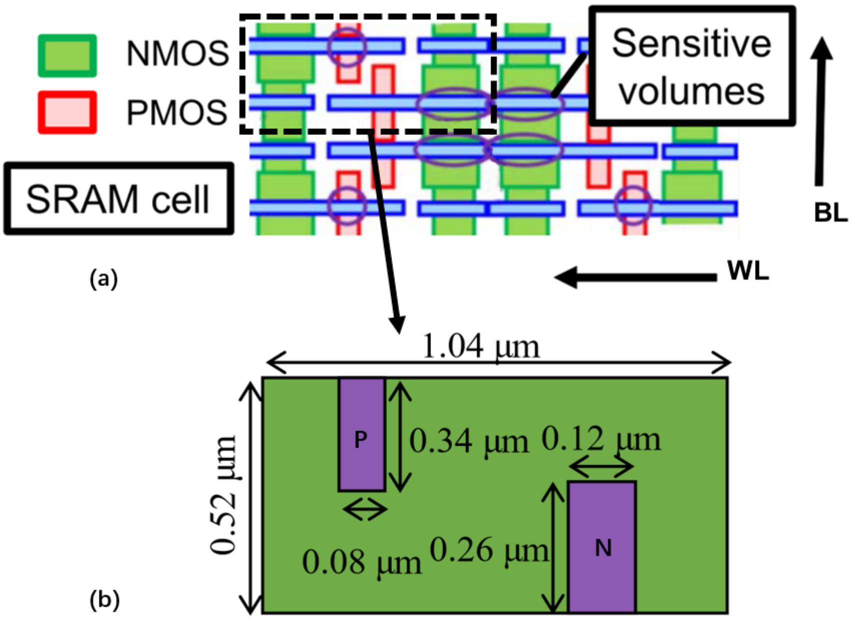

Figure 3.3 (a) Schematic layout of a 2×2 SRAM cell and (b) SV structure configuration of a memory cell in the simulation.

3.2.4 Beam Source and SEU Determination

In Geant4, all beam sources must set their initial kinetic energy instead of momentum. Therefore, the momentum of the muon beam p_μ in the irradiation tests must be converted to the corresponding kinetic energy E_k by:

$$E_k = \sqrt{p_\mu^2 + m_\mu^2} - m_\mu\,, \tag{3-1}$$

where m_μ is the muon rest mass. Also, the relationship is shown in Figure 3.4.

As mentioned in Section 2.2.1, the muon beam in measurements has a Gaussian energy distribution. The standard deviation in energy was reported to average 6.4% and 9.6% for different momentum ranges. In the simulation of this study, the standard deviation of the energy distribution is set to be 7.8% for all the momentum points, which makes the simulation result best reproduce the measurement. Figure 3.5 shows an example of the energy distribution of a 38-MeV/c (6.63-MeV) muon source used in the simulation.

Moreover, since only one SRAM chip is set in the simulation, the beam source size does not have to be the same as the beam profile used in the irradiation tests. However, since the beam source is a 340-mm air distance from the device, the beam flux at the boundary is not uniform due to the multiple scattering. Figure 3.6 illustrates this situation. To avoid this nonuniform, the size of the muon beam source in the simulation is set to be 28 × 28 mm square, which is larger than the device profile.

In a single sensitive volume model, the charge collection efficiency (CCE) is considered 1.0 everywhere within the SV and 0.0 out of the SV. The ionization deposition energy of the muon and secondary particle in the SV is all used to produce charges, which are fully collected. Therefore, an SEU occurs when the muon and secondaries deposit sufficient energy in SV greater than the threshold value E_{th}, obtained from the critical charge Q_c by:

$$E_{th}[\mathrm{MeV}] = \frac{E_{pair} Q_c}{e} = \frac{Q_c[\mathrm{fC}]}{44.5}\,, \tag{3-2}$$

where e represents the elementary charge, and E_{pair} refers to the minimum energy to create an electron-hole pair in silicon and is equal to 3.6 eV.

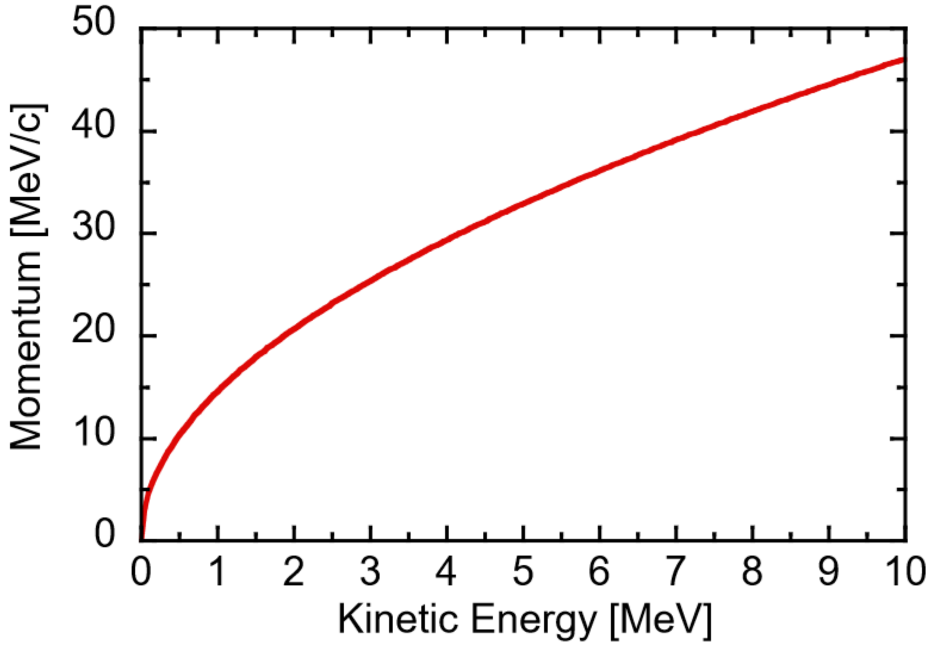

Figure 3.4 Relationship of muon momentum p_μ and kinetic energy E_k, derived by the equation (3-1).

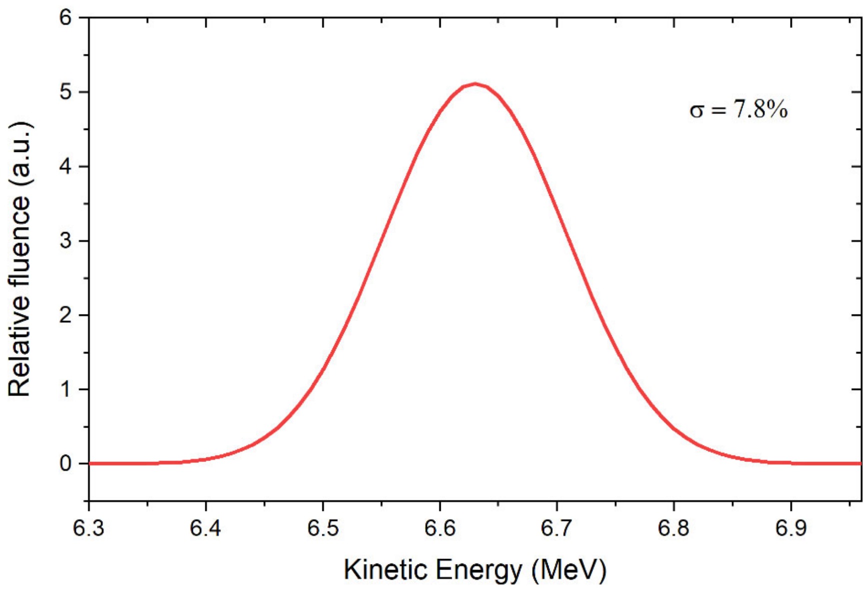

Figure 3.5 Estimated kinetic energy distribution of a muon beam in 38-MeV/c irradiation (6.63 MeV in kinetic energy). The standard deviation is 7.8%.

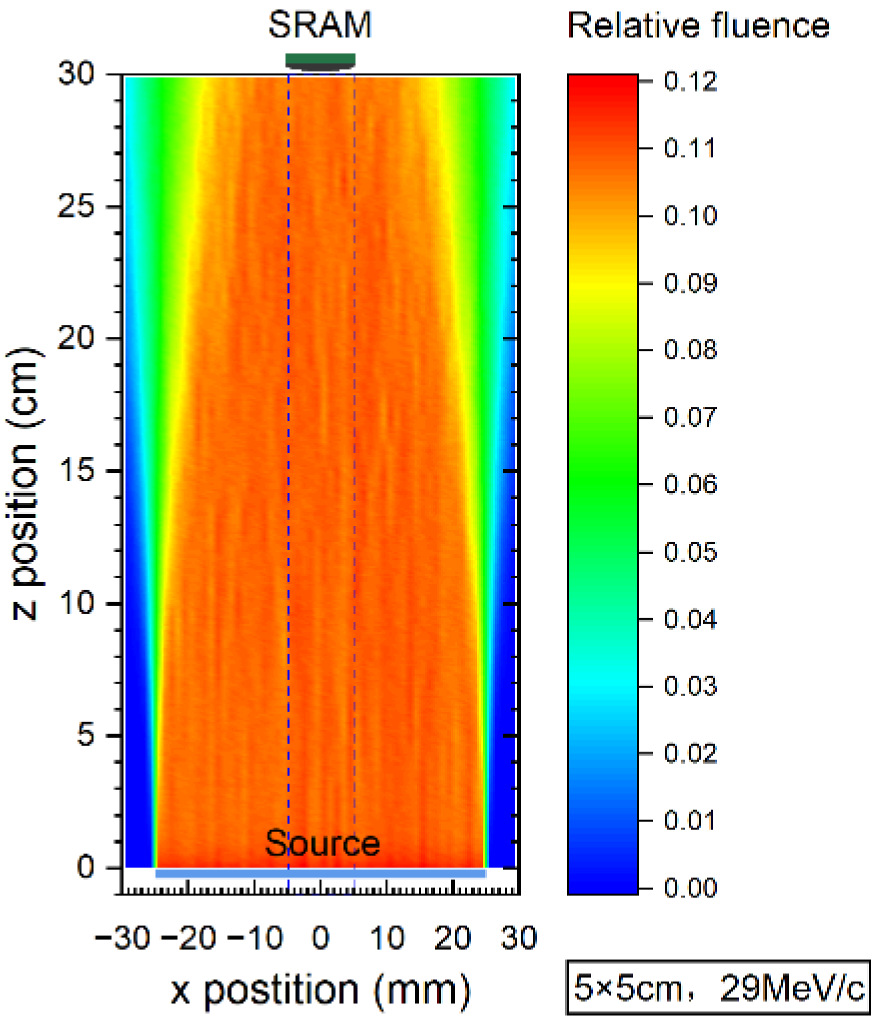

Figure 3.6 Fluence distribution of 29-MeV/c muons in case of 5×5 cm square source.

3.3 Simulation Results

3.3.1 Critical Charge Dependence

As mentioned, SEUs are generated if the deposition energy producing the charges exceeds the critical charge value (Q_c). The actual Q_c of a device is related to the structure, materials, and manufacturing processes of the transistor. It is challenging to obtain precise values when the device manufacturer does not provide the parameter. In Monte Carlo simulations, Q_c is usually estimated by comparing the simulated SEU cross-section with experimental values. The estimation is considered reliable when the estimated Q_c values closely match for different types of particles and irradiation conditions. In other word, Q_c becomes a vital adjustable parameter directly affecting the simulation results. Thus, The Q_c-dependence of the negative and positive muon-induced SEU cross-section is studied to adjust the value to the reasonable value. Figure 3.7 shows the critical charge dependent SEU cross sections induced by 38-MeV/c negative muon direct ionization and secondary ions from muon capture in case of BS irradiation. Figure 3.8 shows the critical charge dependent SEU cross sections generated by 38-MeV/c positive muon direct ionization in the case of BS irradiation. By comparing the measured values of the SEU cross-section caused by 38-MeV/c positive and negative muons, the critical charge of 1.1 fC makes the simulation results agree with the measured values best.

From Figure 3.7, the secondary particles Helium (He) and the residual nucleus Magnesium (Mg) and Aluminum (Al) released from muon capture are the primary causes of the negative muon SEU. The Hydrogens (H) come in the second contribution of SEU, followed by direct ionization of negative muon. Their specific contributions are shown in Figure 3.9 when Qc is set to 1.1 fC.

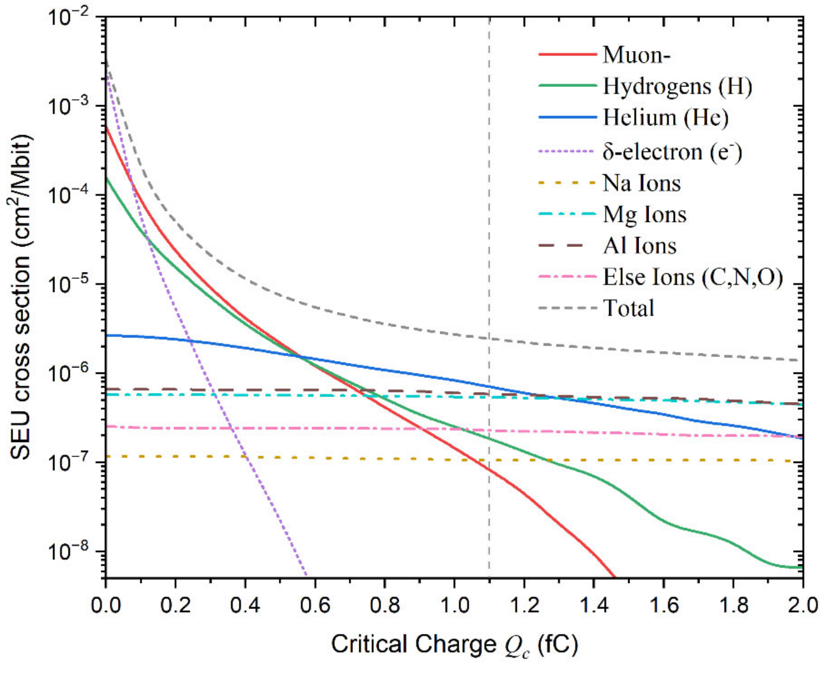

Figure 3.7 Critical charge-dependent SEU cross sections induced by 38-MeV/c negative muons direct ionization and secondary ions from muon capture, in the case of BS irradiation.

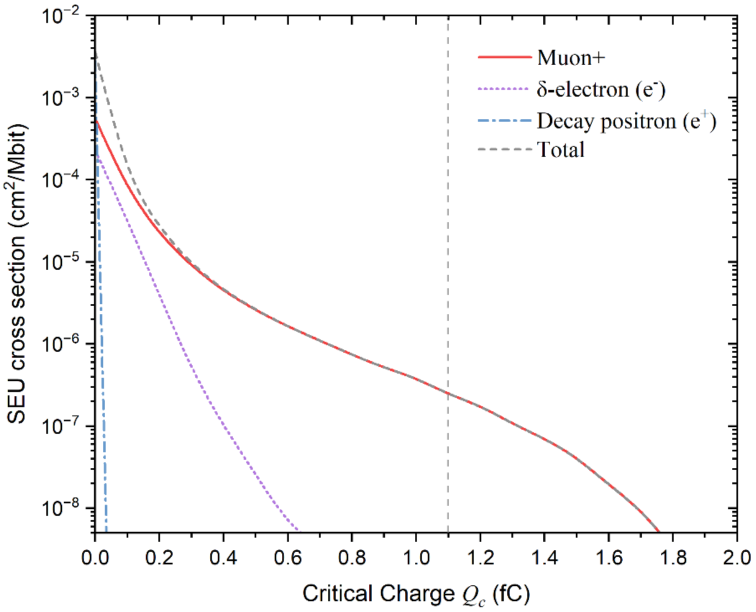

Figure 3.8 Critical charge-dependent SEU cross sections induced by 38-MeV/c positive muons direct ionization in the case of BS irradiation.

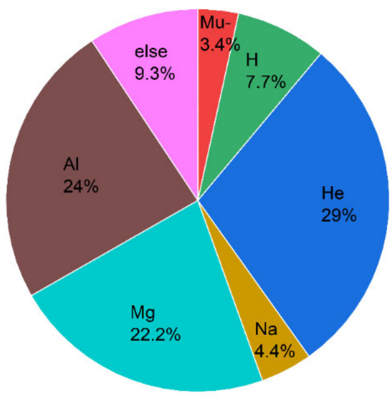

Figure 3.9 Contribution of direct ionization and secondaries from muon capture to the SEU in the case of 38-MeV/c negative muon BS irradiation. The critical charge was set to 1.1 fC.

Also, from the comparison of Figures 3.7 and 3.8, the direct ionization of negative muons results in an SEU cross-section of 8.30×10^{-8} cm^2/Mbit, which is significantly lower than the one resulted from positive muons, i.e., 2.45×10^{-7} cm^2/Mbit. This is due to the Barkas effect described in the previous Section 1.3.1.

3.3.2 Muon Momentum Dependence

The simulation results of momentum-dependent SEU cross sections induced by positive and negative muon for both PS and BS irradiation tests are given and compared with the measured one in Figure 3.10. Panel (a) shows the measured and simulated positive and negative muon SEU cross-sections of 65-nm bulk SRAM for the PS irradiation test, while panel (b) shows those for the BS irradiation test. The measured results are shown with the colored points, while the simulated results are with the colored dash curves. The critical charge Q_c was determined to be 1.1 fC in simulations so that the simulated SEU cross-sections reproduce the experiment well in both PS and BS irradiation tests.

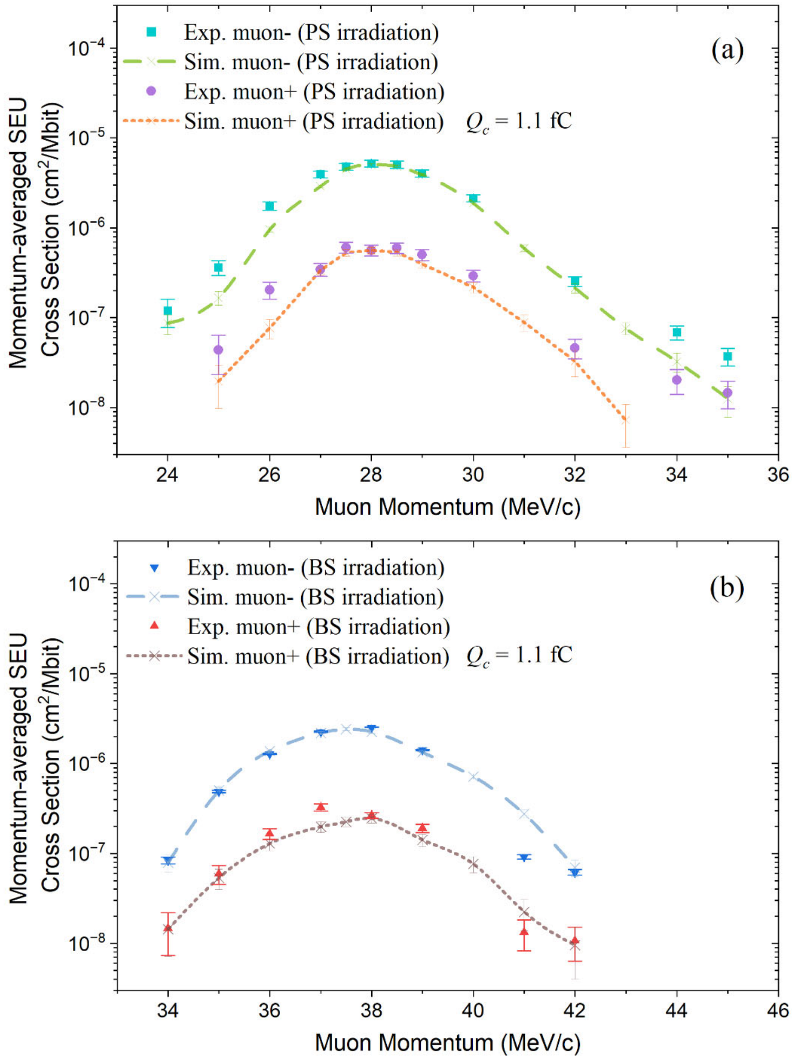

Figure 3.10. The simulation results of momentum-dependent SEU cross sections induced by positive and negative muon for both PS and BS irradiation tests.

From Figure 3.10, the simulated peak positions and cross-sections under the BS irradiation agree well with the experimental results for both positive and negative muons. As for the PS irradiation, the simulated results of the peak position and the cross sections near the peak region agree with the experimental results. However, the simulated cross-sections are smaller than the experimental ones in the non-peak area, especially in the high-momentum region. No SEU was observed in the simulation for the 34-MeV/c and 35-MeV/c positive muons. This may be because the momentum distribution of incident muons is not strictly Gaussian and has tails in the low and high momentum regions. In addition, the standard deviation of the muon energy spectrum may vary with momentum.

In addition, in agreement with the experimental results, the simulated SEU peaks for PS irradiation are also more than two times larger than those for BS irradiation. In subsection 3.4, a simulation-based analysis of the difference in the peak SEU cross-sections between PS and BS irradiations will be made.

3.4 Quantitative Assessment of the Impact of Energy Straggling on SEU

The difference in peak positions of the SEU cross-section between the PS and BS irradiations can be easily explained by the difference in penetration depths before muons reach the SV. The SEU cross-section is maximized at the momentum where the Bragg peak is located in the SV. Also, the difference in the magnitude of the SEU cross-section peak can be explained qualitatively by the difference in energy loss straggling due to different thicknesses. The effect of energy straggling can be seen in the variation of the Bragg peak height with muon energy and depth of incidence in Figure 1.12. However, since SEU triggers when the deposition energy exceeds the threshold E_{th}, the Bragg curves, like in Figure 1.12, cannot quantitatively characterize the impact of energy straggling on the SEU cross-section. Therefore, this study performs a quantitative assessment by defining the concept of effective SEU fluence.

3.4.1 Assessment Method of the Effective SEU Fluence

As mentioned in Section 3.2.4, the deposition energy in the SV to cause SEUs has a threshold value (E_{th}), and the deposition energy of positive muons depends on their kinetic energy before entering the SV. Due to stochastic processes such as energy straggling and multiple scattering in device materials, the kinetic energy of positive muons just before the SV has a distribution even for mono-energetic muons. Using simulation, the energy spectrum of positive muons was calculated just before the SV for 28-MeV/c PS irradiation and 38-MeV/c BS irradiation. The results are shown with the black curves in the upper and lower panels in Figure 3.12. The red curves in Figure

3.12 indicate the energy spectrum of positive muons with energy deposition over E_{th} in a virtual SV, and the integrated values of the red curves are defined as "effective SEU fluence" for the positive muons. This means the relative fluence of muons that effectively induce SEUs.

Here, a virtual SV with a horizontal area equal to the average of two actual SVs is set up as a cylinder centered at the position of each muon+ incident in SV, as shown in Figure 3.11. The reason for using such a virtual SV setup is the proportion of the actual SV to the area of the memory cell is relatively small, as shown in panel (a) of Figure 3.3, resulting in a low incident effectiveness rate. If a more realistic SV setup as in Figure 3.3 is used, the number of SEU induced by positive muons in simulation is not sufficient to form a continuous and statistically significant spectrum of energy. Therefore, the red line in Figure 3.12 is a simplified way of calculating the energy spectrum of SEU events.

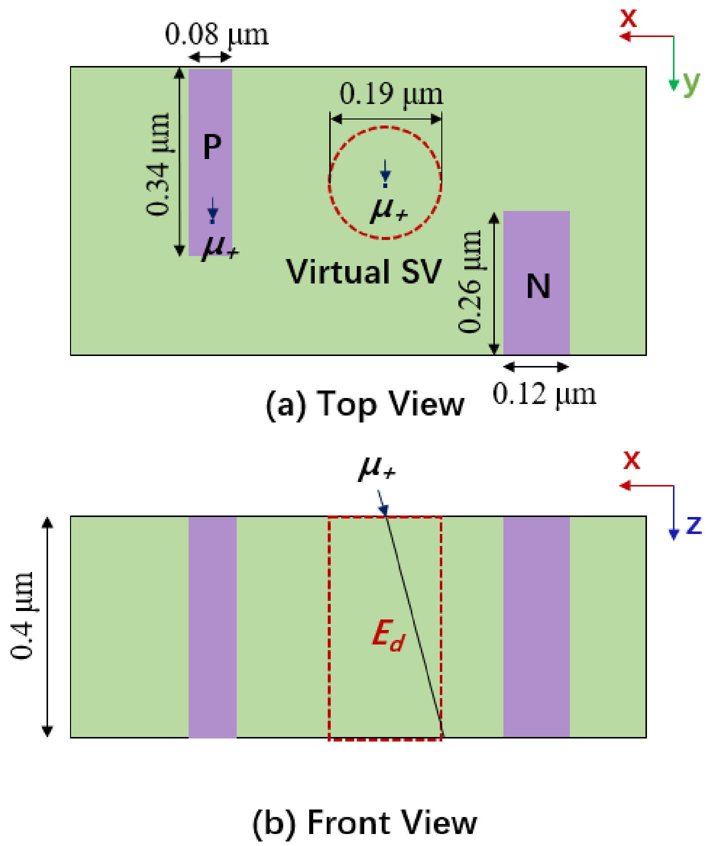

Figure 3.11 Schematic of the virtual SV setup used for calculating the effective SEU fluence.

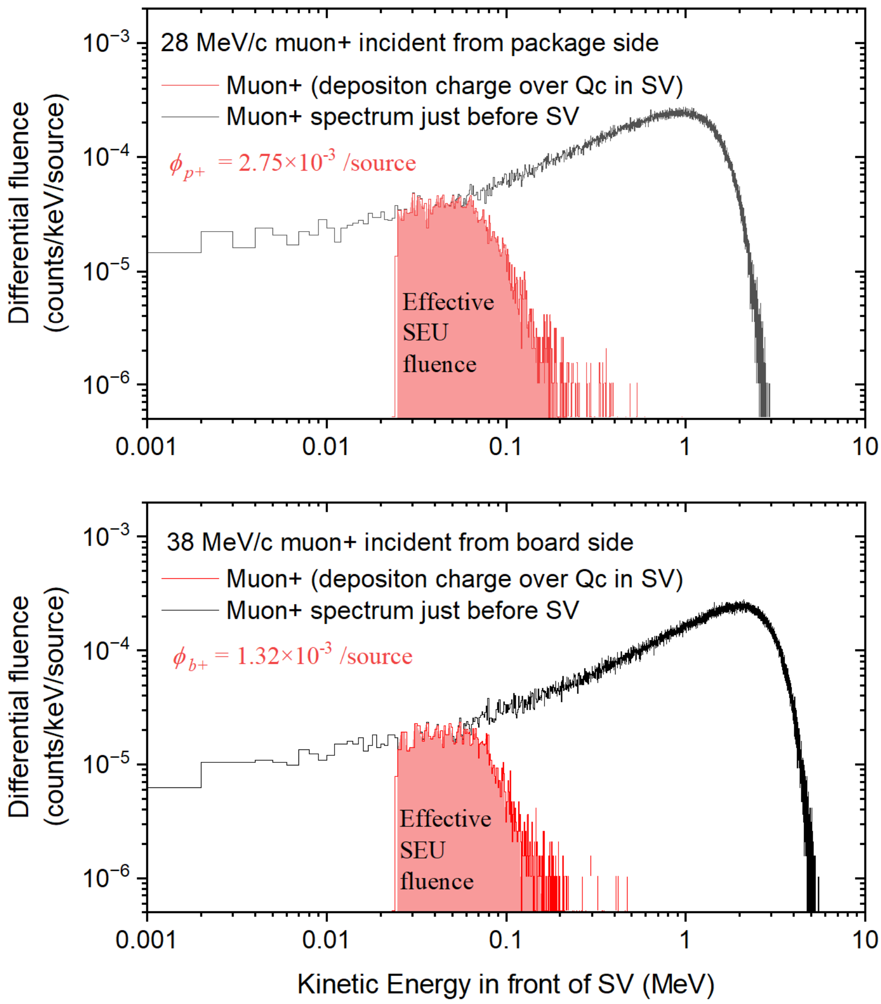

Figure 3.12 Energy distributions of positive muons before entering the SV with different irradiation sides are shown with black curves. The lower panel shows the BS irradiation case, while the upper panel shows the PS irradiation case. The red curves mean the positive muons with deposition energy over E_{th} in SV.

The effective SEU fluences for PS irradiation with 28-MeV/c positive muons and BS irradiation with 38-MeV/c positive muons are given by ϕ_{p+} and ϕ_{b+}, respectively. They differ from each other because the muon energy distinctions before the SV are different between PS and BS irradiations due to the change in the incident depth. Their ratio k_{EF+} is obtained by

$$k_{\mathrm{EF}+} = \frac{\phi_{p+}}{\phi_{b+}} = 2.08 \pm 0.03\,, \tag{3-3}$$

where the error is estimated from the statistical error of the simulated effective SEU fluence. This ratio $k_{\mathrm{EF}+}$ could quantitatively estimate the impact of different energy straggling degrees on the peak SEU cross-sections of positive muons between PS and BS irradiation.

For negative muons, the main contribution of the SEUs is the secondaries released by the muon capture reaction. Therefore, the spatial distribution of the negative muon capture events inside the device is counted by simulation and shown with the black curves in Figure 3.13. The vertical axis is the differential events number per incidence length, and the horizontal axis is the position of the events described by the distance from the bottom of the package. The device structure in the place of an event is marked on the top of the figure. The upper panel shows the case of PS irradiation with 28-MeV/c negative muons, and the lower panel shows the case of BS irradiation with 38-MeV/c negative muons. Note that the peak of muon capture events appears in the metal layer, and the difference between muon capture events in the package and those in the SRAM chip is due to different materials.

Once the secondary ions released from the muon capture reaction deposit the energy over E_{th} in the SV, the events are counted at their released (initial) position, shown with curves of different colors for different secondary ions in Figure 3.13. The green curves represent the hydrogens (H), including protons, deuterons, and tritons. The blue curves represent the alpha particles (He), and the purple ones represent the heavy ions (HI), like aluminum, magnesium, and sodium. Contributions from HI are distributed closest to the SV, followed by alpha, and those from hydrogens are distributed furthest. Their different ranges in the device material can explain this trend.

Then, the events of all the secondary ions, whose deposition energies in the SV exceed E_{th}, are added and defined as the effective SEU fluence of negative muons. The effective SEU fluences for PS irradiation with negative muons of 28 MeV/c and BS irradiation with negative muons of 38 MeV/c are denoted by ϕ_{p-} and ϕ_{b-}, respectively. Their ratio $k_{\mathrm{EF}-}$ is defined and calculated by

$$k_{\mathrm{EF}-} = \frac{\phi_{p-}}{\phi_{b-}} = 1.96 \pm 0.04\,. \tag{3-4}$$

Similarly, this ratio $k_{\mathrm{EF}-}$ gives a quantitative estimation of the impact of different energy straggling degrees on the peak SEU cross-sections of negative muons between PS and BS irradiation.

The defined effective SEU fluences for positive and negative muons directly characterize the capability of particles to induce SEU in the case of different incident depths of the SV.

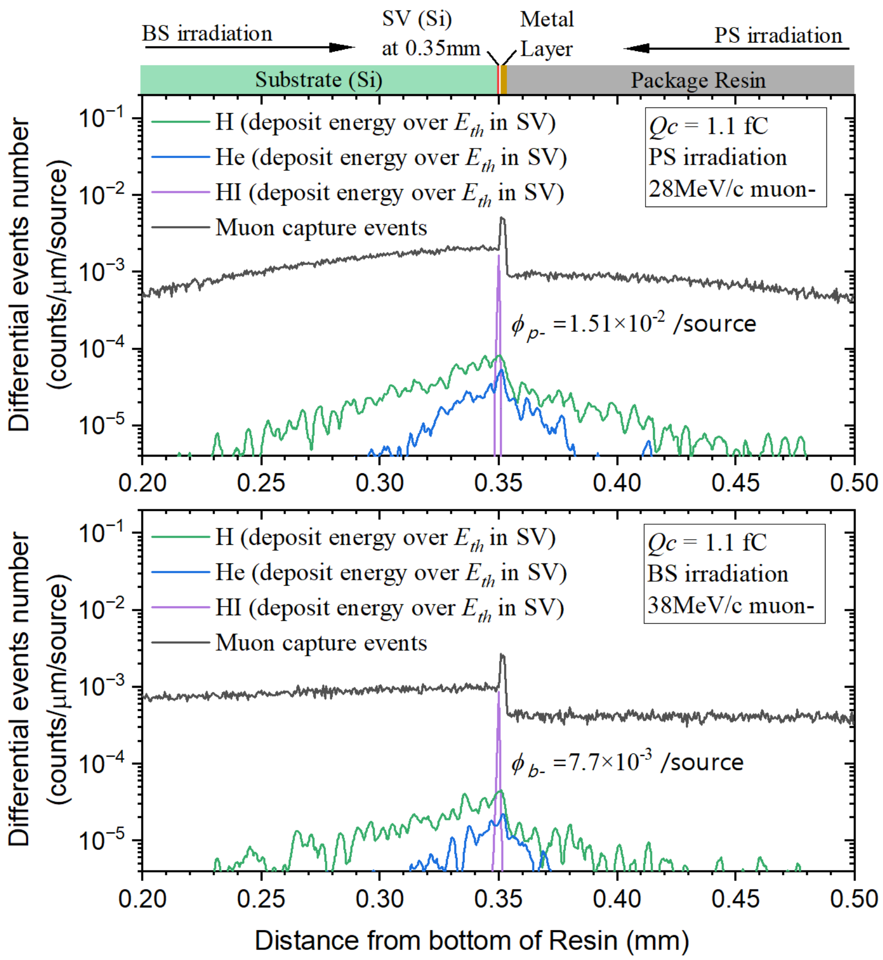

Figure 3.13. Spatial distributions of muon capture events inside the 65-nm bulk SRAM for PS irradiation with 28-MeV/c negative muons and BS irradiation with 38-MeV/c negative muons. The events of their released secondaries depositing energy over E_{th} in SV are also shown with colored curves.

3.4.2 Assessment Validity with Experimental Results

To verify that the effective SEU fluence defined for positive and negative muons can characterize the different capabilities of particles to induce SEU due to the energy straggling, this study compares the effective SEU fluence ratios of positive and negative muons (k_{EF+} and k_{EF-}) in PS and BS irradiation with the measured SEU cross-sections ratios (k_{CS+} and k_{CS-}) in Figure 3.14.

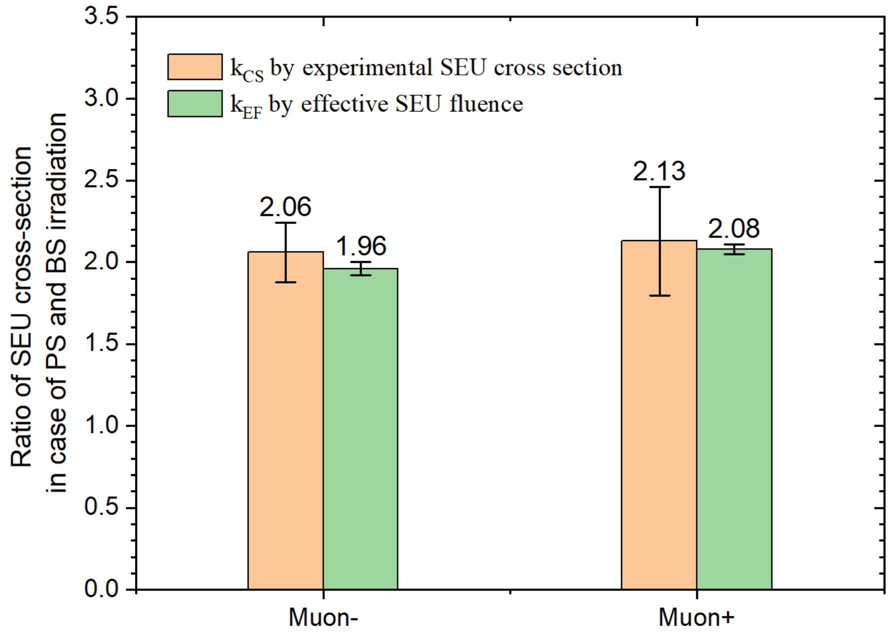

Figure 3.14 Comparison of the experimental and estimated ratios of peak cross sections for PS irradiation to those for BS irradiation for both positive and negative muons.

As shown in Figure 3.14, the k_{CS+} value in equation (2-13) and the k_{EF+} value in equation (3-3) agree within their error margin. And despite the minor differences within the error margin, k_{EF-} and k_{CS-} also agree well. Thus, the effective SEU fluence is essential to understand that the magnitude of the peak SEU cross-sections is different by a factor of about two between the PS and BS irradiations with both positive and negative muons.

3.4.3 Other Application of the Effective SEU Fluence

As mentioned in Section 3.4.2, the effective SEU fluence can quantitatively characterize the influence of depth of SV on the SEU cross sections due to the energy straggling. Therefore, it also can be used to evaluate the impact of package shape on the SEU spatial distribution.

For instance, the package of 65-nm bulk SRAM is ellipsoidal; the muons at the edge and center of the package will pass through different thicknesses to reach the SV and influence the SEUs. However, this phenomenon is insignificant because the experimental beams have a momentum distribution. Therefore, simulations with mono-energetic muon beams are performed to reveal the impact of shape on the spatial distribution of the SEUs. Meanwhile, the effective SEU fluence of positive muon for the corresponding irradiation cases is counted and used to explain the simulation results quantitatively. The results are shown in Figure 3.15. Figure 3.15 (a) shows the two-dimensional spatial distribution of the effective SEU fluence (left panel) and their SEU event in simulation (right panel) in PS irradiation with 28-MeV/c positive muons, while (b) shows the case in PS irradiation with 28.5-MeV/c positive muons. The horizontal and vertical coordinates in Figure 3.15 are the positional coordinates on the 2.8 by 2.4 mm chip, respectively. Figures 3.15 (a) and (b) show that the two-dimensional spatial distribution of effective SEU fluence muon+ agrees well with SEU locations.

The muons incident from the edges of the package pass thinner material to arrive at SV, thus first making their Bragg peak overlap the SV in 28 MeV/c. Therefore, the effective SEU fluence and simulated SEU location are distributed at the ring edge. As for the muons incident from the center of the package, they pass thicker material to arrive at SV, thus overlapping their Bragg peak in SV in 28.5 MeV/c. Their effective SEU fluence and simulated SEU location are distributed at the center circle. In addition, to further verify that this SEU location distribution is due to the package shape, this study also sets up a rectangular package for comparison. The result is shown in Figure 3.15 (c). Due to the use of a rectangular package, the depth of incidence for the muon beam to arrive at the SV is the same in the two-dimensional chip plane. Thus, the effective SEU fluence and SEU location are almost uniformly distributed and do not show a tendency to concentrate anywhere in the two-dimensional chip plane. Noise-like scattering in the effective SEU fluence and SEU Event distribution is due to stochastic processes such as multiple scattering and energy loss straggling.

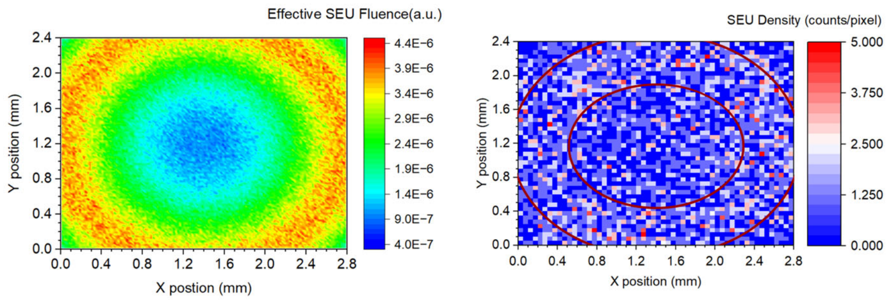

(a) 28-MeV/c muon+, ellipsoidal package

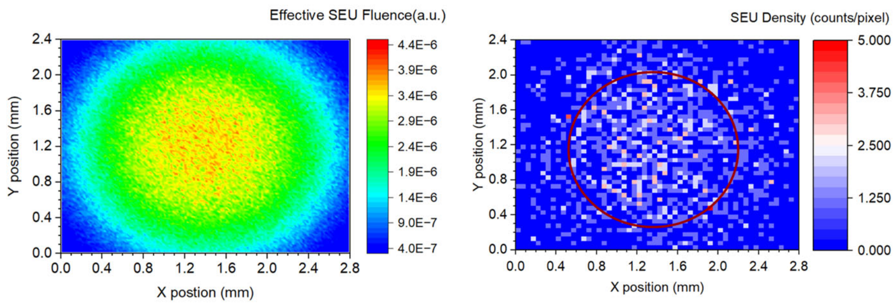

(b) 28.5-MeV/c muon+ , ellipsoidal package

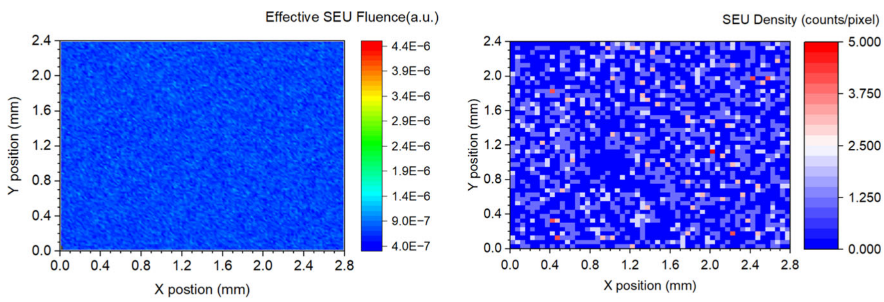

(c) 28-MeV/c muon+, rectangular package

Figure 3.15. The two-dimensional spatial distribution of the effective SEU fluence (left panel) and their simulated SEU event location (right panel) in PS irradiation with 28-MeV/c (a) and 28.5-MeV/c (b) positive muons. Panel (c) shows the result when changing the package shape from ellipsoidal to rectangular.

3.5 Influence of multiple scattering

The difference in SEU cross-sections between PS and BS irradiations has been explained by the effective SEU fluence in Section 3.4. However, in addition to the energy dispersion affecting the effective SEU fluence, multiple scattering also affects the muon incident angle just before the SV, which may also influence the SEU cross-section. Thus, it was evaluated whether the multiple scattering on the SEU difference between PS and BS irradiation, i.e., the ratio $k_{CS\pm}$, is significant or not by simulation.

In the simulation, multiple scattering is canceled, while the other conditions are the same as in section 3.2. The results of positive muons without multiple scattering are compared with those with multiple scattering in Figure 3.16. The relative SEU event numbers, the relative muon fluences incident to the device, and the SEU cross-sections of positive muons in PS and BS irradiation with and without multiple scattering are shown with different color columns.

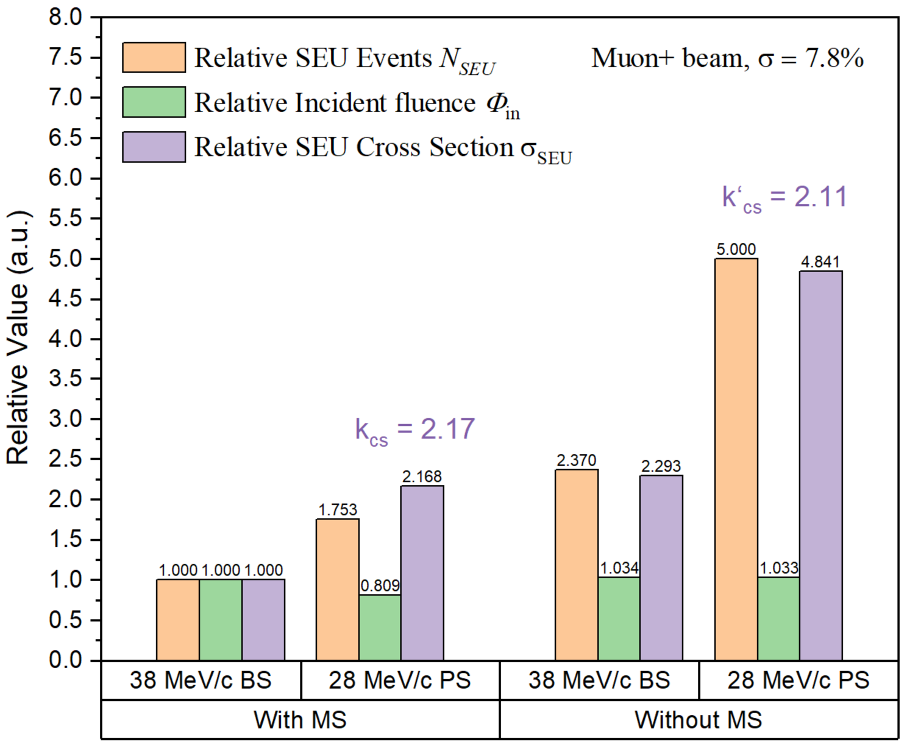

Figure 3.16 Evaluation of the effects of multiple scattering on SEU cross-sections of positive muon in PS and BS irradiations

By observing the relative SEU events (orange) and SEU cross-sections (purple) in Figure 3.16, we can see that they significantly increase in the case without multiple scattering. This suggests that multiple scattering of muon+ in air and device materials affects the SEU events and SEU cross-sections. The reasons for this phenomenon are as follows. The multiple scattering process significantly changes the angular distribution of positive muons after they penetrate air and device material to the surface of the SV. The angular distribution of positive muons on the SV surface with and without multiple scattering are shown in Figure 3.17. The result without multiple scattering (MS) is shown as the black curve, while the result with multiple scattering is shown as the red curve. As can be seen from the Figure 3.17, when multiple scattering is neglected, the particles are almost entirely incident on the SV with θ equals to 0 degree. Whereas, with multiple scattering, there is a broader distribution of the incidence angles of the particles and peaks at about 8.5 degrees. The z-direction dimension of the SV is significantly larger than the x-direction for both NMOS and PMOS, as shown in Figure 3.18. Therefore, when multiple scattering is neglected, the positive muons that would have an angular distribution of incidence are almost entirely incident along the longest z-axis direction of the SV, and the level of energy deposition is higher than in the (actual) case with multiple scattering.

This conclusion reminds us that simulation without multiple scattering or placing muon sources with equivalent energy spectra on the surface of the SRAM geometric model can increase the number of SEU events. This results in an overestimation of the value of critical charge Q_c when comparing the simulation result with the experimental cross-sections. In Figure 3.19, we compare the observed values of Q_c with and without multiple scattering when the simulation cross-section reproduces the measured one. When multiple scattering is neglected, the Q_c dependent SEU cross-section is clearly different from that with multiple scattering. In the Q_c range of 0.2 to 1.75 fC in Figure 3.19, the simulated cross-sections without multiple scattering are more significant than those with multiple scattering. This indicates that the level of energy deposition is higher in the case of no multiple scattering.

However, the figure also shows that this increase in the SEU cross-sections due to canceling the multiple scattering is nearly identical in the PS and BS irradiations. Thus, the k_{CS} value is almost the same between the cases with and without multiple scattering. This phenomenon is due to two main reasons. On the one hand, the transporting distance of muon+ between the beam exit and the device is the same for PS and BS irradiations. On the other hand, the difference in material thickness and density between PS and BS irradiations is not enough to significantly change the effect of multiple scattering on the energy deposition process.

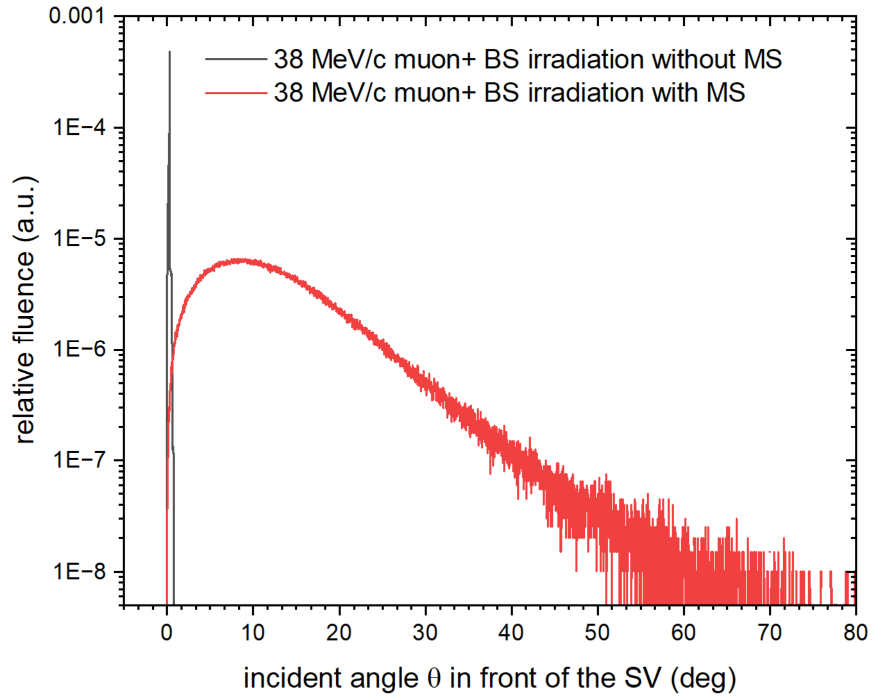

Figure 3.17 Distribution of momentum zenith angle θ for positive muons at the surface of the SV (where incident SV).

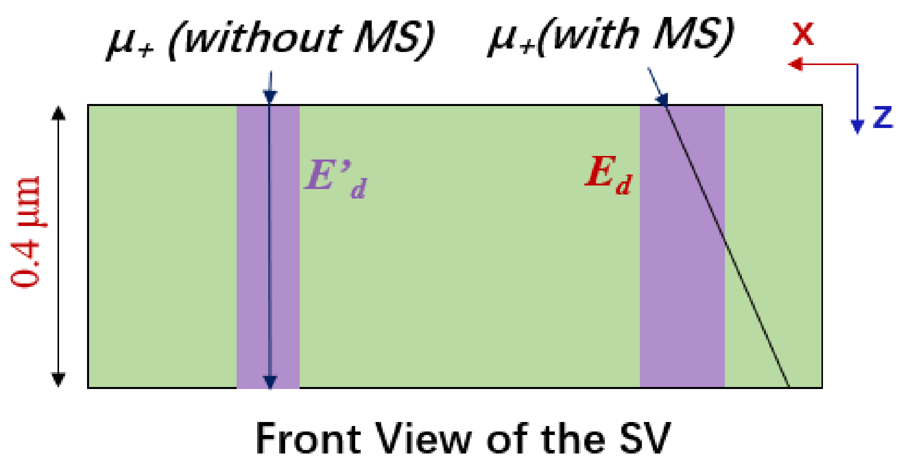

Figure 3.18 Illustration of differences in energy deposition levels with and without multiple scattering.

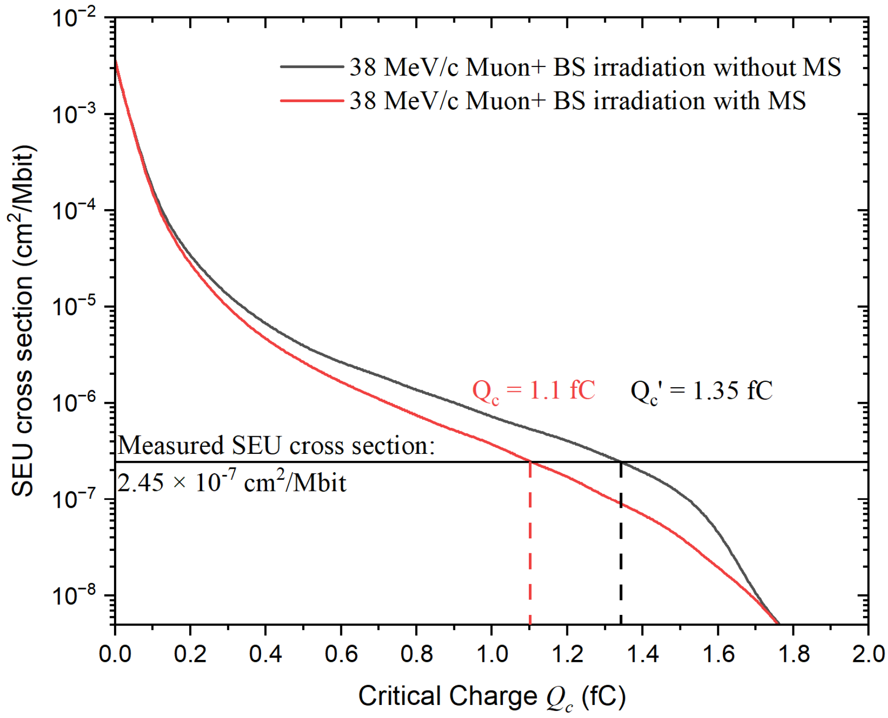

Figure 3.19 Critical charge-dependent SEU cross-sections induced by 38-MeV/c positive muons in the case of BS irradiation with and without multiple scattering.

As for negative muons, the results without multiple scattering are compared with those with multiple scattering in Figure 3.20. Similar to positive muons, the k_{CS} value of negative muons is almost the same between the cases with and without multiple scattering. However, unlike the positive muons, the effect of multiple scattering on the SEU cross-sections of negative muons is insignificant. They were almost the same between the cases with and without multiple scattering. This is because the negative muons SEUs are mainly induced by the secondary particles released from the muon capture reaction. Therefore, the change in the incident angle distribution of negative muon on the SV surface due to canceling multiple scattering does not significantly affect the SEUs.

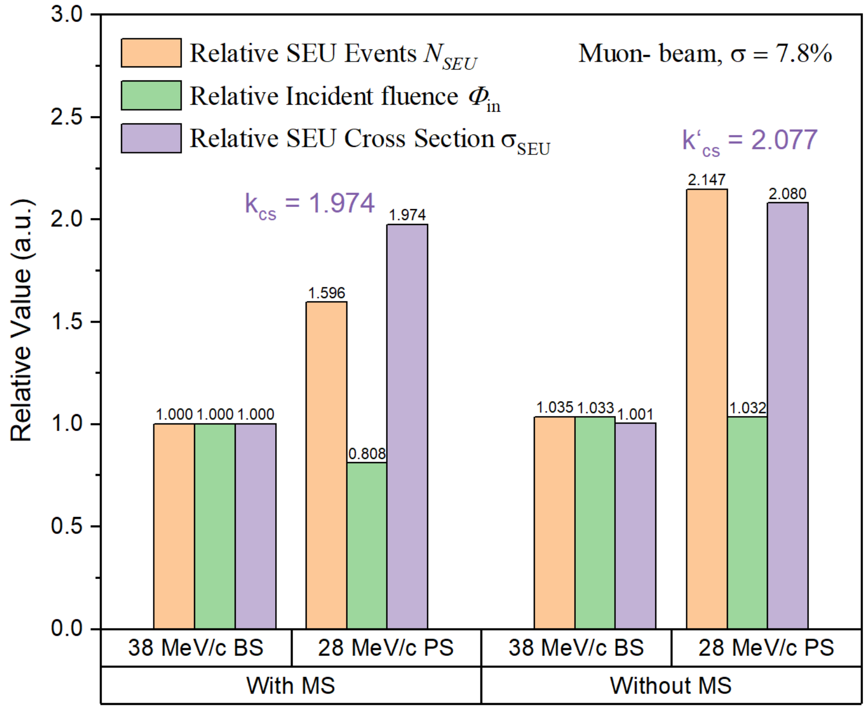

Figure 3.20 Evaluation of the effects of multiple scattering on SEU cross-sections of negative muon in PS and BS irradiation

3.6 Conclusion

The Q_c dependent SEU cross-section was first analyzed after introducing the physical process and geometric model of simulation. After comparing the experimental results, the Q_c was determined to be 1.1 fC. For 38-MeV/c negative muons, the secondary particles Helium (He) and the residual nucleus Magnesium (Mg) and Aluminum (Al) released from muon capture are the primary causes of the SEUs. The Hydrogens (H) come in the second contribution of SEU, followed by direct ionization of negative muon.

The simulated SEU peak positions and cross-sections under the BS irradiation agreed well with the experimental results for both positive and negative muons. As for the PS irradiation, the simulated results of the peak position and the cross sections near the peak region agreed with the experimental results. The simulated cross-sections are smaller than the experimental ones in the non-peak area, especially in the high-momentum region. The simulated SEU peaks for PS irradiation are also about two times larger than those for BS irradiation, which agrees well with the measurements.

Then, the effective SEU fluence was defined and used to quantitatively explain the ratio of SEU cross-sections that exist between PS and BS irradiation. The SEU ratios conducted by effective SEU fluence were 2.08 for positive muons and 1.96 for negative muons, which agreed well with that undertaken by measured SEU cross sections.

Finally, the analysis confirmed that the effect of multiple scattering on the ratio of SEU cross-section between PS and BS irradiation is insignificant.

4 Comparison of Positive Muon with Proton-induced SEU

4.1 Introduction

As our concern for muon SEUs is growing, many more experiments need to be performed. However, there are minimal muon irradiation facilities worldwide. Figure 4.1 shows worldwide muon irradiation facilities in operation and under construction as of 2022. The related information was collected from the website of the International Society for µSR Spectroscopy (ISMS) [75]. As of 2022, only five muon facilities are in operation, and the other two are under design and construction.

The minimal muon test facilities worldwide make it challenging to conduct muon irradiation tests. As the Low Energy Proton (LEP) induced SEU and its contribution to the SER have been investigated widely and have similarities with positive muons in physical properties, this chapter established a method for predicting muon SEUs using a combination of proton testing and Monte Carlo simulation, after comparing positive muon and proton-induced SEU in a 65-nm bulk SRAM.

Since no proton test on the same SRAM device in muon tests was conducted, the proton SEU cross-section data used for comparing with positive muon and for developing the method were obtained by simulation. Before making the simulation, the validity of the physical model is verified with the experimental results of other 65-nm SRAM devices.

Facility Name	Organization	Source Type	Current Status
CMMS	TRIUMF	Continuous	In operation
RIKEN-RAL	ISS	Pulsed	In operation
LMU/SµS	PSI	Continuous	In operation
MUSE	J-PARC	Pulsed	In operation
MuSIC	RCNP	DC	In operation
RAON	ICT/NRF	DC	under construction
MELODY	CSNS	Pulsed	under construction

Figure 4.1 The muon irradiation facilities in operation and under construction as of 2022. The information is collected from [75].

4.2 Simulation Method of Proton

4.2.1 Physical Process

In the Geant4 simulation of proton-induced SEUs, direct ionization, multiple scattering, and nuclear reactions were considered as the physical processes during transportation and energy deposition.

The same as muons mentioned in Section 3.2.2, the built-in physical process list EM Opt4 (Electromagnetism Option 4) is in charge of simulating the electromagnetism processes of protons, including ionization, multiple scattering, bremsstrahlung, etc. The multiple Coulomb scattering is handled by the WentzelVI model and a single scattering model, the same as the model of muons. However, the physical models and database settings for proton ionization are not all the same as muons. The Bragg model is used below 2 MeV, and the Bethe-Bloch model above is used for proton ionization.

In addition, the proton inelastic hadron-nucleus processes (i.e., proton-induced nuclear reactions) are implemented by the Bertini intranuclear cascade model [72] between 0 and 6 GeV. The Fritiof (FTF) model [76] handles the nuclear reactions from 3 GeV to 100 TeV. Where the Bertini and FTF models overlap in the proton energy range, the Bertini model is invoked with a probability that decreases linearly from 1.0 to 0.0, and the FTF model is invoked with the complementary possibility.

4.2.2 Validity of the Simulation

Since no proton test on the same 65-nm SRAM devices as used in muon irradiation tests was conducted, the validity of the proton simulation was performed by a proton SEU simulation for another RADSAGA 65-nm SRAM [77]. The simulation result of proton SEU cross-sections is compared with the experimental data in Figure 4.2. The geometric and material information for modeling the device and the experimental proton data were taken from [77]. The critical charge (Q_c) was determined to be 0.45 fC to make the simulation best agree with the measured one.

The simulated proton SEU cross-sections show reasonably good agreement with the experimental ones at proton energies below 10 MeV, where direct ionization dominates the energy deposition process. Meanwhile, the simulation result differs from the experimental data at proton energies above 10 MeV, where indirect ionization, i.e., ionization by secondary ions generated by nuclear reaction, dominates. This disagreement indicates that nuclear reaction models used in the simulation may not accurately describe nuclear reactions. Also, impurity components in the device material might affect the reaction cross sections. However, the model choice is beyond the scope of the current work focusing on positive muon and proton SEUs.

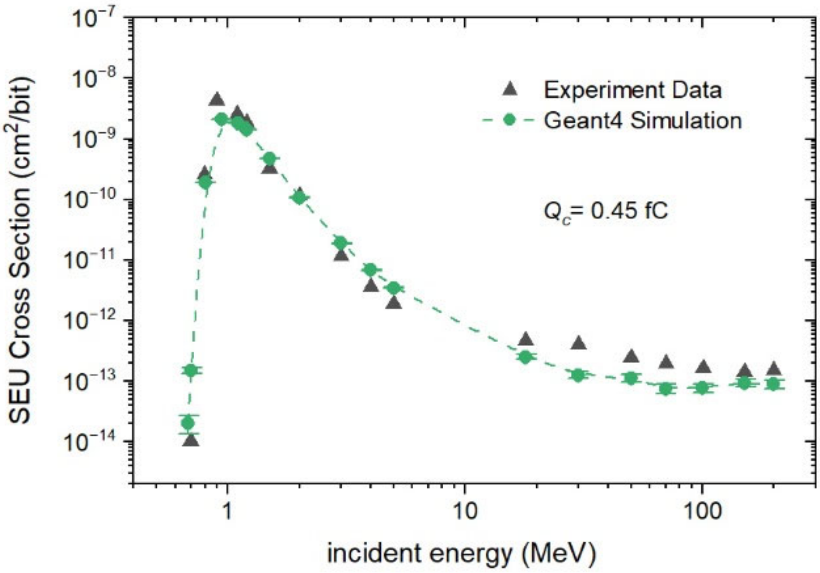

Figure 4.2 Comparison of simulated proton SEU cross sections with measured ones [77] for RADSAGA 65-nm SRAMs.

4.2.3 Other Setup in Simulation

The same geometrical model as in the muon simulation in Chapter 3 was used to simulate the proton-induced SEUs for the 65-nm SRAMs used in muon irradiation tests. The critical charge is also the same 1.1 fC as in the muon irradiation simulation. The proton source is set to the same area and the same distance of 340 mm with the muon simulation.

However, to establish a better mapping of the proton to muon SEU cross-section, after repeated tests, the energy spectrum width of the proton should be slightly larger than that of the muon and is therefore set to 8.8%. This will be detailed in Section 4.4.2

4.3 Simulation Results

4.3.1 Kinetic Energy Dependence of SEU Cross-Sections

Figure 4.3 compares kinetic energy-dependent SEU cross-sections in BS irradiation between positive muon and proton. The red curve shows the simulation result of positive muon irradiation on 65-nm bulk SRAM, while the green one shows the proton case. By comparison, one can find that the peak energy of the proton-induced SEU is much higher than that of the positive muon. The peak SEU of the positive muon is at 6.63 MeV, while that of the proton is at 17.1 MeV. This is because protons have a lower penetrating ability than muons and thus require more initial kinetic energy to pass through the same thickness to reach the SV, as shown in Figure 1.12, with the varying initial (incident) kinetic energy between protons and positive muons with the same range.

The magnitude of proton-induced SEU cross-sections is also more significant than the muon-induced one. This can be explained qualitatively by the different Bragg curve properties between the proton and positive muon with the same range, as shown in Figure 1.12. The ratio of the peak SEU cross-section between proton and positive muon by using simulation is derived by

$$k_{\mathrm{CSp}} = \frac{\sigma_p}{\sigma_m} = 15.28 \pm 1.87, \tag{4-1}$$

where σ_p and σ_m denote the peak SEU cross-section for proton and positive muon, respectively. The error is derived using the error propagation formula considering the statistical error of SEU events number in simulations. This ratio will be explained quantitatively using the effective SEU fluence in Section 4.3.2.

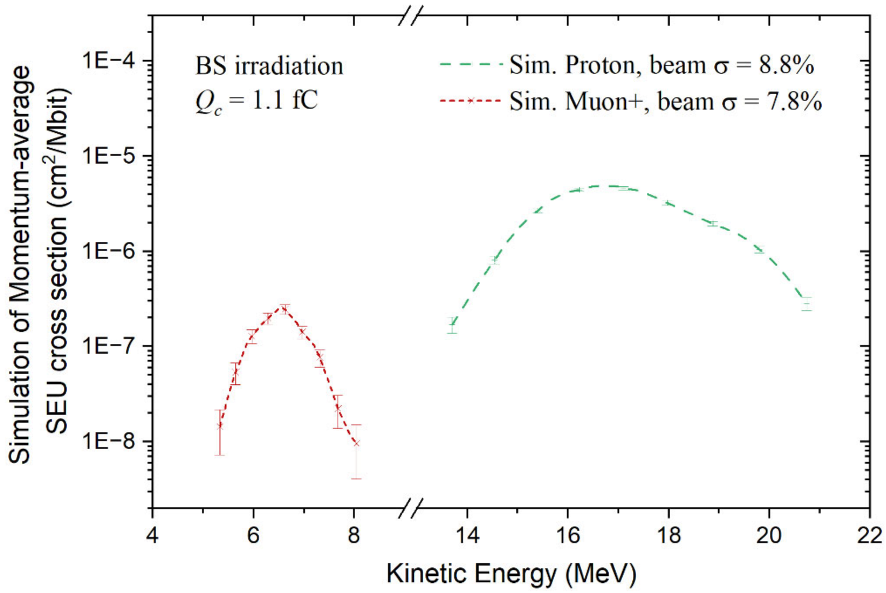

Figure 4.3 Comparison of the kinetic energy dependence of SEU cross sections in BS irradiation between positive muon (red) and proton (green).

4.3.2 Evaluation by Effective SEU Fluence

Similar to the process of defining the effective SEU fluence of the positive muon in Section 3.4.1, the deposition energy of protons in the SV to cause SEUs should have the same threshold value (E_{th}) with positive muons. The deposition energy of protons depends on their kinetic energy before entering the SV. Due to stochastic processes such as energy straggling and multiple scattering in device materials, the kinetic energy of the proton just before the SV has a distribution even for mono-energetic protons. Using simulation, the energy spectrum in BS irradiations was calculated just before the SV for 17.1-MeV protons. The result is shown with the black curve in the upper panel in Figure 4.4. The red curve indicates the energy spectrum of the protons with energy deposition over E_{th} in SV, and the integrated values of the red curves are defined as "effective SEU fluence" for the proton. It means the relative fluence of protons that are effective for inducing SEUs. The energy spectrum and effective fluence are compared with the results of 6.63-MeV (38-MeV/c) muons, shown in the lower panel of Figure 4.4.

The effective SEU fluences for 17.1-MeV protons and 6.63-MeV positive muons are given by ϕ_p and ϕ_m, respectively. They differ because the muon energy distinction before the SV differs from the proton one due to the energy straggling, which is explained in Section 1.4. Their ratio k_{EFp} is obtained by

$$k_{\mathrm{EFp}} = \frac{\phi_p}{\phi_m} = 13.81 \pm 0.02\,, \tag{4-2}$$

where the error is estimated from the statistical error of the simulated effective SEU fluence. This ratio k_{EFp} could quantitatively estimate the impact of energy straggling on the ratio of the peak SEU cross-sections between proton and positive muons.

As shown in Figure 4.4, the protons and positive muons, which deposit energy in SV exceed E_{th}, have different energy windows just in front of the SV, i.e., the diverse range of the red curves. For a deeper understanding of the effective SEU fluence, the lower and upper limits of the energy window for both protons and positive muons can be determined by numerical calculation of the deposition energy in SV as a function of the kinetic energy using the stopping power, which is explained in Appendix. The results are shown in Figure 4.5. The kinetic energy dependence of the energy deposition in SV of the proton is shown with the green curve, while that of the positive muon is shown with the red curve. By setting the threshold deposition energy E_{th} to 0.025 MeV, one can find that the lower limits of positive muon and proton are equal to 0.025 MeV. The upper limit for proton is 0.48 MeV, while that for positive muon is 0.06 MeV. It is worth pointing out that this is a simplified calculation value. Since the multiple scattering makes some particles above the upper limit deposit energy above E_{th} in the SV, the actual window in Figure 4.4 has a tail near the upper limit.

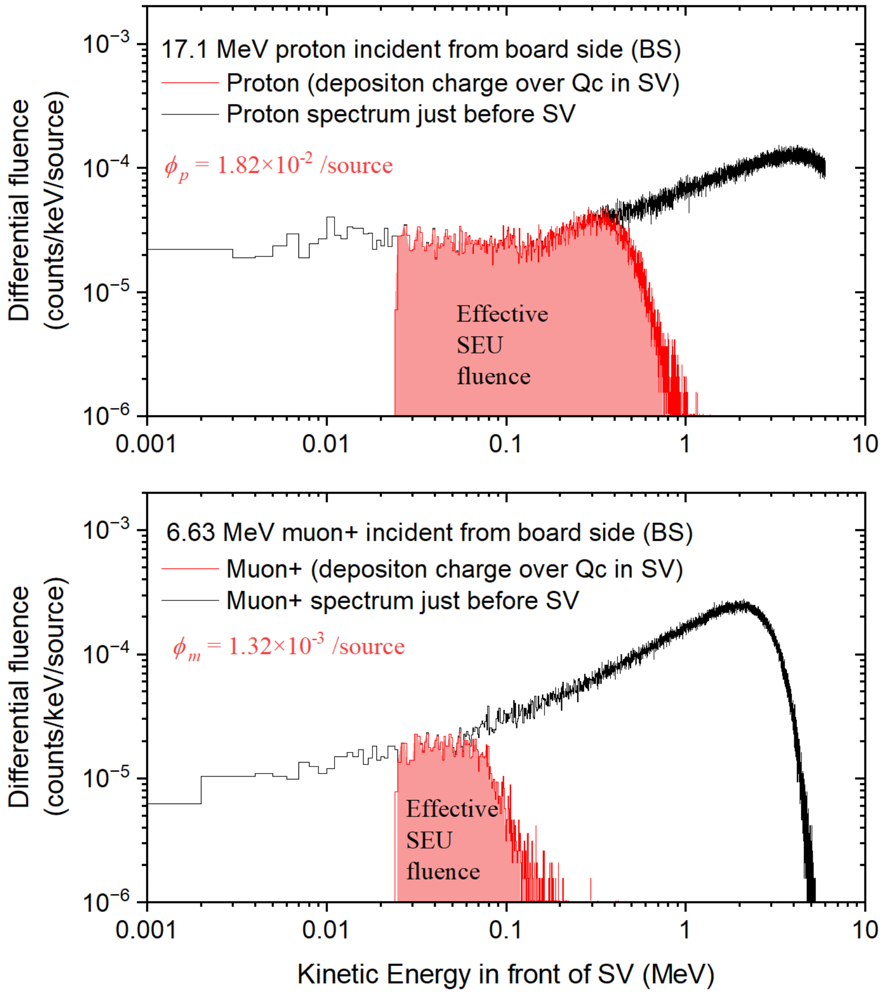

Figure 4.4 Energy distributions of positive muons and protons before entering the SV with different irradiation sides are shown with black curves. The lower panel shows the positive muon case, while the upper panel shows the proton case. The red curves mean the positive muons with deposition energy over E_{th} in SV.

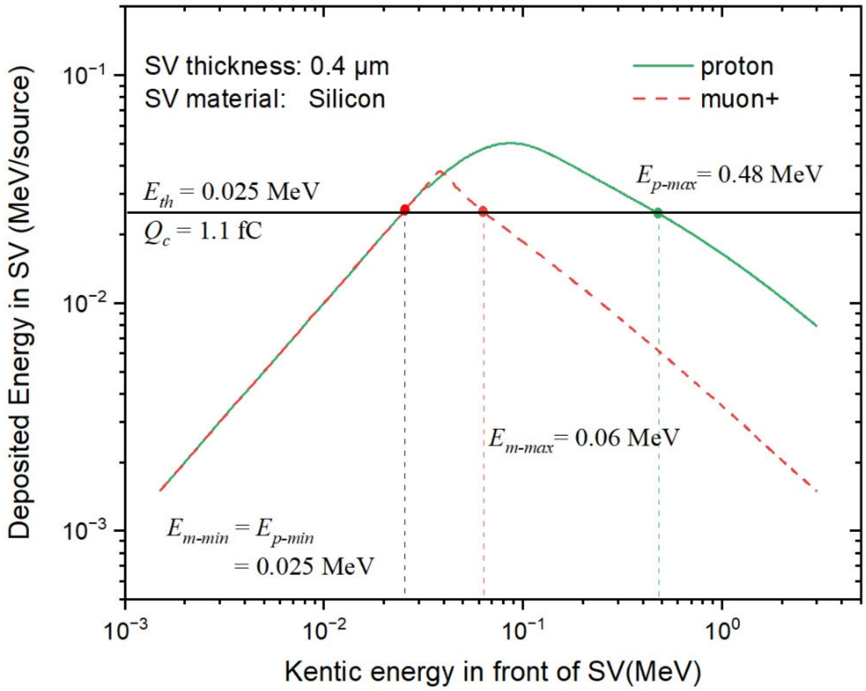

Figure 4.5 The deposition energy E_d as a function of incident particle kinetic energy E_k just before entering SV. The green curve represents the case of proton, while the red one represents the case of positive muons.

4.4 Predicting Muon-Induced SEUs Using Proton Test

4.4.1 Energy Mapping and Equivalence Method

As mentioned in Section 1.4, the incident energy of a proton is always greater than that of a muon when their Bragg peaks overlap at the same depth. Therefore, a one-to-one mapping can be established between the incident energies of the two.

First, we determine the proton energy equivalent to the muon energy so that both Bragg peak positions overlap. Hereafter, this process will be referred to as energy mapping. Because the Bragg peak is located near the end of the range, the mapping method can be represented by the following equation:

$$E_p = R_p^{-1}[R_m(E_m)] \ , \tag{4-3}$$

where E_m denotes muon energy, E_p denotes mapped proton energy, R_m indicates muon range, and R_p^{-1} represents the reverse range function of the proton.

Second, the energy mapping procedure described in Equation (4-3) is applied to several muon energy points within the muon window of vulnerability [46], which is the energy range of incident muons causing SEUs. These muon energy points are denoted by the vector **M** = (E_{m1}, E_{m2}, …, E_{mi}, …, E_{mn}). Because of the narrow window [46], a few energy points are usually sufficient. The mapped proton energies are denoted by the vector **P** = (E_{p1}, E_{p2}, …, E_{pi}, …, E_{pn}). The relation between E_{mi} and E_{pi} is as follows:

$$E_{pi} = R_p^{-1}[R_m(E_{mi})]. \tag{4-4}$$

As mentioned in Section 4.3, the difference in SEU cross sections between a positive muon and the corresponding proton is expected to be significant. Thus, a scaling factor k_S is newly introduced to make a correlation between the experimental proton-induced SEU cross-sections and the muon-induced ones. Although the k_S factor is energy-dependent, we found that it is nearly constant if one can choose a slightly broader energy spectrum of incident protons than that of incident positive muons. Thus, the following relationship exists between the muon SEU cross section and the proton one:

$$\sigma_{<SEU>m}(E_{mi}) = \frac{\sigma_{<SEU>p}(E_{pi})}{k_S}. \tag{4-5}$$

A detailed discussion on the determination of k_S will be given in Section 4.4.2.

4.4.2 Adjustment of Proton Beam Width

The proton simulations with different widths of incident energy spectrum assuming a Gaussian shape were performed for the 65-nm bulk SRAMs used in the previous muon experiment. The simulated SEU cross sections are shown in Figure 4.6, and the corresponding scaling factors k_S are plotted as a function of incident energy in Figure 4.6. The k_S factors are determined using equation (4-5), namely, the ratio between the measured muon SEU cross-sections and the corresponding proton SEU cross-sections obtained by the present simulation.

As shown in Figure 4.6, a broader incident energy spectrum leads to a broadening of the energy-dependent cross-section curve. As a result, Figure 4.7 shows that the k_S factor changes remarkably with energy when the energy spectrum width of the proton is 7.8%, the same as that of the muon beam. Only when the energy spectrum width of the proton is slightly larger than the muon energy spectrum, i.e., 8.8%, k_S is relatively stable and equation (4-5) holds. The reason will be discussed in Section 4.4.4.

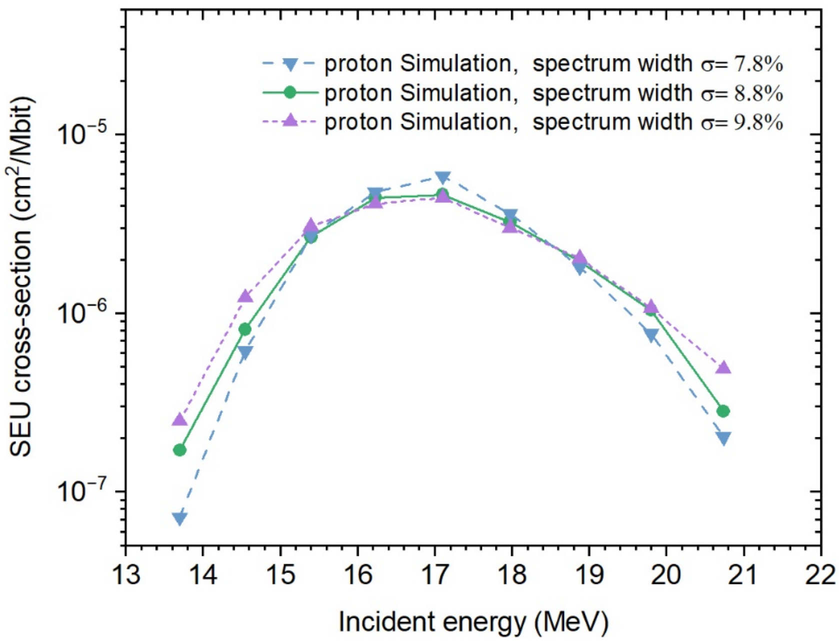

Figure 4.6 Simulated proton SEU cross-section. The spectrum widths of incident protons are 7.8%, 8.8%, and 9.8% of the standard deviation.

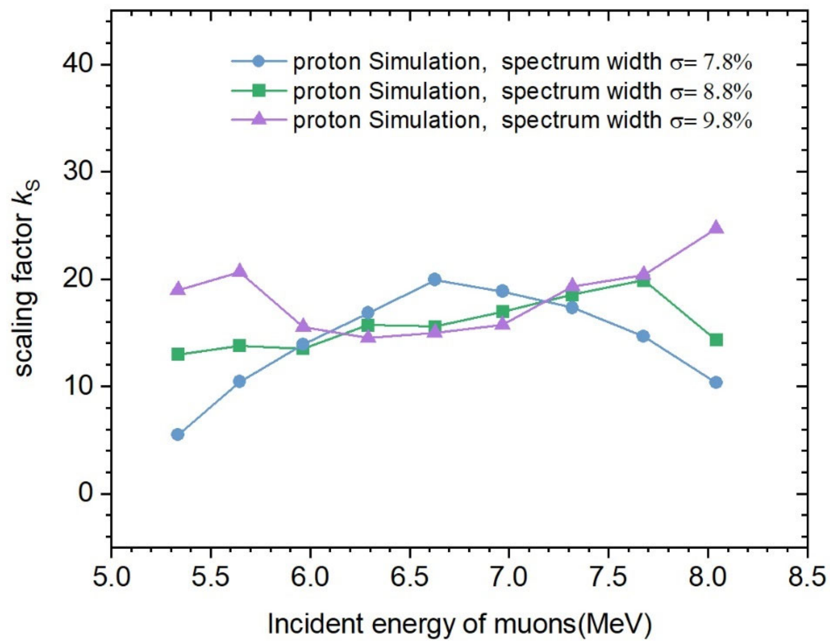

Figure 4.7 The energy-dependent scaling factor k_S determined by the simulation for 65-nm bulk SRAM.

4.4.3 Equivalence of the SEU Cross-sections

Using equation (4-5), this study has predicted the positive muon SEU cross-sections using the simulated proton SEU data as the experimental data. The expected result with the green dashed line is compared to the measured positive muon SEU cross-sections in Figure 4.8.

The final scaling factor k_S used in equation (4-5) for getting Figure 4.8 is 15.38, which is the average value of the energy-dependent k_S when the standard deviation of the proton is 8.8%, as plotted with the green points in Figure 4.7. The scaling factor k_S is similar to the ratio k_{CSp} of peak SEU cross sections in proton and muon simulation, which is 15.28 in equation (4.1). They are slightly different because the calculation of k_{CSp} uses simulated peak muon SEU cross-sections. In contrast, the analysis of k_S uses experimental muon values and averages over the energy points.

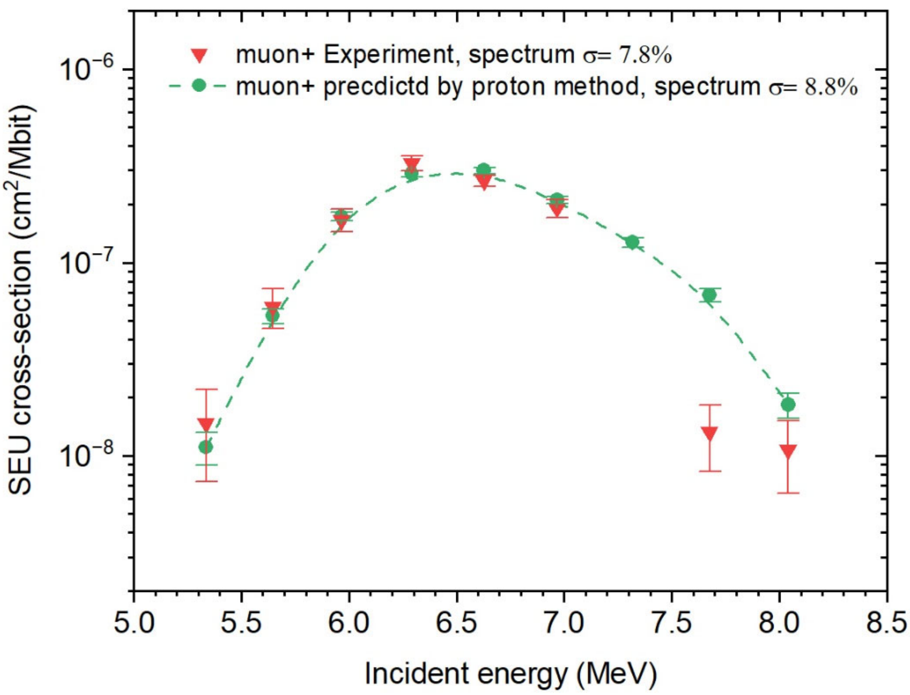

Figure 4.8. The predicted positive muon SEU cross sections by proton simulation and the measured positive muon SEU cross sections for 65-nm bulk SRAM. The spectrum width of positive muons is 7.8% in the muon experiment and 8.8% in the proton simulation. The determined k_S value is 15.38.

The positive muon SEU cross-sections predicted by the newly proposed method agree well with the experimental data. Since the proton SEU cross section has been created by the simulation in the present work, a new measurement of the proton SEU cross section for the same SRAM device will be essential to demonstrate the effectiveness of the method in the future.

It should be noted that the method to predict the positive muon SEU cross-section using the proton test proposed in this chapter is essentially mapping the energy-dependent SEU of a proton with that of positive muons, which both approximates a Gaussian distribution. Therefore, this method has a limitation, that the peak of the SEU caused by proton direct ionization must be significantly higher than the tail caused by nuclear reactions. For example, when the package or device board material is too thick, greater energy straggling will significantly reduce the peak SEU caused by proton direct ionization. What's more, as the thickness of the SV decreases or the critical charge increases, the peak value of the SEU cross-section due to direct ionization becomes relatively lower compared to the cross-section caused by nuclear reactions. In the above-mentioned situations, particular attention should be given to whether the k_S can still maintain relative stability when using the method.

4.4.4 Discussion on Energy Width Adjustment of the Proton Beam

As mentioned in Section 4.4.2, the condition for equation (4-5) to hold, i.e., for the scaling factor k_S to be insensitive to the incident energy, is that the spectrum width of the proton beam is chosen to be slightly larger than that of the muon beam. It is explained by the effective SEU fluence analysis of protons and positive muons in the case of different energy widths of proton beams. In other words, the analysis of the k_{EF} value derived from the ratio of effective SEU fluence is used to evaluate the influence of proton beam width because k_{EF} can better reflect the mechanism of the phenomenon.

The effective SEU fluence is mainly related to two typical parameters, i.e., the kinetic energy of the incident particle and the SV depth from the irradiation surface. If the kinetic energy of the positive muon and that of the corresponding proton are chosen by the energy matching relation expressed by equation (4-4), the respective effective SEU fluences, $\phi_m(d)$ and $\phi_p(d)$, are given as a function of the SV depth, d, using simulation. They are shown in Figure 4.9. The upper panel of Figure 4.9 shows the effective SEU fluences when the SV depth is set to be 1.8 mm for the 6.63-MeV mono-energetic muon, the corresponding mono-energetic 17.1-MeV proton, and the 17.1-MeV proton with a Gaussian spectrum with standard deviation σ = 1.7%. The results of slightly different incident muon energy of 6.46 MeV are also plotted for comparison in the lower panel. In the case of mono-energetic muon and proton, the scaling factor $k_{EF}(d_0)$ derived from the effective fluence is indicated in Figure 4.9. When the proton beam has a Gaussian spectrum with σ = 1.7%, the scaling factor $k'_{EF}(d_0)$ is also presented in Figure 4.9. From a comparison of both the cases of 6.63-MeV and 6.46-MeV muons, it is clear that the variation in $k_{EF}(d_0)$ is significant while that in $k'_{EF}(d_0)$ is much smaller, which suggests that the scaling factor is much less sensitive to incident energy in the case of a slightly broader proton energy spectrum.

Moreover, the modeling process in simulation may introduce dimensional errors with the actual device. The sensitivity of the scaling factor to the dimensional error of SV depth during the modeling process is also discussed. The incident muon energy is fixed to be 6.63 MeV, and the corresponding proton energy is 17.1 MeV, as shown in the upper panel of Figure 4.9. The actual SV depth from the irradiation surface on the device is fixed to be d_0 = 1.8 mm, and the SV depth in the simulation model differs from the actual depth by Δd. Thus, the relative modeling error of the SV depth is defined by

$$R_d = \frac{\Delta d}{d_0}. \tag{4-6}$$

The sensitivity of the scaling factors to the relative modeling error in two different cases of a mono-energetic proton beam and a proton beam with 1.7% width was evaluated from the following equations:

$$S_k(R_d) = \frac{k_{EF}(d_0 + R_d d_0) - k_{EF}(d_0)}{k_{EF}(d_0)}, \tag{4-7}$$

$$S_{k'}(R_d) = \frac{k'_{EF}(d_0 + R_d d_0) - k'_{EF}(d_0)}{k'_{EF}(d_0)}, \tag{4-8}$$

where $S_k(R_d)$ represents the sensitivity of the scale factor to the relative modeling error R_d for the mono-energetic proton beam, while $S_{k'}(R_d)$ represents the sensitivity for the proton beam with 1.7% width. Both $S_k(R_d)$ and $S_{k'}(R_d)$ are plotted as a function of R_d in Figure 4.10.

The sensitivity of the scaling factor k_{EF} reaches nearly 100% for only a 2% variation of R_d in the case of the mono-energetic proton beam, which indicates that the scaling factor is susceptible to the relative modeling error of SV depth. In contrast, the sensitivity of k'_{EF} to R_d is at most 2% to 10% for the proton beam with a 1.7% Gaussian spectrum, resulting in less sensitivity of the scaling factor to the relative modeling errors of the SV depth.

The above discussions suggest that the scaling factor is robust to the incident energy variation and relative dimensional error of the SV depth when the energy spectrum of the proton beam has a suitable width. This condition ensures the relationship between positive muon and proton SEU cross sections given by equation (4-5). Realistic proton beams used in proton irradiation tests are not necessarily mono-energetic and have a certain energy width. Thus, it is expected that equation (4-5) holds automatically in many cases.

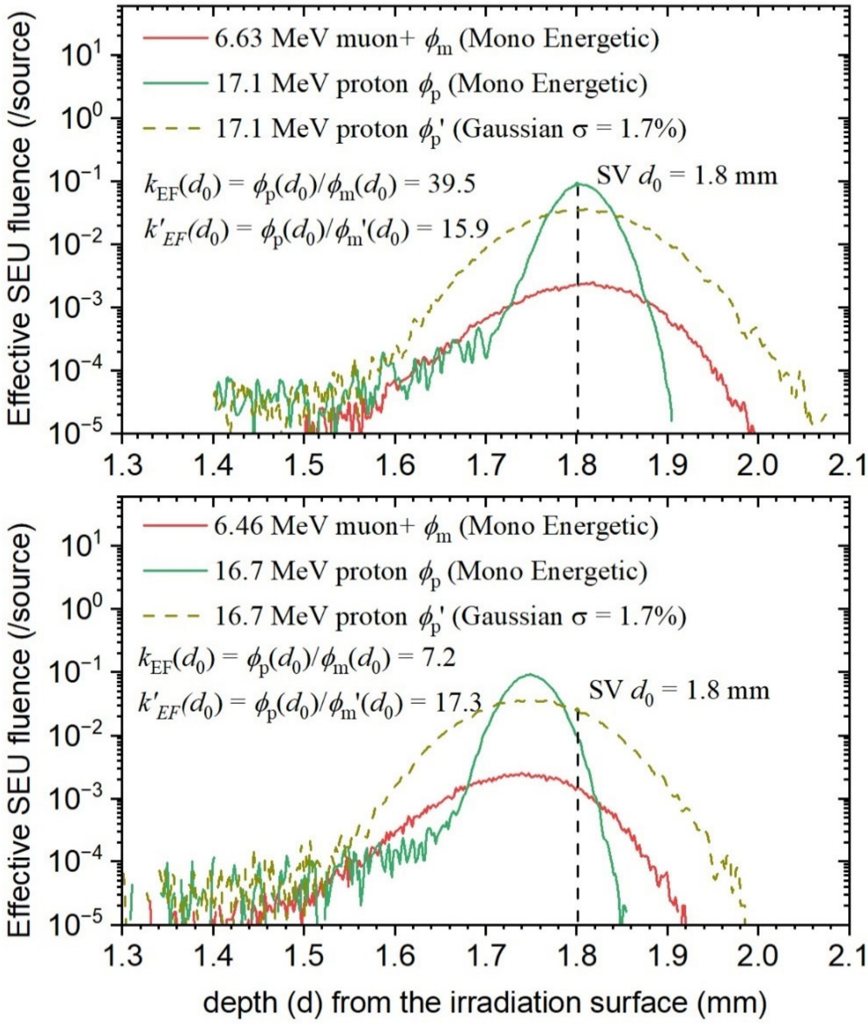

Figure 4.9 The effective SEU fluences, $\phi_m(d)$ and $\phi_p(d)$, as a function of the SV depth, d. The mono-energetic protons are plotted with the green solid curves, while the mono-energetic positive muons are plotted with the red ones. The protons with Gaussian spectrum $\sigma = 1.7\%$ are plotted with the olive dash curves. The upper panel is the case of the 6.63-MeV muon and the corresponding proton, and the lower one is the 6.46-MeV muon and the corresponding proton.

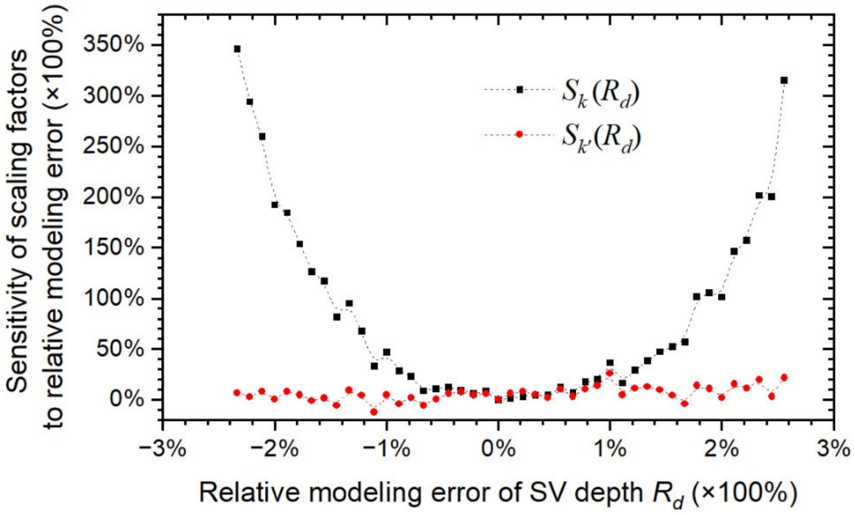

Figure 4.10 Sensitivity of scaling factors k_{EF} and k'_{EF} concerning the relative error of depth R_d in modeling of SV. The black curve represents the sensitivity of the scaling factor k_{EF} to the relative error of SV depth for a mono-energetic proton beam. The red curve shows the sensitivity of scaling factor k'_{EF} concerning the case using a proton beam with a 1.7% Gaussian spectrum.

4.5 Conclusion

After introducing the proton simulation model, the kinetic energy-dependent proton SEU cross-sections in BS irradiation were derived by simulation and compared to the simulation result of the positive muon. The peak SEU of the positive muon was at 6.63 MeV, while that of the proton was at 17.1 MeV because protons have a lower penetrating ability than muons and thus require more initial kinetic energy to pass through the same thickness to reach the SV. The magnitude of proton-induced SEU cross-sections is also more significant than that of the muon. Using simulation, the ratio of proton peak SEU cross-section in BS irradiation to that positive muon one (k_{CSp}) was 15.28. Then, the ratio of peak SEU cross-section between proton and positive muon was explained by the effective SEU fluence. The ratio k_{EFp}, which is derived from the effective SEU fluence, was 13.81.

By comparison between proton and positive muon-induced SEU cross-sections in 65-nm bulk SRAMs, a new method based on proton accelerating test and Monte Carlo simulation to predict SEUs caused by positive muons has been proposed. The proton energy is mapped to the muon one by making their Bragg peaks overlap at the SV in a device. Using the new method, the positive muon SEU cross-sections can be estimated using the measured proton SEU cross-sections dividing a scaling factor k_S after an appropriate width of the incident proton energy spectrum and the critical charge of the device was selected by simulation. The k_S for the 65-nm bulk SRAMs was estimated to be 15.51. The muon SEU cross-section predicted by the proton simulation was found to reproduce the experimental muon SEU data fairly well.

Moreover, the robust analysis suggests that the scaling factor k_S is robust to the incident energy variation and robust to the relative dimensional error of the SV depth, when the energy spectrum of the proton beam has a suitable width. This condition ensures the relationship between positive muon and proton SEU cross-sections given by (4-5).

5 Estimation of the SERs on Bulk SRAMs

5.1 Introduction

The Soft Error Rate (SER) is an essential parameter for evaluating the resistance of electronic devices to cosmic ray-induced SEUs. The SERs can be calculated from SEU cross-sections measured by acceleration irradiation tests. However, Chapters 2 and 3 show that the irradiation side influences the measured SEU cross-sections. Therefore, we need to explore whether the irradiation side also affects the SER estimation. Thus, the impact of the experimental SEU cross-sections on the SER prediction in different irradiation sides is investigated by the regular estimation method based on the conventional perpendicular irradiation tests. The SERs of positive and negative muons in BS irradiation are compared with the proton SERs.

Moreover, since the incident angle dependence of muon-induced SEUs is reported in [45], this study performed the simulations to investigate the influence of incidence angle on SEU cross-section. Finally, in subsection 5.3, this study develops a method to evaluate the muon-induced SER under a realistic environment considering the zenith angle distribution of muon flux.

5.2 SER Estimation Based on the Perpendicular Irradiation

5.2.1 Estimation method

Typically, SER prediction models based on acceleration tests use the measured SEU cross-sections where the device board is perpendicular to the irradiation beams [17], [46]. In this case, The SER under a terrestrial environment can be estimated by the following equation:

$$\mathrm{SER} = \int_0^\infty \varphi(E)\sigma(E)\,dE\,, \tag{5-1}$$

where $\varphi(E)$ represents the flux of muons within the energy range [E, $E+dE$] in a specific terrestrial environment, and $\sigma(E)$ is the SEU cross-section as a function of kinetic energy E. The fluxes of cosmic rays like protons and positive and negative muons can be calculated by the EXPACS tool employing a PHITS-based analytical radiation model (PARMA) [10]. The mono-energetic SEU cross-sections can be derived from the irradiation tests. In particular, the mono-energetic SEU cross-sections for positive and negative muons came from the simulations, in which the muon irradiation tests calibrate the model because the mono-energetic muon beam is not available now.

5.2.2 Impact of Irradiation Side on Muon SER Estimation

In Figure 5.1, the fluxes derived from the EXPACS calculation are shown in the energy range sensitive to inducing SEUs in the 65-nm SRAM device. The fluxes of positive and negative muons are very close and increase with increasing kinetic energy. It is assumed that mono-energetic muons are incident to the device in the vertical direction. The simulated SEU cross-sections of the mono-energetic positive and negative muon, $\sigma(E)$ in equation (5-1), are plotted for both PS and BS irradiations in Figure 5.2.

Using the method expressed by equation (5-1), the estimated SERs for positive and negative muons based on the PS and BS irradiations are shown in Figure 5.3. The unit of SER is FIT/Mbit, where FIT means Fault in Time, i.e., the number of SEU occurrences per 10^9 h. For both positive and negative muons, the estimated SERs for the BS irradiation are slightly larger than those for the PS irradiation. The difference is at most 21%. In this case, the impact of the irradiation side on SER prediction is relatively weak.

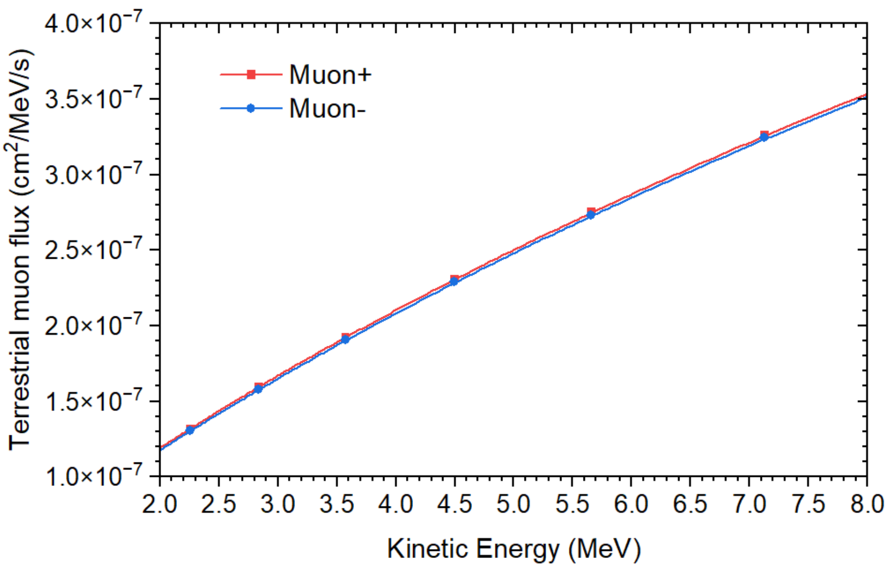

Figure 5.1 Fluxes of positive and negative muons within the energy range sensitive to inducing SEU in the 65-nm bulk SRAMs at sea level in Tokyo. The result is calculated by using EXPACS [10].

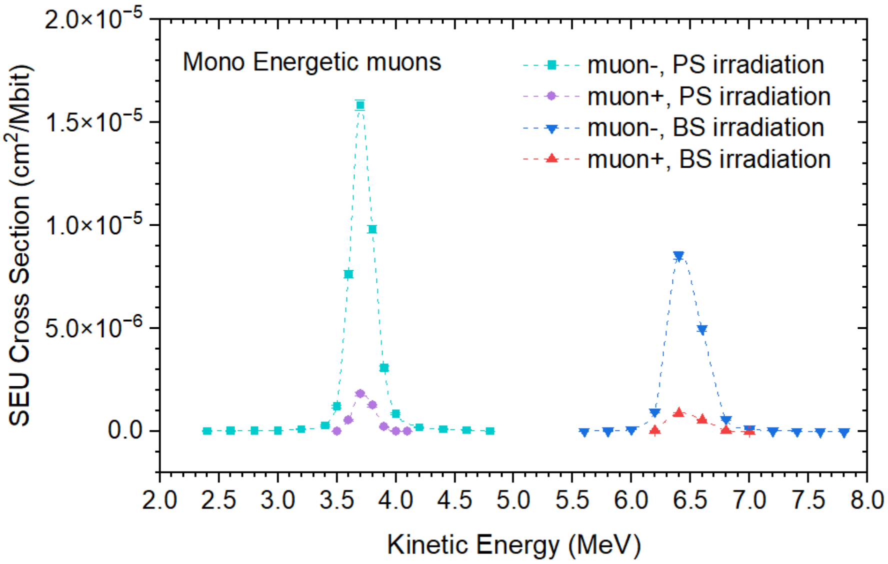

Figure 5.2 Kinetic energy-dependent SEU cross-sections induced by mono-energetic positive and negative muons in 65-nm bulk SRAM with PS and BS irradiations. The results are derived from Geant4 simulations.

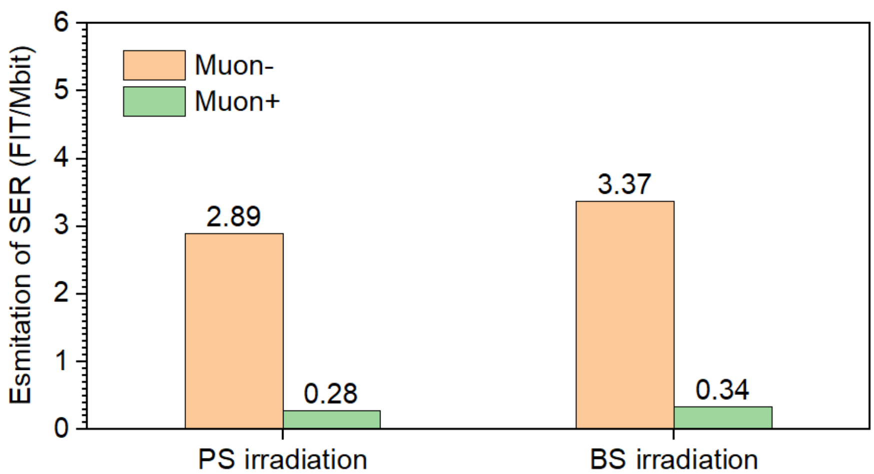

Figure 5.3 The estimated SERs of positive and negative muons for 65-nm bulk SRAM. The SEU cross-sections derived from the PS and BS irradiation tests are used in the estimation.

This weak dependency can be understood as follows. The SV is at a deeper depth in the BS irradiation case than in the PS irradiation case. As a result, the peak position of SEU cross-sections shifts to higher kinetic energy, resulting in larger $\varphi(E)$ in equation (5-1). On the other hand, the energy straggling and multiple scattering is more considerable because the muon penetration path to SV is longer in the BS irradiation case, resulting in a smaller peak cross-section, i.e., a smaller $\sigma(E)$ in equation (5-1) as shown in Fig. 11. Finally, the SERs defined by equation (5-1) are similar between PS and BS irradiations.

5.2.3 Comparison of Muon and Proton SER in BS Irradiation

In Figure 5.4 (a), the proton flux at ground level derived from the EXPACS calculation is shown as a function of the kinetic energy. And the simulated SEU cross-sections of the mono-energetic proton in BS irradiation are plotted in panel (b) of Figure 5.4. Figure 5.4 (b) shows that the SEU cross-sections of mono-energetic protons exhibit a peak in the low-energy region due to direct ionization. In the high-energy region, the SEU cross-sections of protons form a gradually increasing platform, which is primarily caused by nuclear reactions (inelastic scattering).

Using equation (5-1), the proton-induced SER on 65-nm bulk SRAM is calculated and compared with positive and negative muons-induced SERs in Table 5.1. The estimated muon SERs for the 65-nm bulk SRAM are consistent with Manabe's work [60]. The SER of protons is predicted to be 44.23 FIT/Mbit, which is more significant than Hubert's result (about 20 FIT/Mbit) [19]. Although the proton SER in 65-nm bulk SRAMs is more significant than the muon one, it is still not a major factor when compared with the neutron SER from [60]. And due to lower penetration performance, proton flux is supposed to be significantly lower in an indoor environment where electronic devices including the SRAMs are used. Thus, proton SER may not be so severe.

Table 5.1 The predicted SER for proton and positive and negative muons on 65-nm bulk SRAM based on simulation of BS irradiation.

Cosmic ray	SER [FIT/Mbit]
Proton	44.23
Muon+	0.34
Muon–	3.37

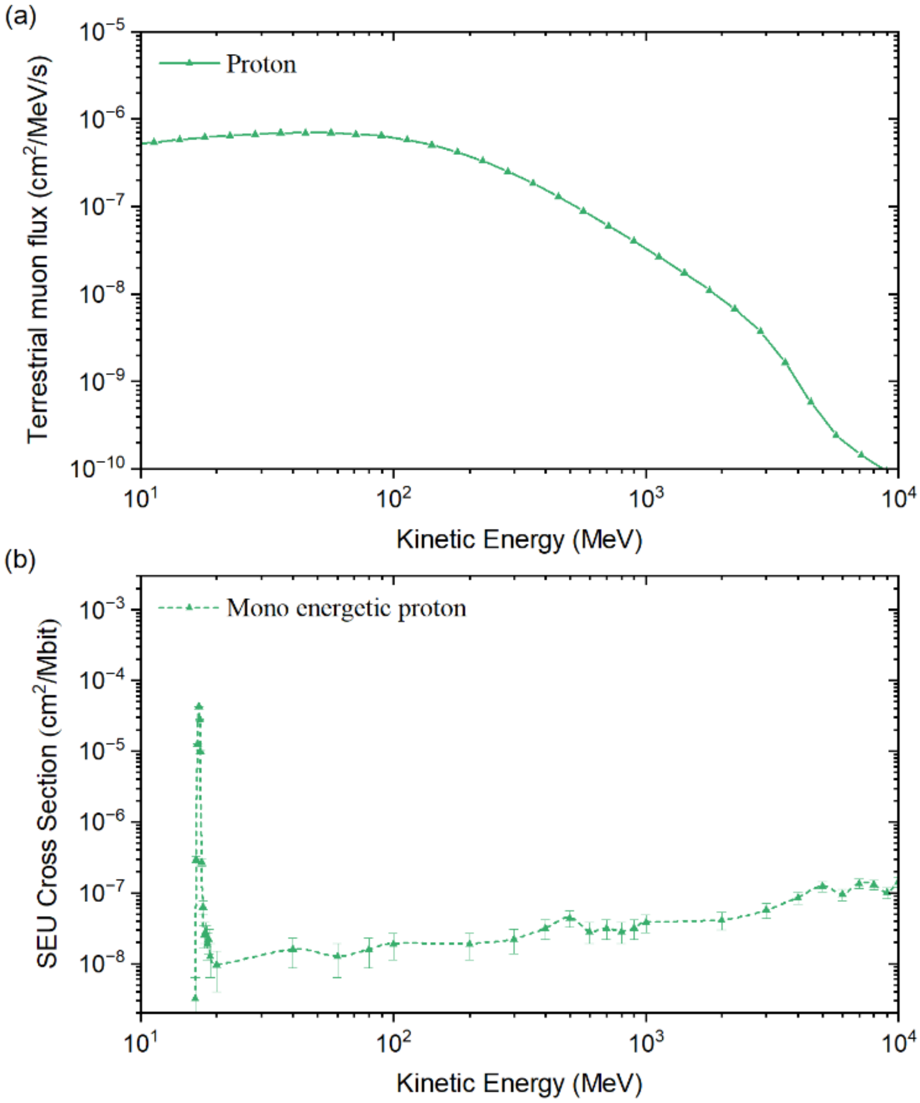

Figure 5.4 Panel (a) shows the proton flux at ground level derived from the EXPACS calculation. Panel (b) shows the kinetic energy-dependent SEU cross-sections induced by mono-energetic protons in 65-nm bulk SRAM based on Geant4 simulation of BS irradiations.

Additionally, to investigate the contribution of protons with different energies to the SER, the energy differential SER is plotted in panel (a) of Figure 5.5. The integrated result of the differential SER is shown in panel (b) of Figure 5.5 as a function of the upper limit energy of integration in equation (5-1).

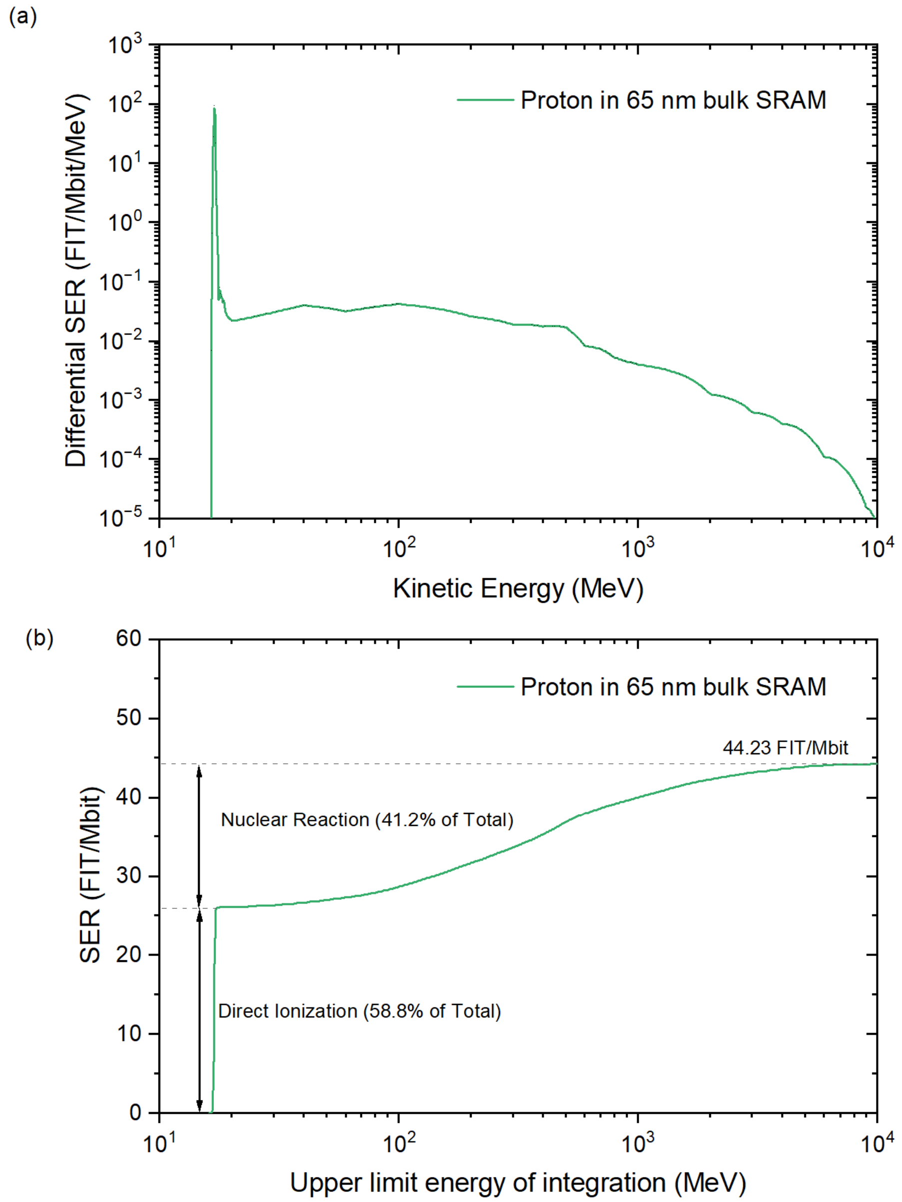

Figure 5.5 Panel (a) shows the kinetic energy differential SER of the proton on 65-nm bulk SRAM. Panel (b) shows the integrated result of the differential SER versus the upper limit energy of integration in equation (5-1).

Figure 5.5 (b) shows that although the peak of the differential SER caused by direct ionization is very narrow, it contributes significantly to the proton SER on 65-nm bulk SRAMs, accounting for 58.8% of the total. As for the SER caused by proton nuclear reactions, it contributes 41.2% to the total and cannot be ignored, although its differential SER is relatively small. This is because the kinetic energy range of its differential SER extends from 20 MeV to over 10 GeV. Moreover, the differential SER rapidly decreases beyond 1 GeV, and the variation of SER with the upper limit of integration becomes gradually stable until it almost remains constant. This is due to a rapid decrease in proton flux at ground level.

5.3 Realistic SER Estimation Considering the Zenith Angle Distribution of Cosmic Rays

Different incident angles of muon beams result in variations of penetration depths before reaching the SV. A test of negative muons-induced SEUs on the same 65-nm bulk SRAM at an incidence angle of 45 degrees from the BS was reported in [45]. This study also performs simulations with different incidence angles in Section 5.3.1 to see how the incident angles influence the muon-induced SEUs because the muon flux on the ground is known to have a zenith angle distribution. Then, the estimation of soft error rates (SERs) at ground level by considering the incident angle dependence of muon-induced SEUs is presented in Section 5.3.3. The results are compared with the estimated SERs using the measured SEU data by conventional irradiation tests in which a device board is placed perpendicular to the incident beam.

5.3.1 Impact of Incidence angle on SEU cross-sections

In the previous paper [45], a negative muon irradiation test for the same 65-nm bulk SRAMs was performed with a device board tilted 45 degrees against the vertical incidence, as shown in an inset illustration in Figure 5.6. The shift of the peak position of the SEU cross-section relative to the vertical incidence was reported. This study calculated the SEU cross-sections as a function of incident momentum using the simulation method with Geant4 described in Chapter 3. The result is compared with the normalized experimental data in Figure 5.6 since only the normalized cross-section is given experimentally. The simulated peak position is consistent with the experimental result, and the normalized cross-sections also agree with the experimental one. Thus, it was found that this simulation method can also be applied when muons are irradiated obliquely.

Then, this study performed further simulations for a wide range of angles to investigate the effect of incident angle on the SEU cross-section. The result is shown in Figure 5.7. The rotation angle of the device board on the x-axis is marked with θ, equal to the incident angle. Since the penetration depth of the negative muons before reaching the SV increases with θ, the peak position of simulated SEU cross-sections moves toward higher momenta. On the other hand, the energy straggling and multiple scattering become more pronounced with increasing penetration depth, resulting in a lower effective SEU fluence. This reduces the peak cross-section. The SEU cross-section at 45-degree incidence is approximately 71.6% of that at 0-degree incidence.

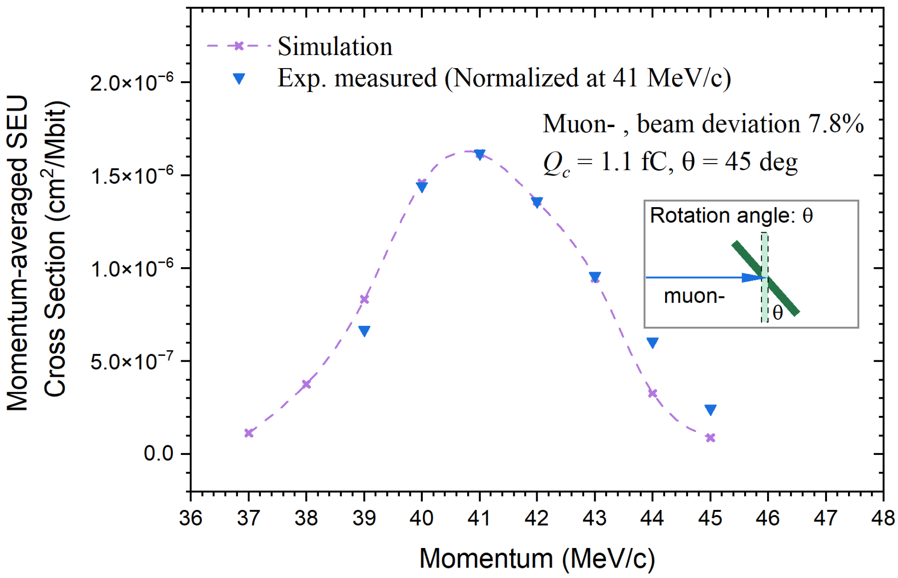

Figure 5.6 Comparison of simulated SEU cross-sections for a 45-degree negative muon incident from the board side with normalized experimental data. The measured values in irradiation tests are taken from [45] and normalized to the simulation results at 41 MeV/c.

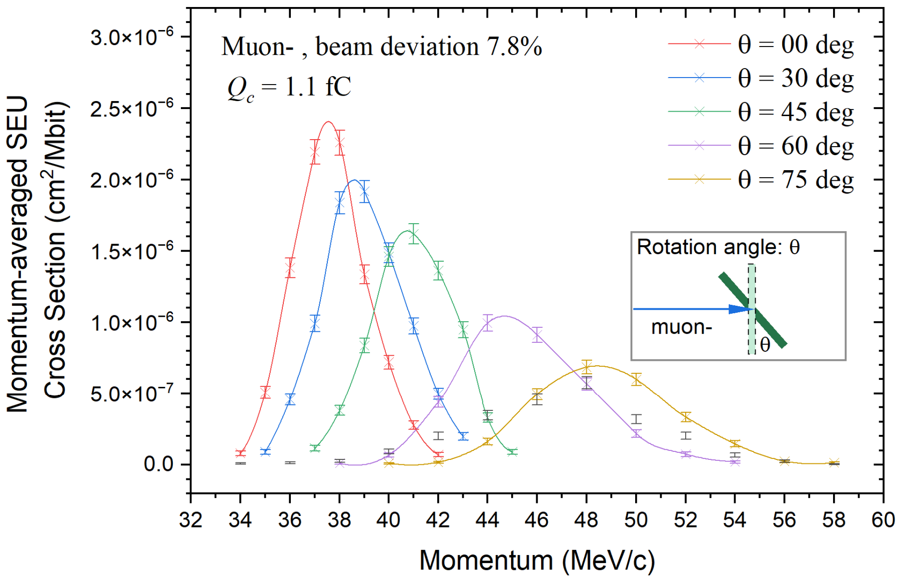

Figure 5.7 Simulation results of the momentum-dependent SEU cross-sections for negative muon incident from the board side at different incidence angles.

5.3.2 Estimation method

Since the muon flux on the ground has a zenith angle distribution, the muon incident angle is expected to affect the SEU cross-section of the SRAM device. Equation (5-1) needs to be modified so that the zenith angle distribution of the muon flux can be considered as follows:

$$\mathrm{SER} = 2\pi \iint \varphi(E,\theta)\sigma(E,\theta)\sin(\theta)\,dEd\theta\,, \tag{5-2}$$

where $\varphi(E,\theta)$ represents the muon differential flux with zenith angle θ in the energy range $[E,\ E+dE]$, and $\sigma(E,\theta)$ denotes the muon SEU cross-sections as a function of kinetic energy and zenith angle. The numerical integration in equation (5-2) was performed using an angular distribution calculated at 15-degree intervals.

The zenith angle distribution of negative muon flux at ground level can also be calculated by EXPACS [10]. The mono-energetic SEU cross-sections as a function of kinetic energy and zenith angle can be obtained from the irradiation test. However, irradiation tests in varying incident angles require a lot of radiation time. Therefore, simulations can be performed using models calibrated with experimental data to get the SEU cross-sections.

5.3.3 Estimation Results

Figure 5.8 shows the calculated zenith angle distribution of negative muon flux at sea level by EXPACS [10]. The simulation-derived SEU cross-sections of mono-energetic negative muon for the 65-nm bulk SRAM with different incident angles for both PS and BS irradiations in Figure 5.9. Finally, Figure 5.10 compares the SER estimated by equation (5-2) with the SER for the perpendicular incidence estimated in Section 5.2.2. Both results are almost the same. This indicates that a vertical irradiation test is useful for estimating muon-induced SERs in terrestrial environments. However, further investigation will be necessary to confirm whether similar results can be obtained with different SRAM devices.

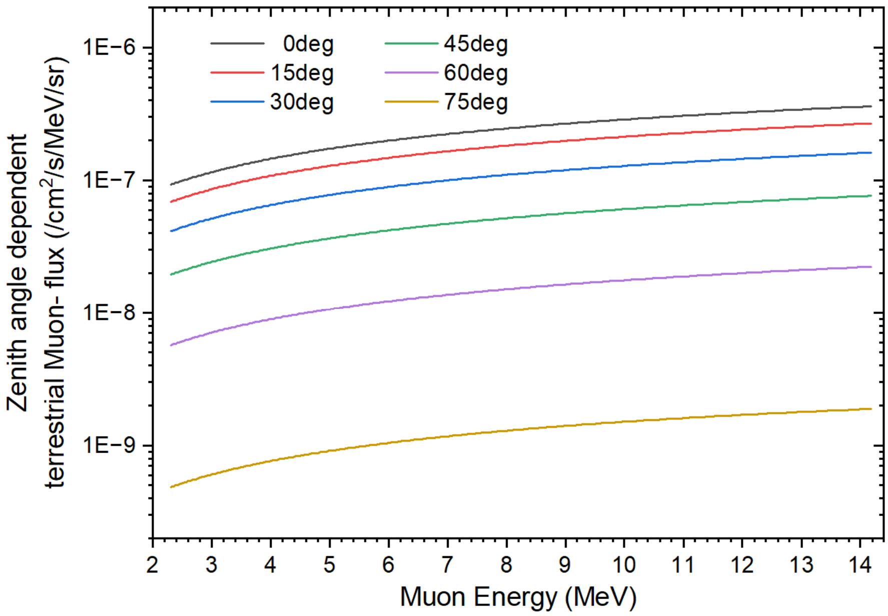

Figure 5.8 Differential fluxes of the negative muon with zenith angle θ within the energy range sensitive to inducing SEU in the 65-nm bulk SRAMs at sea level in Tokyo. The result is calculated by using the EXPACS [10].

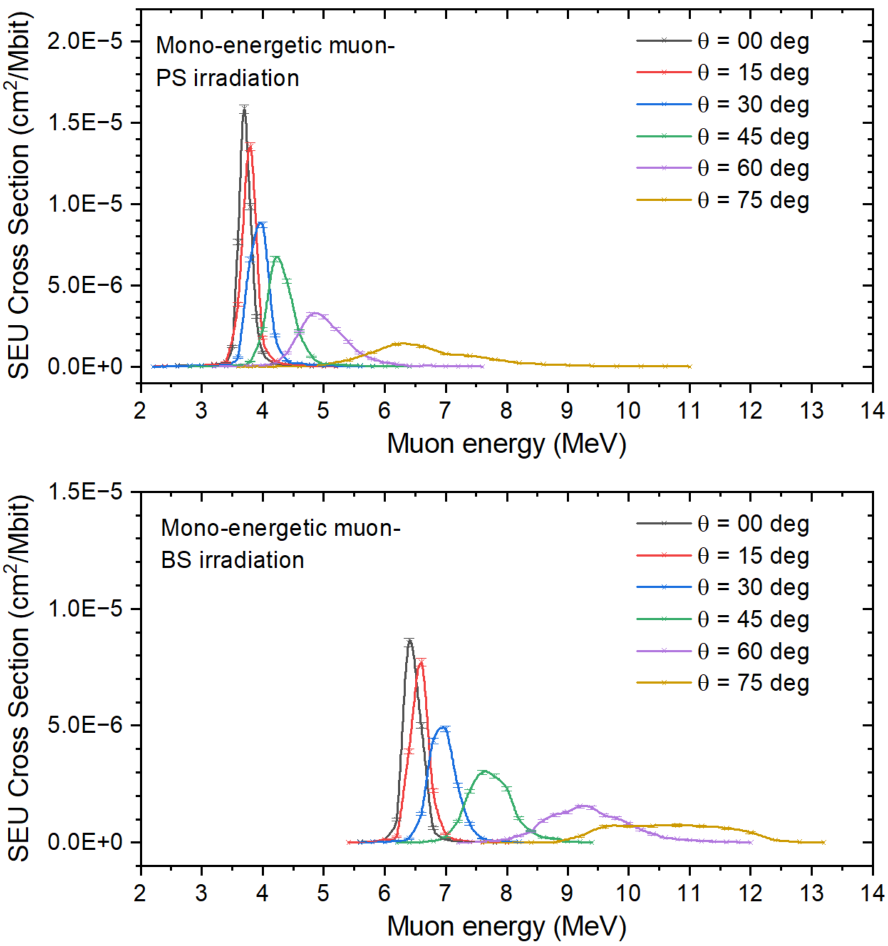

Figure 5.9 Mono-energetic negative muon-induced SEU cross-sections in 65-nm bulk SRAM with different incident angles in PS and BS irradiation.

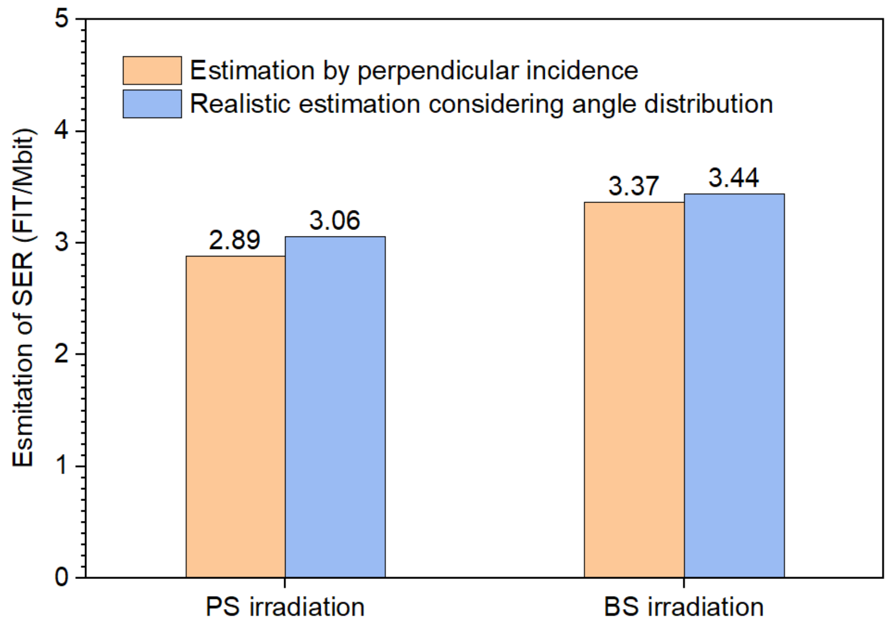

Figure 5.10 Realistic SER estimation of negative muon in 65-nm bulk SRAM considering the zenith angle distribution of muon flux in the terrestrial environment are compared with the approximate SER estimation derived from the perpendicular incidence.

5.4 Conclusion

The impact of the changed experimental SEU cross-sections on the SER prediction in different irradiation sides was investigated by the regular estimation method based on the conventional perpendicular irradiation tests. For both positive and negative muons, the estimated SERs for BS irradiation are slightly larger than those for PS irradiation, at most 21%. Thus, the impact of the irradiation side on SER prediction was found to be relatively weak.

The SERs of positive and negative muons in BS irradiations were compared with the proton. The result showed that the muon SERs for the 65-nm bulk SRAM are significantly less than the proton SER. The SER of positive muon, negative muon, and proton in 65-nm bulk SRAM were 0.34, 3.37, and 44.23 FIT/Mbit, respectively. For proton SER, direct ionization contributes 58.8%, while nuclear reactions contribute 41.2%.

Then, the dependence of the incident angle of muons on the SEU cross-section was investigated and analyzed. The incident angle affected the momentum and the magnitude of the peak SEU cross-sections. The peak momentum was at 38 MeV/c for 0-degree incidence, while at 41 MeV/c for 45-degree incidence. The SEU cross-section at 45-degree incidence was approximately 71.6% of that at 0-degree incidence.

Based on the incident angle-dependent SEU cross-sections, this study predicted the SERs under a more realistic environment by considering the zenith angle distribution of muon flux. The predicted SER was found to have no significant difference from that without zenith angle distribution for 65-nm bulk SRAMs.

In this Chapter, only muon and proton SERs estimations for 65-nm bulk SRAM were performed. However, the SER estimation on the device with smaller technology nodes, like 28-nm bulk and 12-nm FinFET SRAMs, are also necessary to verify whether the trend of muon and proton SER with technical node is shown as in Figure 1.7. The muon irradiation tests for 28-nm bulk and 12-nm FinFET SRAMs have been performed by Gomi et al. [78]. Their simulation analysis and SER estimation will be one of the future research topics of our group.

6 Summary and Conclusions

With the miniaturization of semiconductors and lower operating voltages, there is a growing interest in whether a large number of muons may be another source of SEUs (Single Event Upsets) through the direct ionization process and nuclear capture reaction for negative muons. As a background knowledge of this study, the mechanism of radiation-induced SEUs in SRAM, the fundamentals of cosmic rays in the terrestrial environment, the physical properties of positive and negative muons and protons, and the straggling in energy deposition are introduced at first. Moreover, a brief review of past muon and proton-induced SEU works is explained.

As the concern for muon SEUs is growing, many more experiments need to be performed. However, the SEU cross-sections and the SER (Soft Error Rate) predictions from acceleration tests highly depend on the experimental conditions. Since muons pass through different thicknesses and materials before reaching the Sensitive Volume (SV) in cases of varying irradiation sides, i.e., package side (PS) and board side (BS), variation of peak incident energy and energy straggling are expected to influence the muon-induced SEUs. Therefore, negative and positive muon irradiation tests of 65-nm bulk SRAMs were performed with two different irradiation sides, i.e., BS and PS in the past works. The results of the PS irradiation tests were newly analyzed in Chapter 2 and compared with those of the previous BS irradiation tests. It was found that the peak SEU cross-section is at 28 MeV/c for PS irradiation, which is not the same as 38 MeV/c for BS irradiation. The peak SEU cross-section for PS irradiation is approximately twice that of BS irradiation for both positive and negative muons.

To explain the difference in SEU cross-sections between PS and BS irradiation tests, a simulation analysis of measurement results is given in Chapter 3. The simulation method was introduced first, including the simulation tools (Geant4), physical process, geometry model, beam source, and SEU determination in simulation. Then, the critical momentum dependence of SEU cross-sections for positive and negative muons in BS irradiation was analyzed to determine the critical charge so that the simulation reproduces the measurement well. The critical charge was finally determined to be 1.1 fC. For negative muons, secondary particles released by muon capture contribute about 96% of the SEU. The momentum-dependent SEU cross-sections for positive and negative muons in PS and BS irradiations were derived using the simulation and compared with the measurement. The simulated SEU cross-sections with Geant4 agreed well with the measured ones for both PS and BS irradiation tests, except in the non-peak momentum region under PS irradiation.

Next, the concept of effective SEU fluence was introduced to quantitatively explain the impact of the irradiation side on the SEU cross-section. It was found that the measured ratios of the peak SEU cross-section for PS and BS irradiations, i.e., about two, are consistent with the ratios calculated from the effective fluence within the margin of error. From the analyses with the effective SEU fluence, this study revealed that the difference in observed SEU cross-sections between PS and BS irradiations is caused by the differences in energy straggling and multiple scattering due to changes in penetration depth depending on the irradiation sides.

On the other hand, the minimal muon test facilities worldwide make it challenging to conduct muon irradiation tests, and such muon-accelerating tests are often financially expensive. As the Low Energy Proton (LEP) induced SEU and its contribution to the SER have been investigated widely and reported to need to be considered at ground level, this study also established a method for predicting muon SEUs using a combination of proton testing and Monte Carlo simulation, after comparing positive muon and proton-induced SEU in 65-nm bulk SRAMs. The positive muon-induced SEUs in BS irradiation were compared with proton-induced ones by simulation in Chapter 4. The peak energy of the proton SEU cross-sections is 17.1 MeV, more significant than the peak energy of 6.63 MeV for the muon SEU ones. The peak cross-section of the proton is about 15 times as large as that of the positive muon. This difference was explained by the different characteristics of the energy deposition process between proton and positive muon, using effective SEU fluences.

Then, a new method was developed to predict the positive muon-induced SEU using proton tests and Monte Carlo simulation. The proton energy is mapped to the muon one by making their Bragg peaks overlap at the SV in a device. Using the new method, the positive muon SEU cross-sections can be estimated by introducing a scaling factor for the proton SEU cross-sections measured by a proton irradiation test after an appropriate width of the incident proton energy spectrum. Finally, the results of proton SEU simulation were used to assess the feasibility of the proposed method by comparing it with the previous experimental result of positive muon-induced SEUs for a 65-nm bulk SRAM in BS irradiation. The muon SEU cross-section predicted by the proton simulation was found to reproduce the experimental muon SEU data fairly well. Moreover, the discussions in Section 4.4.4 suggested that the scaling factor is robust to the incident energy variation and relative dimensional error of the SV depth when the energy spectrum of the proton beam has a suitable width.

The last content of this study is the SER estimation of 65-nm bulk SRAMs. First, the impact of irradiation side dependent SEU cross-sections on SER prediction was investigated by the regular estimation method based on the perpendicular irradiation tests. For both positive and negative muons, the estimated SERs for BS irradiation in the direction perpendicular to the device board were slightly larger than those for PS irradiation. However, the difference was at most 21%. Thus, the impact of the irradiation side on SER prediction was found to be relatively weak. The SERs of positive and negative muons in BS irradiations were compared with the proton SER. The result showed that the muon SERs for the 65-nm bulk SRAM are significantly less than the proton SER.

Then, this study investigated the dependence of the incident angle of muons on the SEU cross-section. As a result, the incident angle affected the momentum and the magnitude when the SEU cross-section formed the peak. This can also be explained by the penetration depth variation depending on the incident angle. Based on the incident angle-dependent SEU cross-sections, this study predicted the SERs under a more realistic environment by considering the zenith angle distribution of muon flux. As a result, the predicted SER was found to have no significant difference from that without zenith angle distribution. Therefore, experimental data from conventional irradiation tests in which a device board is placed perpendicular to the incident beam are expected to be useful in estimating muon-induced SERs on the ground.

In the future, some issues regarding muon and proton-induced SEU phenomena still need to be further investigated and should be included in the research plan. First, this study focuses on the testing and simulation study of the SEU cross-section and does not differentiate between Single Bit Upset (SBUs) and multiple cell upsets (MCUs), nor does it conduct a simulation study of the MCU phenomenon. Since there are studies that show that Monte Carlo simulation with a sensitive volume method is able to investigate the MCU phenomenon [79], [80], MCU simulation of the same 65-nm bulk is the study subject to be conducted in the next phase. Second, an accelerating test on the same 65-nm bulk SRAMs using a proton beam is in the plan to further demonstrate the method of predicting positive muon SEU cross-sections with proton tests and simulations proposed in Chapter 4. At last, the susceptibility of devices to soft errors is expected to increase with the miniaturization of semiconductors due to decreased critical charge. Therefore, it is planned to extend the current work of SEU testing, simulation, and SER prediction for SRAMs with smaller design rules than 65 nm, for instance, the 12-nm and 28-nm SRAMs.

Appendix A

The relationship between the deposition energy E_d and the kinetic energy E_k of the particles in front of the SV is obtained by the following numerical calculation.

First, divide the SV into n segments. The thickness of each section is d/n, the incident kinetic energy is denoted by E_i^k, and the deposition energy is represented by E_i^d, where i is from 1 to n. When the n is large enough, the stopping power within each segment is considered constant. Therefore, for a given incident kinetic energy E_k, its deposition energy E_d within the SV can be calculated by

$$E_d = \sum_{i=1}^{n} E_i^d, \tag{A-1}$$

where E_i^d could be obtained by following recurrence relations:

$$\begin{cases} E_{i+1}^k = E_i^k - E_i^d \\ E_i^d = S(E_i^k)\, d/n \\ E_1^k = E_k \end{cases}, \tag{A-2}$$

where $S(E)$ means the stopping power of a particle with energy E, which could be obtained from the database. The relationship between E_d and E_k is shown in Figure 4.4.

References

[1] J.-L. Autran and D. Munteanu, *Soft Errors: From Particles to Circuits*. CRC Press, 2017.

[2] M. Hashimoto, K. Kobayashi, J. Furuta, S.-I. Abe, and Y. Watanabe, “Characterizing SRAM and FF soft error rates with measurement and simulation,” *Integration*, vol. 69, pp. 161–179, Nov. 2019, doi: 10.1016/j.vlsi.2019.03.005.

[3] G. Abich, R. Garibotti, R. Reis, and L. Ost, “The Impact of Soft Errors in Memory Units of Edge Devices Executing Convolutional Neural Networks,” *IEEE Transactions on Circuits and Systems II: Express Briefs*, vol. 69, no. 3, pp. 679–683, Mar. 2022, doi: 10.1109/TCSII.2022.3141243.

[4] E. H. Ibe, *Terrestrial Radiation Effects in ULSI Devices and Electronic Systems*. John Wiley & Sons, 2014.

[5] W. Liao, S. Hirokawa, R. Harada, and M. Hashimoto, “Contributions of SRAM, FF and combinational circuit to chip-level neutron-induced soft error rate: - Bulk vs. FD-SOI at 0.5 and 1.0V -,” in *2017 15th IEEE International New Circuits and Systems Conference (NEWCAS)*, Strasbourg, France, Jun. 2017, pp. 33–36. doi: 10.1109/NEWCAS.2017.8010098.

[6] T. Ndjountche, *Digital electronics 2: sequential and arithmetric logic circuits*. Hoboken, NJ: ISTE Ltd/John Wiley and Sons Inc, 2016.

[7] G. C. Messenger and M. S. Ash, *Single Event Phenomena*. Boston, MA: Springer US, 1997. doi: 10.1007/978-1-4615-6043-2.

[8] W. Liao *et al.*, “Measurement and Mechanism Investigation of Negative and Positive Muon-Induced Upsets in 65-nm Bulk SRAMs,” *IEEE Trans. Nucl. Sci.*, vol. 65, no. 8, pp. 1734–1741, Aug. 2018, doi: 10.1109/TNS.2018.2825469.

[9] “EXPACS Homepage.” Accessed: Oct. 13, 2023. [Online]. Available: https://phits.jaea.go.jp/expacs/jpn.html

[10] T. Sato, H. Yasuda, K. Niita, A. Endo, and L. Sihver, “Development of PARMA: PHITS-based Analytical Radiation Model in the Atmosphere,” *Radiation Research*, vol. 170, no. 2, pp. 244–259, Aug. 2008, doi: 10.1667/RR1094.1.

[11] T. Sato, “Analytical Model for Estimating Terrestrial Cosmic Ray Fluxes Nearly Anytime and Anywhere in the World: Extension of PARMA/EXPACS,” *PLOS ONE*, vol. 10, no. 12, p. e0144679, Dec. 2015, doi:

10.1371/journal.pone.0144679.

[12] “Cosmic rays: particles from outer space,” CERN. Accessed: Oct. 13, 2023. [Online]. Available: https://home.cern/science/physics/cosmic-rays-particles-outer-space

[13] B. D. Sierawski *et al.*, “Muon-Induced Single Event Upsets in Deep-Submicron Technology,” *IEEE Transactions on Nuclear Science*, vol. 57, no. 6, pp. 3273–3278, 2010, doi: 10.1109/TNS.2010.2080689.

[14] B. D. Sierawski *et al.*, “Effects of scaling on muon-induced soft errors,” in *2011 International Reliability Physics Symposium*, Apr. 2011, p. 3C.3.1-3C.3.6. doi: 10.1109/IRPS.2011.5784484.

[15] B. D. Sierawski *et al.*, “Bias dependence of muon-induced single event upsets in 28 nm static random access memories,” in *2014 IEEE International Reliability Physics Symposium*, Jun. 2014, p. 2B.2.1-2B.2.5. doi: 10.1109/IRPS.2014.6860585.

[16] J. M. Trippe *et al.*, “Predicting Muon-Induced SEU Rates for a 28-nm SRAM Using Protons and Heavy Ions to Calibrate the Sensitive Volume Model,” *IEEE Trans. Nucl. Sci.*, vol. 65, no. 2, pp. 712–718, Feb. 2018, doi: 10.1109/TNS.2017.2786585.

[17] S. Manabe, Y. Watanabe, W. Liao, M. Hashimoto, and S.-I. Abe, “Estimation of Muon-Induced SEU Rates for 65-nm Bulk and UTBB-SOI SRAMs,” *IEEE Trans. Nucl. Sci.*, vol. 66, no. 7, pp. 1398–1403, Jul. 2019, doi: 10.1109/TNS.2019.2916191.

[18] A. Coronetti *et al.*, “Proton Direct Ionization Upsets at Tens of MeV,” *IEEE Trans. Nucl. Sci.*, vol. 70, no. 4, pp. 314–321, Apr. 2023, doi: 10.1109/TNS.2022.3207877.

[19] G. Hubert, L. Artola, and D. Regis, “Impact of scaling on the soft error sensitivity of bulk, FDSOI and FinFET technologies due to atmospheric radiation,” *Integration*, vol. 50, pp. 39–47, Jun. 2015, doi: 10.1016/j.vlsi.2015.01.003.

[20] K. Nagamine, *Introductory Muon Science*. Cambridge: Cambridge University Press, 2003. doi: 10.1017/CBO9780511470776.

[21] S. Agostinelli *et al.*, “Geant4—a simulation toolkit,” *Nuclear Instruments and Methods in Physics Research Section A: Accelerators, Spectrometers, Detectors and Associated Equipment*, vol. 506, no. 3, pp. 250–303, Jul. 2003, doi: 10.1016/S0168-9002(03)01368-8.

[22] W. H. Barkas, W. Birnbaum, and F. M. Smith, “Mass-Ratio Method Applied to

the Measurement of L-Meson Masses and the Energy Balance in Pion Decay," *Phys. Rev.*, vol. 101, no. 2, pp. 778–795, Jan. 1956, doi: 10.1103/PhysRev.101.778.

[23] H. Bichsel, "Barkas effect and effective charge in the theory of stopping power," *Phys. Rev. A*, vol. 41, no. 7, pp. 3642–3647, Apr. 1990, doi: 10.1103/PhysRevA.41.3642.

[24] K. M. Erokhin and N. P. Kalashnikov, "Quasiclassical approach to the interpretation of the Barkas effect," *J. Synch. Investig.*, vol. 11, no. 3, pp. 562–569, May 2017, doi: 10.1134/S1027451017030065.

[25] D. F. Measday, "The nuclear physics of muon capture," *Physics Reports*, vol. 354, no. 4–5, pp. 243–409, Nov. 2001, doi: 10.1016/S0370-1573(01)00012-6.

[26] A. Edmonds *et al.*, "A Measurement of Proton, Deuteron, Triton and Alpha Particle Emission after Nuclear Muon Capture on Al, Si and Ti with the AlCap Experiment," *Phys. Rev. C*, vol. 105, no. 3, p. 035501, Mar. 2022, doi: 10.1103/PhysRevC.105.035501.

[27] Yu. G. Budyashov, V. G. Zinov, A. D. Konin, A. I. Mukhin, and A. M. Chatrchyan, "Charged Particles from the Capture of Negative Muons by the Nuclei 28Si, 32S, 40Ca, and 64Cu," *Soviet Journal of Experimental and Theoretical Physics*, vol. 33, p. 11, Jan. 1971.

[28] M. J. Berger *et al.*, "6. Energy-loss Straggling," *Reports of the International Commission on Radiation Units and Measurements*, vol. os-25, no. 2, pp. 61–68, May 1993, doi: 10.1093/jicru_os25.2.61.

[29] P. Rinard, "Neutron interactions with matter," *Passive nondestructive assay of nuclear materials*, no. 375–377, 1991.

[30] R. Gaillard, "Single Event Effects: Mechanisms and Classification," in *Soft Errors in Modern Electronic Systems*, M. Nicolaidis, Ed., in Frontiers in Electronic Testing. , Boston, MA: Springer US, 2011, pp. 27–54. doi: 10.1007/978-1-4419-6993-4_2.

[31] Y. Tosaka *et al.*, "Measurement and analysis of neutron-induced soft errors in sub-half-micron CMOS circuits," *IEEE Trans. Electron Devices*, vol. 45, no. 7, pp. 1453–1458, Jul. 1998, doi: 10.1109/16.701475.

[32] G. Cellere *et al.*, "Neutron-induced soft errors in advanced flash memories," in *2008 IEEE International Electron Devices Meeting*, Dec. 2008, pp. 1–4. doi: 10.1109/IEDM.2008.4796693.

[33] E. Ibe, H. Taniguchi, Y. Yahagi, K. Shimbo, and T. Toba, "Impact of Scaling on Neutron-Induced Soft Error in SRAMs From a 250 nm to a 22 nm Design

Rule," *IEEE Transactions on Electron Devices*, vol. 57, no. 7, pp. 1527–1538, Jul. 2010, doi: 10.1109/TED.2010.2047907.

[34] S. Abe *et al.*, "Neutron-induced soft error analysis in MOSFETs from a 65nm to a 25 nm design rule using multi-scale Monte Carlo simulation method," in *2012 IEEE International Reliability Physics Symposium (IRPS)*, Anaheim, CA, USA: IEEE, Apr. 2012, p. SE.3.1-SE.3.6. doi: 10.1109/IRPS.2012.6241928.

[35] K. Takami *et al.*, "Characterizing SEU Cross-sections of 12- and 28-nm SRAMs for 6.0, 8.0, and 14.8 MeV Neutrons," in *2023 IEEE International Reliability Physics Symposium (IRPS)*, Monterey, CA, USA: IEEE, Mar. 2023, pp. 1–6. doi: 10.1109/IRPS48203.2023.10118134.

[36] "Measurement and Reporting of Alpha Particle and Terrestrial Cosmic Ray Induced Soft Errors In Semiconductor Devices." 2021. Accessed: Oct. 23, 2023. [Online]. Available: https://www.jedec.org/standards-documents/docs/jesd-89a

[37] S. Abe, W. Liao, S. Manabe, T. Sato, M. Hashimoto, and Y. Watanabe, "Impact of Irradiation Side on Neutron-Induced Single-Event Upsets in 65-nm Bulk SRAMs," *IEEE Trans. Nucl. Sci.*, vol. 66, no. 7, pp. 1374–1380, Jul. 2019, doi: 10.1109/TNS.2019.2902176.

[38] J. F. Ziegler and W. A. Lanford, "Effect of Cosmic Rays on Computer Memories," *Science*, vol. 206, no. 4420, pp. 776–788, Nov. 1979, doi: 10.1126/science.206.4420.776.

[39] J. F. Dicello, C. W. McCabe, J. D. Doss, and M. Paciotti, "The Relative Efficiency of Soft-Error Induction in 4K Static RAMS by Muons and Pions," *IEEE Transactions on Nuclear Science*, vol. 30, no. 6, pp. 4613–4615, Dec. 1983, doi: 10.1109/TNS.1983.4333182.

[40] J. F. Dicello *et al.*, "Meson Interactions in NMOS and CMOS Static RAMs," *IEEE Transactions on Nuclear Science*, vol. 32, no. 6, pp. 4201–4205, Dec. 1985, doi: 10.1109/TNS.1985.4334094.

[41] J. F. Dicello, "Microelectronics and microdosimetry," *Nuclear Instruments and Methods in Physics Research Section B: Beam Interactions with Materials and Atoms*, vol. 24–25, pp. 1044–1049, Apr. 1987, doi: 10.1016/S0168-583X(87)80308-7.

[42] J. F. Dicello, M. Paciotti, and M. E. Schillaci, "An estimate of error rates in integrated circuits at aircraft altitudes and at sea level," *Nuclear Instruments and Methods in Physics Research Section B: Beam Interactions with Materials and Atoms*, vol. 40–41, pp. 1295–1299, Apr. 1989, doi: 10.1016/0168-

583X(89)90643-5.

[43] S. Serre, S. Semikh, J. L. Autran, D. Munteanu, G. Gasiot, and P. Roche, “Effects of Low Energy Muons on Electronics: Physical Insights and Geant4 Simulation,” presented at the RADECS 2012, Biarritz, France, Sep. 2012, p. 7.

[44] S. Manabe *et al.*, “Negative and Positive Muon-Induced Single Event Upsets in 65-nm UTBB SOI SRAMs,” *IEEE Trans. Nucl. Sci.*, vol. 65, no. 8, pp. 1742–1749, Aug. 2018, doi: 10.1109/TNS.2018.2839704.

[45] W. Liao *et al.*, “Impact of the Angle of Incidence on Negative Muon-Induced SEU Cross-sections of 65-nm Bulk and FDSOI SRAMs,” *IEEE Trans. Nucl. Sci.*, vol. 67, no. 7, pp. 1566–1572, Jul. 2020, doi: 10.1109/TNS.2020.2976125.

[46] J. M. Trippe *et al.*, “Predicting the vulnerability of memories to muon-induced SEUs with low-energy proton tests informed by Monte Carlo simulations,” in *2016 IEEE International Reliability Physics Symposium (IRPS)*, Pasadena, CA, USA: IEEE, Apr. 2016, p. SE-6-1-SE-6-6. doi: 10.1109/IRPS.2016.7574642.

[47] K. P. Rodbell, D. F. Heidel, H. H. K. Tang, M. S. Gordon, P. Oldiges, and C. E. Murray, “Low-Energy Proton-Induced Single-Event-Upsets in 65 nm Node, Silicon-on-Insulator, Latches and Memory Cells,” *IEEE Transactions on Nuclear Science*, vol. 54, no. 6, pp. 2474–2479, Dec. 2007, doi: 10.1109/TNS.2007.909845.

[48] D. F. Heidel *et al.*, “Low Energy Proton Single-Event-Upset Test Results on 65 nm SOI SRAM,” *IEEE Transactions on Nuclear Science*, vol. 55, no. 6, pp. 3394–3400, Dec. 2008, doi: 10.1109/TNS.2008.2005499.

[49] B. D. Sierawski *et al.*, “Impact of Low-Energy Proton Induced Upsets on Test Methods and Rate Predictions,” *IEEE Trans. Nucl. Sci.*, vol. 56, no. 6, pp. 3085–3092, Dec. 2009, doi: 10.1109/TNS.2009.2032545.

[50] J. A. Pellish *et al.*, “Criticality of Low-Energy Protons in Single-Event Effects Testing of Highly-Scaled Technologies,” *IEEE Transactions on Nuclear Science*, vol. 61, no. 6, pp. 2896–2903, Dec. 2014, doi: 10.1109/TNS.2014.2369171.

[51] N. A. Dodds *et al.*, “The Contribution of Low-Energy Protons to the Total On-Orbit SEU Rate,” *IEEE Transactions on Nuclear Science*, vol. 62, no. 6, pp. 2440–2451, Dec. 2015, doi: 10.1109/TNS.2015.2486763.

[52] Y. Luo, F. Zhang, X. Pan, H. Guo, and Y. Wang, “Impact of Total Ionizing Dose on Low Energy Proton Single Event Upsets in Nanometer SRAM,” *IEEE Transactions on Nuclear Science*, vol. 66, no. 7, pp. 1848–1853, Jul. 2019, doi: 10.1109/TNS.2019.2922501.

[53] C. Peng *et al.*, “Low-energy proton-induced single event effect in NAND flash memories,” *Nuclear Instruments and Methods in Physics Research Section A: Accelerators, Spectrometers, Detectors and Associated Equipment*, vol. 969, p. 164064, Jul. 2020, doi: 10.1016/j.nima.2020.164064.

[54] E. P. Wilcox *et al.*, “Observation of Low-Energy Proton Direct Ionization in a 72-Layer 3-D NAND Flash Memory,” *IEEE Transactions on Nuclear Science*, vol. 68, no. 5, pp. 835–841, May 2021, doi: 10.1109/TNS.2021.3063156.

[55] Y. Miyake *et al.*, “J-PARC muon source, MUSE,” *Nuclear Instruments and Methods in Physics Research Section A: Accelerators, Spectrometers, Detectors and Associated Equipment*, vol. 600, no. 1, pp. 22–24, Feb. 2009, doi: 10.1016/j.nima.2008.11.016.

[56] Y. Miyake *et al.*, “Current status of the J-PARC muon facility, MUSE,” *J. Phys.: Conf. Ser.*, vol. 551, no. 1, p. 012061, Dec. 2014, doi: 10.1088/1742-6596/551/1/012061.

[57] “Aerial shot from the west side of J-PARC【4-001】.” Accessed: Oct. 24, 2023. [Online]. Available: https://j-parc.jp/c/en

[58] “Overview of the Accelerators.” Accessed: Oct. 24, 2023. [Online]. Available: https://j-parc.jp/c/en

[59] S. Abe *et al.*, “A Terrestrial SER Estimation Methodology based on Simulation coupled with One-Time Neutron Irradiation Testing,” *IEEE Trans. Nucl. Sci.*, pp. 1–1, 2023, doi: 10.1109/TNS.2023.3280190.

[60] S. Manabe, “Study of Muon-induced Single Event Upsets in SRAMs and their Fundamental Physical Process,” Doctoral dissertation, Kyushu University, Fukuoka, Japan, 2021. [Online]. Available: https://catalog.lib.kyushu-u.ac.jp/opac_download_md/4475179/tj1177.pdf

[61] T. U. Ito, A. Toyoda, W. Higemoto, M. Tajima, Y. Matsuda, and K. Shimomura, “Online full two-dimensional imaging of pulsed muon beams at J-PARC MUSE using a gated image intensifier,” *Nuclear Instruments and Methods in Physics Research Section A: Accelerators, Spectrometers, Detectors and Associated Equipment*, vol. 754, pp. 1–9, Aug. 2014, doi: 10.1016/j.nima.2014.04.014.

[62] “EJ-200, EJ-204, EJ-208, EJ-212 - Plastic Scintillators - Eljen Technology.” Accessed: Sep. 22, 2023. [Online]. Available: https://eljentechnology.com/products/plastic-scintillators/ej-200-ej-204-ej-208-ej-212

[63] J. B. Birks, “Scintillations from Organic Crystals: Specific Fluorescence and

Relative Response to Different Radiations," *Proc. Phys. Soc. A*, vol. 64, no. 10, p. 874, Oct. 1951, doi: 20030219041302.

[64] G. D. Badhwar, C. L. Deney, B. R. Dennis, and M. F. Kaplon, "The non-linear response of the plastic scintillator NE102," *Nuclear Instruments and Methods*, vol. 57, pp. 116–120, Jan. 1967, doi: 10.1016/0029-554X(67)90507-1.

[65] I. Holl, E. Lorenz, and G. Mageras, "A measurement of the light yield of common inorganic scintillators," *IEEE Transactions on Nuclear Science*, vol. 35, no. 1, pp. 105–109, Feb. 1988, doi: 10.1109/23.12684.

[66] Y. Deng and Y. Watanabe, "A Method of Predicting Muon-Induced SEUs Using Proton Tests and Monte Carlo Simulation," *IEEE Transactions on Nuclear Science*, vol. 70, no. 8, pp. 1775–1782, Aug. 2023, doi: 10.1109/TNS.2023.3267767.

[67] M. J. Berger *et al.*, "ICRU Reports 49," *Reports of the International Commission on Radiation Units and Measurements*, vol. os-25, no. 2, pp. 280–283, May 1993, doi: 10.1093/jicru_os25.2.280.

[68] R. Bimbot *et al.*, "Stopping of Ions Heavier than Helium (ICRU73)," *Journal of the ICRU*, vol. 5, no. 1, pp. 1–253, Jun. 2005, doi: 10.1093/jicru/ndi001.

[69] W-M. Yao et al., "Review of Particle Physics," *J. Phys. G: Nucl. Part. Phys.*, vol. 33, no. 1, p. 1, Jul. 2006, doi: 10.1088/0954-3899/33/1/001.

[70] V. N. Ivanchenko, O. Kadri, M. Maire, and L. Urban, "Geant4 models for simulation of multiple scattering," *J. Phys.: Conf. Ser.*, vol. 219, no. 3, p. 032045, Apr. 2010, doi: 10.1088/1742-6596/219/3/032045.

[71] J. M. Fernández-Varea, R. Mayol, J. Baró, and F. Salvat, "On the theory and simulation of multiple elastic scattering of electrons," *Nuclear Instruments and Methods in Physics Research Section B: Beam Interactions with Materials and Atoms*, vol. 73, no. 4, pp. 447–473, Apr. 1993, doi: 10.1016/0168-583X(93)95827-R.

[72] H. W. Bertini and M. P. Guthrie, "News item results from medium-energy intranuclear-cascade calculation," *Nuclear Physics A*, vol. 169, no. 3, pp. 670–672, Jul. 1971, doi: 10.1016/0375-9474(71)90710-X.

[73] K. K. Gudima, S. G. Mashnik, and V. D. Toneev, "Cascade-exciton model of nuclear reactions," *Nuclear Physics A*, vol. 401, no. 2, pp. 329–361, Jun. 1983, doi: 10.1016/0375-9474(83)90532-8.

[74] W. Liao, M. Hashimoto, S. Manabe, S. Abe, and Y. Watanabe, "Similarity Analysis on Neutron- and Negative Muon-Induced MCUs in 65-nm Bulk SRAM," *IEEE Trans. Nucl. Sci.*, vol. 66, no. 7, pp. 1390–1397, Jul. 2019, doi:

10.1109/TNS.2019.2921365.

[75] ISMS, “Muon Facilities Introduction on website of ISMS,” Isms. Accessed: Nov. 03, 2023. [Online]. Available: https://www.musr.org/muon-facilities

[76] B. Andersson, G. Gustafson, and B. Nilsson-Almqvist, “A model for low-pT hadronic reactions with generalizations to hadron-nucleus and nucleus-nucleus collisions,” *Nuclear Physics B*, vol. 281, no. 1, pp. 289–309, Jan. 1987, doi: 10.1016/0550-3213(87)90257-4.

[77] A. Coronetti *et al.*, “Assessment of Proton Direct Ionization for the Radiation Hardness Assurance of Deep Submicron SRAMs Used in Space Applications,” *IEEE Trans. Nucl. Sci.*, vol. 68, no. 5, pp. 937–948, May 2021, doi: 10.1109/TNS.2021.3061209.

[78] Y. Gomi *et al.*, “Muon-Induced SEU Cross-sections of 12-nm FinFET and 28-nm Planar SRAMs,” presented at the RADECS 2023, Toulouse, France, Sep. 2023.

[79] T. Uemura, T. Kato, H. Matsuyama, and M. Hashimoto, “Soft-Error in SRAM at Ultra-Low Voltage and Impact of Secondary Proton in Terrestrial Environment,” *IEEE Transactions on Nuclear Science*, vol. 60, no. 6, pp. 4232–4237, Dec. 2013, doi: 10.1109/TNS.2013.2291274.

[80] W. Tianqi *et al.*, “Single-Event Upset Prediction in SRAMs Account for On-Transistor Sensitive Volume,” *IEEE Transactions on Nuclear Science*, vol. 62, no. 6, pp. 3207–3215, Dec. 2015, doi: 10.1109/TNS.2015.2480880.

Acknowledgments

This work was carried out at the Department of Interdisciplinary Engineering Sciences, Interdisciplinary Graduate School of Engineering Sciences, Kyushu University, under the supervision of Professor Yukinobu Watanabe. This work began in April 2021, and as of today, I have been helped by many mentors and friends. I wish to express my heartfelt gratitude to them.

First, I would like to express my deepest gratitude to Professor Yukinobu Watanabe for supervising me enthusiastically. During my first year of enrollment, I had to conduct research at home in China because of the Covid-19 epidemic. It was Prof. Watanabe's regular online meetings and guidance that kept me on track with my research, and we got through that difficult time together. During the three years of study, his guidance and fruitful advice always inspired me with new ideas and kept my work from careless mistakes. Moreover, I have learned a lot from him, such as a sincere attitude toward research, the patience to explore the unknown step by step, the perspective of being bold in assumptions and being careful in evidence, and so on. I will keep learning and studying hard by making use of the knowledge and experiences received from him.

My great thanks are also expressed to Professors Hironao Sakaki and Masanori Hashimoto for their careful reading of this manuscript and valuable comments. In particular, I would like to express my great gratitude to Professors Masanori Hashimoto and Wang Liao for providing the raw data and necessary information for the muon experiments and giving a lot of guidance and help.

Moreover, I would like to express my great thanks to Doctor Seiya Manabe. Although we have never met, my research is based on his former research on muon experiments and PHITS simulations. He graduated from our laboratory years ago and gave me essential guidance and help via e-mail.

I would like to thank Doctor Shin-ichiro Abe very much for helpful advice on the transport simulation and nuclear reaction of muons during my study. As the supervisor in my summer internship at JAEA, he gave me a lot of guidance and help, which helped me gain a deeper understanding of negative muon capture.

My appreciation also goes to Assistant Professor Shoichiro Kawase for valuable comments on the simulation setting and analysis of the beam profile monitor. In addition, he often shared his knowledge of Japanese culture and the Japanese language with me in our regular conversations, for which I feel grateful.

It has been an enormous pleasure for me to work together with Naoya Okamoto, Satoko Kamei, Naoto Nakagami, Ayumu Okuda, Kawata Teppei, and Kentaro Kitafuji in our laboratory, as well as the graduates Hiroto Shiba, Shotaro Fukunaga and

Hirotaka Tanaka.

My thanks are expressed to Rumiko Koga for her help with office work. With her kind support, I was able to solve a lot of difficulties with office documents.

This work was supported by Grant-in-Aid for Scientific Research (S) from the Japan Society for the Promotion of Science under Grant 19H05664. The muon irradiation tests described in Chapter 2 were performed at the MLF in J-PARC under user programs Nos. 2016B0046 and 2017A0139.

Finally, I would like to express my gratitude to my family for permitting me to continue my research at the graduate school and for supporting me during these three years. I would also like to thank my fiancée, Ze Zhang, for supporting and encouraging me throughout my three years of PhD study. Without their support, I could not complete this work.